University of Nottingham
UK | CHINA | MALAYSIA

Discrete Breathers in One- and Two-Dimensional Mechanical Lattices

Reem Almarashi

Thesis submitted to the University of Nottingham
for the degree of Doctor of Philosophy

May 2025

Acknowledgements

Alhamdulillah, all praise is due to Allah for granting me strength perseverance, and guidance throughout this journey.

I am deeply grateful to my family for their unwavering support and wise advice. My heartfelt thanks go to my beloved parents, Hamidah Hamid and Mosleh Hela, for their endless love and encouragement. To my sisters, Eman and Linah, whose exceptional support and kindness have been a cornerstone of my journey, I owe a special debt of gratitude. I am also grateful to Raha and Alaa for their encouragement and love. To my brothers, especially Adnan, thank you for standing by me and inspiring me every step of the way.

I extend my sincere gratitude to Saudi Electronic University for providing the funding and support that made this work possible, and to the Royal Embassy of Saudi Arabia Cultural Bureau for their guidance.

I am thankful to my supervisors Jonathan Wattis, Rachel Nicks and to the School of Mathematics at the University of Nottingham, for their mentorship and invaluable contributions to my academic journey.

To my friends and all who have supported me in any way throughout this endeavour, thank you from the bottom of my heart.

List of Abbreviations

1D	One Dimensional
2D	Two Dimensional
c.c	Complex Conjugate
DBs	Discrete Breathers
ETL	Electrical Transmission Lattice
FPUT	Fermi–Pasta–Ulam–Tsingou (Lattice)
KG	Klein Gordon (Lattice)
MiM	Mass-in-Mass
mKdV	Modified Korteweg–de Vries (Equation)
NLEs	Nonlinear Localized Excitations
NLS	Nonlinear Schrödinger
NNIs	Nearest Neighborhood Interactions
ODEs	Ordinary Differential Equations
PDEs	Partial Differential Equations
SG	Sine-Gordon Equation
SLAM	Self-Localized Mode
SNI	Second Neighborhood Interaction
STWs	Solitary Travelling Waves

Contents

List of Tables

List of Figures

Abstract

In this thesis, we investigate discrete breathers in nonlinear mechanical lattices through numerical and asymptotic methods. First, in a one-dimensional mass-in-mass Fermi–Pasta–Ulam–Tsingou (FPUT) chain with internal oscillators, we identify stable stationary breathers and long-lived weakly unstable stationary and moving breathers and breather–kinks. Second, in two-dimensional hexagonal lattices, we use multiple scales analysis, we derive the equations governing wave propagation and reduce them to Nonlinear Schrödinger (NLS) equations. We identify the ellipticity condition and a focusing condition for the exist of fully localised NLS solutions in triangular geometries, and derive (2+1)-dimensional and coupled (2+1)-dimensional NLS subsystems in honeycomb structures. The latter arise from critical points of the dispersion relation and yield existence criteria for small-amplitude breathers. These results are relevant for predictive models for energy localisation in mechanical metamaterials as they link lattice symmetry, nonlinearity and breather stability.

Chapter 1

Introduction and Literature Review

In this introductory chapter, we review the various types of solitons: breather, pulses and travelling kink waves are introduced, and some historical developments are illustrated. It is shown that discrete nonlinear systems play an important role in the analysis of complex dynamical behaviour, as in electronic and mechanical dynamics. These are pivotal in applications related to advanced materials, such as graphene and metamaterials, where understanding interactions at the microscopic level can lead to the manipulation of wave propagation through engineered nonlinearity. These findings may contribute to the development of next generation technologies.
This chapter therefore presents a motivation for the thesis and for the thesis structure.

1.1 Historical developments

The study of lattice dynamics is fundamental to understanding the intrinsic properties of crystalline solids. Lattices, understood as the periodic arrangement of atoms or molecules in a crystal, exhibit harmonic and anharmonic behaviours that significantly influence a material's physical characteristics. In

the harmonic regime, atoms oscillate about their equilibrium positions due to forces proportional to their relative displacements, allowing for analytical simplifications in predicting crystal behaviour.

However, real world crystals deviate from purely harmonic behaviour due to anharmonicity. These nonlinear effects arise when atomic displacements are sufficiently, resulting in interactions beyond the harmonic approximation. Such phenomena manifest in optics, electronics and acoustics. This transition from harmonic to anharmonic dynamics reflects the movement from idealised systems to realistic models that account for fluctuating mechanical interactions.

Translational symmetry allows a lattice to extend across thousands of atoms, producing a regular repeating pattern. This periodicity is essential in defining the a crystal's electronic band structure and phonon dispersion relations. However, defects or vibrational excitations may break the symmetry, introducing localised states or scattering centres that significantly alter the lattice's overall behaviour.

Solitons, including breathers and kinks, emerge as distinct solutions to nonlinear partial differential equations (PDEs) in nonlinear wave dynamics. Solitons are localised waves that retain their shape and velocity post interaction, thus distinguishing them from typical dispersive waves. Travelling waves, a broader category, include pulses and kinks each characterised by specific propagation and localisation features. A *pulse* is a localised wave packet with a peak that propagates while maintaining its form. By contrast, a *kink* features a transition in amplitude across the medium, connecting distinct asymptotic states.

1.1.1 Breathers and Localised Oscillations

Breathers, or *Discrete Breathers (DBs)*, represent localised oscillatory modes that concentrate energy in discrete systems [3]. These modes have also been referred to by various other terms: *Intrinsic Localised Modes (ILMs)* emphasise their emergence in defect-free lattices; *Self-Localised Modes (SLAMs)* highlight

the self-trapping mechanism; and *Nonlinear Localised Excitations (NLEs)* describe their general nonlinear nature. The term "Discrete Breather" was coined by Flach and Willis [3], whose framework is adopted throughout this thesis. DBs have been studied in quasi one dimensional lattices, where high energy, fully localised solutions exist even in higher-dimensional configurations [4]. In some systems, such as those governed by the sine-gordon (SG) equation

$$\frac{\partial^2 u}{\partial t^2} - \frac{\partial^2 u}{\partial x^2} + \sin(u) = 0, \tag{1.1.1}$$

breathers appear as bound states of kink-anti-kink pairs. However, in many discrete systems, DBs are better viewed as individual entities, exhibiting robust propagation similar to travelling kinks.

1.1.2 Breather Existence

Breathers exist in nonlinear discrete systems due to two fundamental features: first, *discreteness* introduces an upper limit to the dispersion relation, allowing the breather frequency and its harmonics to lie outside the phonon bands; and second, *nonlinearity* ensures that the breather frequency and its harmonics can avoid resonances with linear modes, enabling the solution to remain long lived.

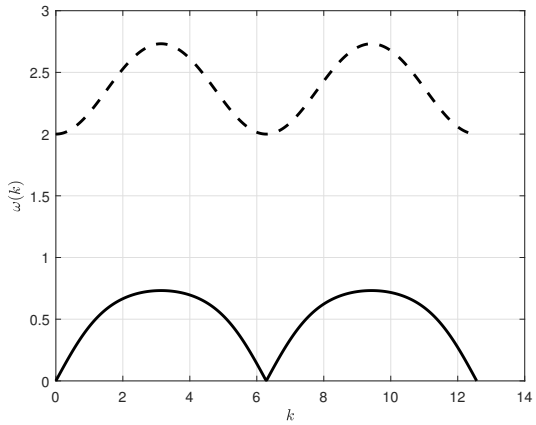

Figure 1.1: Illustration of the dispersion relation (2.2.6) [1] for $0 < k < 4\pi$, and $\rho = 3, \mu = 3$. The solid line represents the acoustic branch, while the dashed line corresponds to the optical branch.

For example (Figure 1.1), a frequency gap lies between the two branches, and the frequency of a breather may occur either above the optical branch or below the acoustic branch. Breathers can also exist in continuous systems, provided that nonlinear and dispersive effects are in balance.

1.1.3 Wobbling Kinks

A *wobbling kink* is a kink soliton that exhibits internal periodic oscillations while maintaining its shape. The "wobbling" describes internal oscillations of the kink's shape that occur during its propagation. Instead of moving smoothly, it "wobbles" around its equilibrium [5]. The potential function in the ϕ^4 model has two symmetric minima, and the equation of motion is derived from the Hamiltonian

$$\mathcal{H} = \frac{1}{2}\left(\left(\frac{\partial\phi}{\partial t}\right)^2 + \left(\frac{\partial\phi}{\partial x}\right)^2\right) + V(\phi), \tag{1.1.2}$$

where the potential is given by

$$V(\phi) = \frac{1}{4}\phi^4 - \frac{1}{2}\phi^2. \tag{1.1.3}$$

The corresponding equation of motion is

$$\frac{\partial^2\phi}{\partial t^2} - \frac{\partial^2\phi}{\partial x^2} - \phi + \phi^3 = 0. \tag{1.1.4}$$

The stationary kink solution connecting $\phi = -1$ as $x \to -\infty$, and $\phi = 1$ as $x \to \infty$, is

$$\phi(x,t) = \tanh\left(\frac{x}{\sqrt{2}}\right). \tag{1.1.5}$$

To study wobbling behaviour, we introduce a small perturbation

$$\phi(x,t) = \phi_{\text{kink}}(x) + \epsilon\eta(x,t), \tag{1.1.6}$$

with $\epsilon \ll 1$. Linearising (1.1.4) leads to

$$\frac{\partial^2 \eta}{\partial t^2} - \frac{\partial^2 \eta}{\partial x^2} + \left(3\phi^2(x,t) - 1\right)\eta = 0. \tag{1.1.7}$$

Here, $(3\phi^2(x,t) - 1)$ represents the effective potential generated by the kink, with the ϕ^4 model yielding

$$U(x) = 2 - 3\,\mathrm{sech}^2\left(\frac{x}{\sqrt{2}}\right), \tag{1.1.8}$$

resulting in the perturbation equation

$$\frac{\partial^2 \eta}{\partial t^2} - \frac{\partial^2 \eta}{\partial x^2} + U(x)\,\eta = 0. \tag{1.1.9}$$

Assuming a separable solution $\eta(x,t) = e^{i\omega t}\Psi(x)$, we reduce the (1.1.9) to a time-independent Schrödinger-type equation

$$-\frac{d^2\Psi}{dx^2} + U(x)\Psi = \omega^2\Psi, \tag{1.1.10}$$

which allows us to identify the internal (wobbling) modes of the kink.

1.1.4 Lattice models: mass-spring systems and nonlinear potentials

We now illustrate the theoretical frameworks and computational models used to describe discrete mass-spring systems in one dimension (1D), focusing on the Fermi–Pasta–Ulam–Tsingou (FPUT) and Klein–Gordon (KG) lattices. A mass-spring chain represents a straightforward 1D atomic lattice or crystal model. This system is typically formulated as a dynamical system with the Hamiltonian

$$\mathcal{H}(p,q) = \sum_n \frac{1}{2m}p_n^2 + \sum_n W(q_n) + \sum_n V(q_{n+1} - q_n), \tag{1.1.11}$$

where m is the mass of each particle, p_n is the momentum conjugate to displacement q_n, and V and W are real valued potential functions. As illustrated in Figure 1.2, the quantity q_n measures the displacement of the n-th particle from its equilibrium position. Let $\phi = q_{n+1} - q_n$ denote the strain between neighbouring particles.

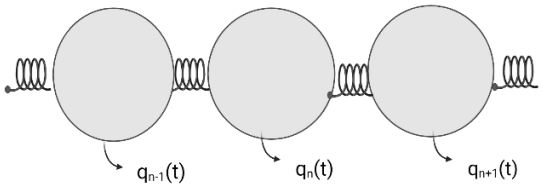

Figure 1.2: Schematic illustration of a 1D mass-spring chain model.

Different choices of V and W yield various well-known lattice models, including:

- **FPUT lattice**

$$W(q) = 0, \quad V(\phi) = \frac{1}{2}\phi^2 + \alpha\frac{\phi^3}{3} + \beta\frac{\phi^4}{4}, \tag{1.1.12}$$

  where α and β represent the strengths of cubic and quartic nonlinearity, respectively. The cases $\beta = 0$ and $\alpha = 0$ correspond to the α-FPUT and β-FPUT models respectively.

- **Klein–Gordon (KG) lattice**

$$W(q) = \sum_{r=2}^{\infty} a_r q^r, \quad V(\phi) = c\frac{\phi^2}{2}, \tag{1.1.13}$$

  where the coefficients a_r arise from the Taylor expansion of the on-site potential $W(q)$, and c is a coupling constant.

For asymptotic methods applied to small amplitude solutions, only the leading-order terms in the Taylor expansion of the potential functions are typically

considered. Combining the Hamiltonian (1.1.11) with the FPUT potential (1.1.12) yields the equation of motion

$$\frac{d^2q_n}{dt^2} = (q_{n+1}-2q_n+q_{n-1})+a(q_{n+1}^2-2q_n^2+q_{n-1}^2)+b(q_{n+1}^3-2q_n^3+q_{n-1}^3), \quad (1.1.14)$$

where a and b relate to the nonlinear terms in the interaction potential. This discrete second-order equation reflects the interplay between linear coupling and nonlinear interactions, governing the evolution of nodal displacements $q_n(t)$ in the mass-spring chain.

1.1.5 Alternative potentials: Toda and Morse models

Beyond polynomial potentials, other forms are prominent in the literature on nonlinear lattice dynamics.

Toda potential

$$V(\phi) = \frac{\alpha}{\beta}\left(e^{-\beta\phi} + \beta\phi - 1\right), \quad V'(\phi) = \alpha(1 - e^{-\beta\phi}), \quad (1.1.15)$$

where α controls the amplitude, and β determines how rapidly the potential decays with increasing ϕ. The Toda lattice is notable for admitting exact solutions [6]. For small displacements ϕ, a Taylor expansion of the Toda potential yields terms resembling the FPUT model with polynomial nonlinearity.

Morse potential

$$V(\phi) = \alpha\left(1 - e^{-\beta(\phi-\phi_0)}\right)^2, \quad (1.1.16)$$

commonly used to model molecular vibrations, particularly where bond-breaking occurs [7]. Here, ϕ_0 is the equilibrium position, β controls the width of the potential well, and α represents the depth of the potential.

In this thesis, we focus primarily on onsite potentials $W(q)$ and polynomial

interaction potentials $V(\phi)$, as given in equations (1.1.12) and (1.1.13). In the next section, we will discuss the NLS equations.

1.2 Nonlinear Schrödinger equation

The Nonlinear Schrödinger (NLS) equation plays a vital role in many areas of mathematical physics, as it describes the slow modulation of envelope solitons in dispersive nonlinear media. The general form of the NLS equation in d-dimensions with power-law nonlinearity 2σ is given by

$$i\psi_t + D\nabla^2\psi + B|\psi|^{2\sigma}\psi = 0, \quad \psi(x,0) = \phi(x), \tag{1.2.1}$$

where $\psi(x,t)$ is a complex-valued wave function, with $t \in [0,\infty)$ and $x \in \mathbb{R}^d$. Here, ∇^2 denotes the Laplacian in d dimensions, D is the dispersion coefficient, and B is the nonlinear coefficient.

The classification of the NLS equation (2.2.9) depends on the sign of the product BD:

- If $BD < 0$, the equation is defocusing, supporting *dark solitons*.
- If $BD > 0$, the equation is focusing, supporting *bright solitons*.

This classification is not original to the present work but is established in seminal works (see, e.g., [8–10]) and has been extensively studied (see, e.g., [11, 12]). Coupled NLS systems are discussed in [13, 14].

Rasmussen [10] used the method of moments (also called *virial theory*) to derive sufficient conditions for *blow-up*, where a localised wave can collapse and its amplitude becomes unbounded in finite time. Two conserved quantities in the NLS equation (2.2.9) are

$$\mathcal{H} = \int \left(D|\nabla\psi|^2 - \frac{B}{\sigma+1}|\psi|^{2\sigma+2} \right) d^d x, \qquad \mathcal{N} = \int |\psi|^2 \, d^d x, \tag{1.2.2}$$

where $\mathcal{H}$ is the Hamiltonian (conserved energy) and $\mathcal{N}$ is the norm (conserved mass). Blow-up can occur if: $\mathcal{H} < 0$, and $\mathcal{N}_0 > \mathcal{N}_c$, where $\mathcal{N}_c$ is the critical norm which depends on the spatial dimension d.

For initial data with $\mathcal{N}_0 < \mathcal{N}_c$ and $\mathcal{H} > 0$, the solution tends to disperse or decay. The parameter $\sigma_c = \frac{2}{d}$ defines three key regimes:

Subcritical: $\sigma < \sigma_c$; Critical: $\sigma = \sigma_c$; and Supercritical: $\sigma > \sigma_c$.

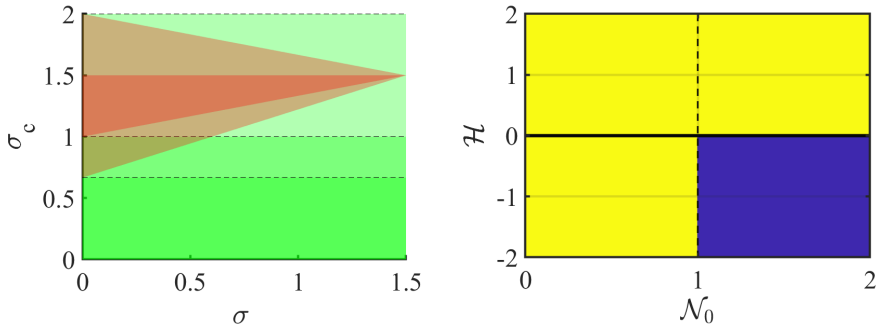

Figure 1.3: Left: the relationship between the nonlinearity power σ and critical threshold σ_c in dimensions $d = 1, 2, 3$. Green indicates a subcritical regime; red a supercritical regime. Right: regions of blow-up and dispersion depending on the initial norm $\mathcal{N}_0$ and energy $\mathcal{H}$.

A notable solution of the focusing NLS equation is the Townes soliton [15], which arises when $\sigma = 1$, $d = 2$. This one parameter family of solutions can be analysed via asymptotic and numerical methods [8, 13, 14, 16–18].

1.2.1 Coupled nonlinear Schrödinger equations

The coupled NLS equations describe the interaction between two or more nonlinear wave components. They are widely used in nonlinear optics, Bose Einstein condensates (BECs) and plasma physics [13]. A general 1D system for

two interacting wave fields $\psi_1(x,t)$ and $\psi_2(x,t)$ is

$$i\frac{\partial\psi_1}{\partial t}+\frac{\partial^2\psi_1}{\partial x^2}+\gamma_1|\psi_1|^2\psi_1+\beta|\psi_2|^2\psi_1=0, \tag{1.2.3}$$
$$i\frac{\partial\psi_2}{\partial t}+\frac{\partial^2\psi_2}{\partial x^2}+\gamma_2|\psi_2|^2\psi_2+\beta|\psi_1|^2\psi_2=0, \tag{1.2.4}$$

where γ_1,γ_2 are the nonlinear interaction coefficients for each wave respectively, and β is the nonlinear interaction coefficients between the two waves. If γ_1,γ_2,β are equal, then the model (1.2.3)-(1.2.4) simplifies to the Manakov model as

$$i\frac{\partial\psi_1}{\partial t}+\frac{\partial^2\psi_1}{\partial x^2}+\gamma\left(|\psi_1|^2+|\psi_2|^2\right)\psi_1=0, \tag{1.2.5}$$
$$i\frac{\partial\psi_2}{\partial t}+\frac{\partial^2\psi_2}{\partial x^2}+\gamma\left(|\psi_1|^2+|\psi_2|^2\right)\psi_2=0. \tag{1.2.6}$$

Here, γ is a common nonlinear interaction strength between and within the fields. This unified form simplifies the analysis of vector soliton solutions. The solutions of the Manakov model include Dark–Bright (D–B) and Dark–Dark (D–D) solitons [13]. Bright solitons are localised peaks in the wave amplitude and are usually observed in focusing NLS equations. Dark solitons, on the other hand, occur in defocusing NLS equations. These can be derived using analytical techniques, including the *multiple-scales method* (see Section 1.3.2). In [13], the authors consider a generalisation of the Manakov model given by

$$i\frac{\partial\psi_1}{\partial t}+\frac{\partial^2\psi_1}{\partial x^2}+\gamma\left(|\psi_1|^2+|\psi_2|^2+\mu+V(x)\right)\psi_1=0, \tag{1.2.7}$$
$$i\frac{\partial\psi_2}{\partial t}+\frac{\partial^2\psi_2}{\partial x^2}+\gamma\left(|\psi_2|^2+|\psi_1|^2+\mu+V(x)\right)\psi_2=0, \tag{1.2.8}$$

where $\gamma=1$, μ , and $V(x)$ are potentials relevant to BEC systems. The dark–bright (D–B) soliton solution of the generalised Manakov model is expressed in terms of two real-valued amplitude functions $|\psi_1|$ and $|\psi_2|$. These describe the density profiles of the dark and bright components respectively

$$|\psi_1| = \mu\cos^2(\delta) - \left(\mu\cos^2(\delta)\cos^2\phi - \eta^2\sin^2(\delta)\right)\operatorname{sech}^2(\xi) - \sqrt{\mu}\eta\sin(2\delta)\left[\sin\phi\sin(kx+\theta(t)) + \cos\phi\cos(kx+\theta(t))\tanh(\xi)\right]\operatorname{sech}(\xi), \tag{1.2.9}$$

$$|\psi_2| = \mu\sin^2(\delta) - \left(\mu\sin^2(\delta)\cos^2\phi - \eta^2\cos^2(\delta)\right)\operatorname{sech}^2(\xi) + \sqrt{\mu}\eta\sin(2\delta)\left[\sin\phi\sin(kx+\theta(t)) + \cos\phi\cos(kx+\theta(t))\tanh(\xi)\right]\operatorname{sech}(\xi), \tag{1.2.10}$$

where the parameters are defined as follows: μ is the background amplitude of the dark component; δ the mixing angle controlling the amplitude ratio of the dark and bright components; η is the amplitude of the bright soliton (setting $\eta = 0$ yields a dark–dark soliton); ϕ is the phase angle determining the soliton type; the $\xi = D(x - x_0(t))$ is the moving spatial coordinate with inverse width D and soliton centre $x_0(t)$; the $k = D\tan\phi$ is an associated wavenumber; and the $\theta(t) = \frac{1}{2}(D^2 - k^2)t + \theta_0$ is the phase shift, with θ_0 a constant phase offset. The parameters must satisfy the balance condition

$$D^2 = \mu\cos^2\phi - \eta^2,$$

to ensure a stable coupling between the dark and bright components.

1.3 Asymptotic analysis

Asymptotic analysis provides powerful tools for understanding complex systems by examining their behaviour in limiting regimes often described by partial differential equations (PDEs). This approach is particularly useful when seeking explicit approximate solutions, such as breathers that are otherwise difficult to obtain. A substantial body of research has focused on deriving such approximate solutions.

In this context, we focus on two primary techniques, which are often used in

conjunction with each other: the Continuum Approximation and the method of Multiple Scales. The Continuum Approximation allows discrete systems to be represented as continuous media on a macroscopic scale. By contrast, the multiple scale method is designed to handle problems where different temporal and spatial scales influence the system dynamics. We now briefly outline how these techniques are employed to construct analytical solutions.

1.3.1 Continuum approximation

In the continuum approximation, a discrete physical system such as a lattice composed of interacting particles is modelled as a continuous medium, to investigate phenomena on length scales much greater than the lattice spacing [19]. This allows the discrete variables n to be replaced by continuous $x = \varepsilon n$ and $\varepsilon \ll 1$. For example, instead of tracking the displacement of each atom in a crystal lattice by $\phi_n(t)$, one approximates the configuration using a field that varies continuously in both space and time $\phi(x,t)$. The governing PDEs are then derived from the original discrete model through suitable approximations. Consider a 1D FPUT lattice, where the relative displacements between neighbouring particles are given by $\phi_n = q_{n+1} - q_n$. The discrete equation of motion is given by

$$\frac{d^2\phi_n(t)}{dt^2} = V'(\phi_{n+1}) - 2V'(\phi_n) + V'(\phi_{n-1}), \tag{1.3.1}$$

where the derivative of the interaction potential $V(\phi)$ (1.1.12) takes the form

$$V'(\phi) = \phi + \alpha\phi^2 + \beta\phi^3. \tag{1.3.2}$$

$$\frac{d^2\phi_n(t)}{dt^2} = \phi_{n+1} - 2\phi_n + \phi_{n-1} + \alpha\left(\phi_{n+1}^2 - 2\phi_n^2 + \phi_{n-1}^2\right) \tag{1.3.3}$$

To derive the continuum limit for the case $\beta = 0$, we introduce a continuous spatial variable $x = \varepsilon n$, assuming a small lattice spacing ε. The key assumption is that $\phi_n(t)$ varies slowly in space, allowing us to approximate $\phi_n(t) \approx \phi(x,t)$,

where $\phi(x,t)$ is a smooth function. Furthermore, we assume a small amplitude expansion such that $\phi = \mathcal{O}(\epsilon^2)$, implying that $\phi^2 = \mathcal{O}(\epsilon^4)$ and $\phi^3 = \mathcal{O}(\epsilon^6)$, ensuring weak nonlinearity.

Expanding $\phi_{n\pm1}(t)$=$\phi(x \pm \varepsilon, t)$ in a Taylor series yields

$$\phi(x \pm \varepsilon, t) = \phi(x,t) \pm \varepsilon \frac{\partial \phi}{\partial x} + \frac{\varepsilon^2}{2}\frac{\partial^2 \phi}{\partial x^2} \pm \frac{\varepsilon^3}{6}\frac{\partial^3 \phi}{\partial x^3} + \cdots . \tag{1.3.4}$$

Substituting into the discrete equation (1.3.1) and keeping terms up to fourth order in ε, we obtain

$$\frac{\partial^2 \phi}{\partial t^2} = \varepsilon^2 \frac{\partial^2}{\partial x^2}\left(\phi + \alpha\phi^2\right) + \frac{\varepsilon^4}{12}\frac{\partial^4}{\partial x^4}\left(\phi + \alpha\phi^2\right) + \cdots . \tag{1.3.5}$$

$$\frac{\partial^2 \phi}{\partial t^2} = \varepsilon^2 \frac{\partial^2 \phi}{\partial x^2} + \frac{\varepsilon^4}{12}\frac{\partial^4 \phi}{\partial x^4} + \alpha\varepsilon^2 \frac{\partial^2 \phi^2}{\partial x^2} + \mathcal{O}(\varepsilon^6). \tag{1.3.6}$$

Now, consider a travelling wave solution of the form $\phi_n(t) = \phi(\varepsilon(n - ct)) = \phi(z)$, where $z = \varepsilon(n - ct)$ and c denotes the wave speed. Substituting into the original discrete equation (1.3.1) gives

$$\varepsilon^2 c^2 \frac{\partial^2 \phi}{\partial z^2} = \varepsilon^2 \frac{\partial^2 \phi}{\partial z^2} + \frac{\varepsilon^4}{12}\frac{\partial^4 \phi}{\partial z^4} + \alpha\varepsilon^2 \frac{\partial^2 \phi^2}{\partial z^2} + \mathcal{O}(\varepsilon^6). \tag{1.3.7}$$

assuming $\phi = \varepsilon^2\psi \quad , \psi = \mathcal{O}(1)$, we get

$$\varepsilon^4(c^2 - 1)\frac{\partial^2 \psi}{\partial z^2} = \frac{\varepsilon^6}{12}\frac{\partial^4 \psi}{\partial z^4} + \alpha\varepsilon^6 \frac{\partial^2 \psi^2}{\partial z^2} + \mathcal{O}(\varepsilon^6). \tag{1.3.8}$$

To balance term, we consider speed near unity, specifically $(c^2 - 1) \approx \mathcal{O}(\varepsilon^2)$, we simplify (1.3.8) to

$$\frac{(c^2 - 1)}{\varepsilon^2}\frac{\partial^2 \psi}{\partial z^2} = \frac{1}{12}\frac{\partial^4 \psi}{\partial z^4} + \alpha\frac{\partial^2 \psi^2}{\partial z^2} + \cdots . \tag{1.3.9}$$

We consider a small amplitude solitary wave solution of the form

$$\phi(z) = \frac{3}{2\alpha}\frac{(c^2-1)}{\varepsilon^2}\,\mathrm{sech}\left(\frac{3(c^2-1)}{\varepsilon^2}z\right). \tag{1.3.10}$$

In this limit, the solitary wave retains its structure and smoothness, consistent with the expectations of the continuum approximation.

1.3.2 Multiple scale approximation

An effective method for determining an approximation for breather solutions is the multiple scales method that is frequently used in perturbation theory, nonlinear dynamics, and wave propagation, as well as when a system features behaviour on multiple scales that interact with each other, such as a slow modulation of a fast oscillation [19, 20] . In this method, we introduce multiple independent scales, such as a very long time scale, i.e. $T = \varepsilon^2 t$ for the oscillation; a long time scale, i.e. $\tau = \varepsilon t$; and a slow space scale $X = \varepsilon m$ in one dimension for the modulation of breather amplitude. Then, we apply the asymptotic expansion of the solution in terms of a small parameter $\varepsilon \ll 1$, where each term in the expansion depends on these multiple scales. Therefore, expanding the solution and considering interactions between different scales can cover the system's behaviour. The phase θ of linear waves characterizes the oscillatory behaviour of the wave and depends on the wave number and spatial dimensions. In a 1D chain, the phase can be displayed as $\theta = km + \omega(k)t$, where k is the wave number, m represents the position along the chain and $\omega(k)$ is the frequency of the wave. By considering the displacements u_m as the function of the independent variables m, t, X, τ and T, the ansatz solution for

1D lattices has the form

$$\begin{aligned} u_m(t) = \varepsilon e^{i\theta} F(x,\tau,T) + \varepsilon^2 (e^{2i\theta} G_2(x,\tau,T) + e^{i\theta} G_1(x,\tau,T) + G_0(x,\tau,T)) \\ + \varepsilon^3 (e^{3i\theta} H_3(x,\tau,T) + e^{2i\theta} H_2(x,\tau,T) + e^{i\theta} H_1(x,\tau,T) + H_0(x,\tau,T)) \\ + ... + c.c, \end{aligned} \tag{1.3.11}$$

where the $c.c$ is the complex conjugate.

In [21], Butt & Wattis considered a 1D FPUT chain whose particles interact with their nearest neighbours. They sought small amplitude breather-kink solutions by performing a standard multiple-scale asymptotic expansion for the difference of displacements same, as (1.3.11) in the form

$$\phi_n(t) = \varepsilon e^{i\omega t + ikm} F(Z,T) + \ldots, \tag{1.3.12}$$

where $\varepsilon \ll 1$ is a small parameter, $T = \varepsilon^2 t$ is a very long timescale, and Z is the slow travelling wave coordinate (see equation 1.3.14). This ansatz leads to an NLS equation for F with cubic nonlinearity. Substituting the ansatz solution (1.3.11) in the equation of motion (1.1.14), equating the similar orders of ε, we get

- at order $\mathcal{O}(\varepsilon e^{i\theta})$, the linear dispersion relation

$$\omega(k) = 2\sin\left(\frac{k}{2}\right), \tag{1.3.13}$$

- at $\mathcal{O}(\varepsilon^2 e^{i\theta})$, a modulation equation

$$F_\tau = cF_X, \quad \text{with } Z = X - c\tau, \quad F(x,\tau,T) = F(Z,T), \quad c = \cos\left(\frac{k}{2}\right), \tag{1.3.14}$$

- at $\mathcal{O}(\varepsilon^2 e^{2i\theta})$, second harmonic correction

$$\omega^2 G_2 = \sin^2(k)(G_2 + aF^2) \quad \Rightarrow \quad G_2 = a\cot^2\left(\frac{k}{2}\right)F^2, \tag{1.3.15}$$

- at $\mathcal{O}(\varepsilon^3 e^{i\theta})$, the (NLS) equation arises

$$\begin{aligned} iF_T + F_{\tau\tau} = F_{XX}\cos k - 12b|F|^2 F\sin^2\left(\frac{k}{2}\right) \\ - 8a\sin^2\left(\frac{k}{2}\right)\left[F(G_0 + G_0^*) + F^* G_2\right], \end{aligned} \tag{1.3.16}$$

where $G_0 = -a\csc^2\left(\frac{k}{2}\right)|F|^2$.

Reduction to Standard NLS equation Form: by expressing this in the standard form and changing variables (1.3.14), we get

$$iF_T = DF_{ZZ} + B|F|^2 F, \tag{1.3.17}$$

with

$$D = \frac{1}{4}\sin\left(\frac{k}{2}\right), \quad B = \frac{2a^2\cos^2\left(\frac{k}{2}\right) - 4a^2 + 3b\sin^2\left(\frac{k}{2}\right)}{\sin^2\left(\frac{k}{2}\right)}.$$

The reduction results in an NLS equation with (1+1)-dimensions that are either focusing, i.e. $BD > 0$, or defocusing $BD < 0$. The standard breather solution of the NLS equation is

$$F(Z,T) = A\exp\left(\frac{iBA^2T}{2}\right)\operatorname{sech}\left(AZ\sqrt{\frac{B}{2D}}\right), \tag{1.3.18}$$

where A is breather amplitude.

Wattis *et al.* [22] extended and improved upon earlier work [21] by applying an asymptotic reduction approach, which reduces the FPU lattice equations to a modified Korteweg–de Vries (mKdV) equation. This equation is integrable and supports interactions between multiple solitons, including breather-kink

solutions. The ansatz solution is given in the form

$$u_m(t) = \varepsilon F(x_1, t_1, x_2, t_2, \dots) + \varepsilon^2 G(x_1, t_1, x_2, t_2, \dots) + \\ + \varepsilon^3 H_3(x_1, t_1, x_2, t_2, \dots) + ... + c.c, \tag{1.3.19}$$

where $x_j = \varepsilon^j n, \quad t_j = \varepsilon^j t, \quad (j \in \mathbb{N})$. By equating terms at equal orders of $\varepsilon \ll 1$, the resulting mKdV equation takes the form

$$0 = 4F_T + \ DF_{ZZZ} + 3bF^2F_Z. \quad D = \frac{1}{12}, \ \ b > 0, \tag{1.3.20}$$

where $z = x_1 - t_1$, $\tau = t_1$, $T = t_3 + x_3$, and $\quad Z = x_3 - t_3$. Wattis *et al* [22] employed the Bäcklund transformation, which is used in the study of integrable PDEs to construct explicit solutions; this transformation enables the construction of new solutions from the known ones, generating complex versions, such as combined breather-kink solutions.

Further, when this concept is extended to 2D lattices, such as square or hexagonal lattices, the phase θ generalises to

$$\theta = km + hln + \omega(k, l)t, \tag{1.3.21}$$

where k and l are the wave numbers in the two spatial directions, m and n denote the positions along the respective axes and $\omega(k, l)$ is the corresponding frequency.

For a square lattice, where the axes are orthogonal, the parameter $h = 1$. However, in hexagonal lattices, where the axes are angled, $h = \sqrt{3}$, reflecting the different geometric structure. This formulation allows for an accurate description of both the symmetry and dimensionality of wave propagation in different lattice types. Here, we follow [23–26].

The aim is to find the leading-order expressions for the functions G_i, H_i, and F, where $i = 1, 2, \ldots$. This method proceeds order by order in ε, collecting harmonics in the expansion of $u_m(t)$ and $v_n(t)$. At each order, resonant terms (such as $e^{i\theta}$) may introduce secular growth, unless they are cancelled by suitable corrections to the amplitude or by satisfying a solvability condition. In this way, the solution is systematically constructed by balancing fast oscillations and slow modulations at each order.

1.4 Literature review

1.4.1 Background and motivation

The FPUT system was among the earliest numerical experiments in nonlinear dynamics [27]. It revealed the unexpected recurrence of initial conditions after long simulations, now known as FPUT *recurrence*. This phenomenon sparked extensive research in nonlinear wave propagation. Zabusky and Kruskal [28] later explained recurrence in the Korteweg–de Vries (KdV) equation in terms of elastic collisions between travelling waves, introducing the concept of solitons. Since then, many nonlinear wave structures have been studied, including discrete breathers and breather–kink modes. Discrete breathers are spatially localised and time periodic solutions in nonlinear lattices. They have attracted significant attention due to their role in energy localisation in coupled oscillator systems. Rigorous existence and stability proofs for such solutions in conservative systems were established by MacKay and Aubry [29], using the anti-continuum limit approach, where coupling between (KG) lattice sites tends to zero. A more comprehensive review of mathematical and physical aspects of discrete breathers can be found in Flach and Willis [3]. The existence of breathers in the FPUT chain was proven by James [30], with generalisations for broader classes of FPUT-type models presented by Livi *et al.* [31].

1.4.2 The diatomic and monoatomic FPUT systems

In nonlinear lattice theory, monoatomic systems consist of identical particles, whereas diatomic systems alternate between two types of masses, typically labelled as "light" m and "heavy" M. The mass ratio $\rho = M/m$ and $0 < \rho < 1$ between these particles significantly shapes the chain's spectral and dynamical properties, especially regarding localised modes and wave propagation.

Vainchtein *et al.* [32] captured both slow and fast timescale dynamics for $\rho \ll 1$, linking the original system to an effective nonlinear envelope equation. Unlike earlier WKB-based approaches when focused on fast dynamics [33], their method yielded more accurate approximations particularly through Padé-type expansions which were effective for modelling the slow dynamics [34].

Pelinovsky *et al* [35] recently derived error bounds for approximating diatomic system dynamics using a monoatomic model for small mass ratio limit $\rho \ll 1$. Their energy analysis ensures long-term accuracy, particularly when large mass displacements remain small.

Monoatomic FPUT chains subjected to longitudinal tension support rich transverse wave dynamics, including stable soliton solutions. Cadet [36] explored monoatomic chain and identified both linearly and circularly polarised envelope solitons. By reformulating the system in complex variables and applying semi-discrete approximations, he reduced the dynamics to a NLS equation (see Section 1.2) that governs the envelope evolution. This model revealed how longitudinal-transverse coupling can generate localised wave structures. In subsequent work [37], Cadet included tension effects and examined how longitudinal displacements impact transverse mode stability. He found that circularly polarised solitons are generally robust, while linearly polarised waves show stability only under specific material and wave parameters. Later [38] expanded the model to include higher-order nonlinearities, identifying stability regimes for transverse waves and showing that linearly polarised solitons often

transition to elliptical polarisation upon interacting with other waves.

Collectively, these studies show that both monoatomic and diatomic FPUT systems exhibit a wide variety of localised excitations. Their dynamics depend sensitively on parameters such as mass ratios, interaction strengths and lattice geometry.

1.4.3 Second neighborhood interaction

Second-neighbour interaction (SNI) extends the concept of nearest-neighbour interaction (NNI) by allowing particles to influence others two lattice sites away. These longer range interactions significantly affect lattice dynamics, particularly in biological and mechanical systems.

Christiansen *et al.* [39] investigated soliton dynamics in a zigzag lattice incorporating both NNI and SNI (Figure 1.4). Inspired by structures such as DNA strands and protein helices, their model permits longitudinal and transverse motion, capturing richer dynamical behaviour. In the absence of SNI, the system remains weakly nonlinear; its inclusion supports stable solitons, including kinks and breathers.

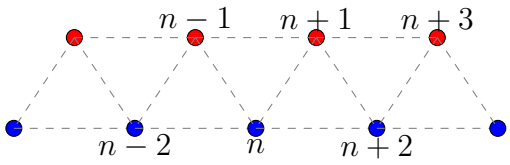

Figure 1.4: Illustration of a zigzag chain system where the red particles form the upper chain and the blue particles the lower.

Khusnutdinova *et al.* [2] developed a bilayer lattice model to examine wave propagation in systems undergoing delamination, where chains composed of distinct masses may separate in regions of weak interlayer bonding (Figure 1.5). Applying a long wave approximation, they derived coupled KG equations and showed that wave dynamics depend critically on the mass ratio; light upper chains dominate at low ratios; heavier lower chains at high ratios, and strong coupling enables energy exchange when masses are comparable. Further anal-

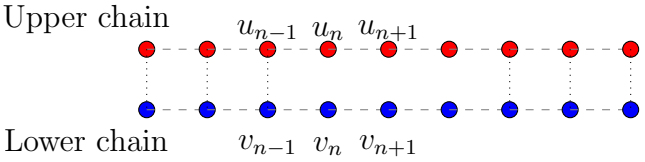

Figure 1.5: Illustration of model used in [2], with upper chain in red and lower in blue. The dashed (springs) lines show the upper chain and lower chain. Dashed black lines connect particles between the upper and lower chains.

ysis using Lie symmetry methods [40] yielded exact and self similar solutions standing waves, kink–kink structures and complex patterns whose behaviour varies with wave speed, amplitude and interlayer mass ratio. Extending this work, Khusnutdinova *et al.* [41] examined coupled dipole chains with soft bonding, revealing that weak coupling induces dispersive effects and leads to solitary waves with oscillatory, unstable tails.

Truskinovsky *et al.* [42] studied a monatomic mass spring chain with NNI and SNI, showing that the strength and sign of SNI are crucial for wave stability. Competitive interactions where SNI counteracts NNI can still support solitary waves, but with subsonic or supersonic speeds depending on system parameters.

Duran *et al.* [43] explored nonlinear lattices with long-range interactions via the α-FPU model. They demonstrated that solitary travelling waves become unstable when the derivative of wave energy with respect to velocity is negative. Together, these studies demonstrate that extending lattice models beyond NNI to include SNI and long-range coupling leads to fundamentally different wave phenomena, influencing the existence, shape and stability of nonlinear excitations in discrete media.

1.4.4 Mass-in-Mass systems

The mass-in-mass (MiM) lattice system, illustrated in Figure 1.6, consists of an infinite chain of identical beads, each coupled nonlinearly to its nearest

neighbour and internally connected to a resonator mass. While numerous studies have considered the case of linear interactions between inner and outer masses, MiM systems with nonlinear features continue to reveal rich dynamics.

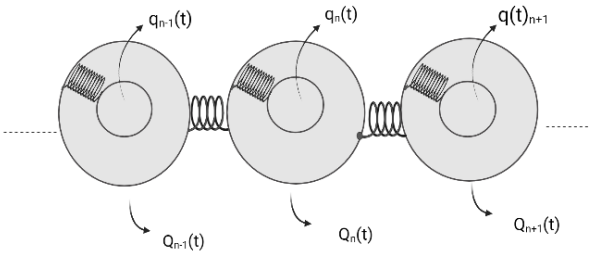

Figure 1.6: Mass-in-Mass (MiM) system: $q_n(t)$ is the inner mass, and $Q_n(t)$ is the outer mass. This configuration forms the basis for the MiM system studied in this thesis.

Kevrekidis *et al.* [44] explored the interaction between a defect and a train of solitary waves in a granular MiM chain, where a bead was coupled to an internal harmonic oscillator. Using asymptotic and numerical techniques, they demonstrated that the defect influenced wave propagation by reflecting part of the energy and trapping the rest in localised oscillations, a phenomenon absent in systems lacking the MiM structure.

Extending this work, Kevrekidis *et al.* [45] investigated travelling wave solutions in a chain of beads, each connected to an internal resonator. They identified "anti-resonance" conditions under which stable, pulse-like travelling waves emerge. Similarly, Liu *et al.* [46] studied discrete breathers in diatomic chains with linear internal resonators with mass m_2 and nonlinear outer interactions with mass m_1. By applying multiple-scale analysis (see Section 1.3.2), they reduced the system to a NLS equation (see Section 1.2), whose parameters are determined by the mass ratio $\rho = m_2/m_1$. Their results showed that for $0 < \rho < 2.356$, the NLS equation is focusing, supporting bright breather solutions. Even at large mass ratios (e.g. $\rho = 10$), the focusing behaviour persists. In contrast, as $\rho \to 0$, the system becomes defocusing, giving rise to dark solitons. Faver *et al.* [47] further examined solitary waves in related systems, showing that the MiM model reduces to a monatomic FPUT lat-

tice in two limiting cases: when the resonator mass is small; or when internal spring stiffness is large. These studies collectively demonstrate how internal resonators enrich the range of localised wave behaviours in diatomic lattices.

Wallen *et al.* [48] analysed discrete breathers in MiM chains, focusing on the impact of coupling stiffness κ. In the anti-continuum limit ($\kappa \to 0$), the system supports highly localised, single-site breathers. As κ increases, these structures broaden but remain localised due to nonlinearities, with the governing equations reducing to an NLS-type equation.

Bonanomi *et al.* [49] conducted experimental, numerical and theoretical studies of travelling waves in MiM chains composed of aluminium outer masses, steel inner masses, and a polymer spring. Their work showed that internal resonator vibrations can filter mechanical waves within tunable frequency bands adjustable via static pre compression leading to localised modes.

Porter *et al.* [50] explored the propagation of highly nonlinear solitary waves in Hertzian bead chains. They compared wave shapes and speeds across different dimer configurations, such as alternating light and heavy beads, as well as sequences consisting of N heavy beads followed by one light bead. Their analysis combined experimental observations with long wave asymptotics, revealing how nonlinear contact mechanics shape wave propagation.

Theocharis *et al.* [51] studied breather-kink solutions in compressed diatomic chains of alternating heavy and light beads. They found two types of discrete gap breathers: one centred on a heavy bead (unstable across all frequencies); and another on a light bead, which is stable over a broad frequency range.

Recently, Wattis [1] provided an analytical study of the MiM system using multiple-timescale analysis (see Section 1.3.2). He demonstrated that, under certain linear coupling and nonlinear interactions, the system reduces to an NLS equation. However, when both inner and outer interactions exhibit quadratic nonlinearities, the reduction leads to a Complex Ginzburg–Landau (CGL) equation instead. These results motivate the numerical investigations presented in Chapter 2.

1.4.5 Discrete breathers in two dimensions

In nonlinear lattice studies, the term "hexagonal lattices" can refer to distinct but related geometries, including honeycomb, triangular or kagome lattices. Although all exhibit hexagonal symmetry, their structural differences have significant implications for wave propagation, breather dynamics and potential applications in metamaterials.

Honeycomb and triangular lattices, for example, differ in unit cell composition and neighbour connectivity. The honeycomb lattice (on left of Figure 1.7) features two nodes per unit cell, whereas the triangular lattice (on right) connects each node to six equidistant neighbours. While hexagonal lattices are less studied than square lattices in mechanical contexts, understanding their behaviour may inform the design of advanced materials.

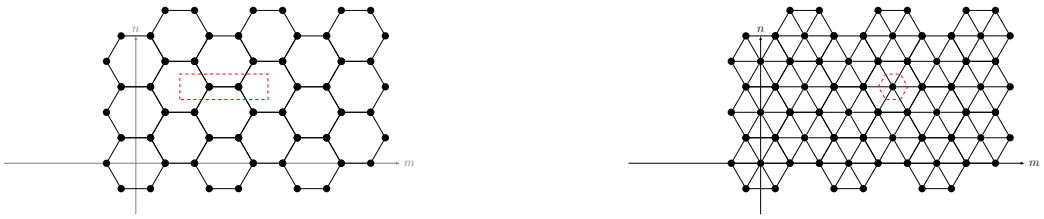

Figure 1.7: Left: Honeycomb lattice with red rectangle highlights the unit cell. Right: Triangular lattice with the unit cell outlined in red; axes are labelled as m and n.

Marín *et al.* [52] were among the first to study discrete breathers in 2D sine-Gordon triangular lattices. They found that breathers could propagate with minimal dispersion in specific directions, particularly when initial perturbations deviated by 15° from the lattice axis. By incorporating nonlinear couplings between atoms in adjacent planes and applying an onsite potential, they revealed that hexagonal symmetry supports directionally mobile breather solutions.

Bajars *et al.* [53] extended this model to include more general atomic interactions. Their results demonstrated the formation of long lived mobile breathers that retain energy and remain spatially localised over time. In particular, these breathers exhibit frequency focusing: initial oscillations gradually narrow into

a single dominant frequency band, enhancing temporal coherence and reducing dispersion.

Kevrekidis *et al.* [54] examined breather stability in 2D KG and FPUT models. They linked stability to the derivative $H'(\omega)$, where $H(\omega)$ is the system's energy as a function of frequency for hard and soft nonlinear potentials, providing a general framework for assessing breather stability across lattice types. The stability of a breather with respect to $H'(\omega)$ depends on the type of potential. If $H'(\omega) > 0$, the breather is stable in hard potentials and unstable in soft potentials. Conversely, if $H'(\omega) < 0$, the breather is stable in soft potentials and unstable in hard potentials.

These insights into discrete breather dynamics in 2D lattices provide a foundation for exploring their dynamics across different physical settings, including electrical and mechanical lattice systems.

1.4.6 Electrical and mechanical lattices

The 2D square electrical transmission lattice (ETL) consists of repeating unit cells comprising two linear inductors and a nonlinear capacitor. Butt and Wattis [24] analysed such systems, based on the FPUT lattice, by applying Kirchhoff's laws to derive governing equations for charge dynamics at each site. Through a multiple-scale asymptotic expansion (see Section 1.3.2), they identified small amplitude breather solutions localised in both spatial directions. The envelope of the breather evolves according to a reduced 2D NLS equation, with ellipticity conditions on wave numbers constraining the breather's speed, frequency and profile.

This approach was later extended to other geometries. In [23], triangular lattices were examined, while honeycomb lattices were considered in [55]. In both cases, similar asymptotic techniques were applied, yielding comparable breather solutions. These studies incorporated both quadratic and cubic nonlinearities and continued to rely on Kirchhoff's framework for charge evolution.

Parallel developments occurred in mechanical systems. Wattis and Alzaidi [26] investigated a 2D square mechanical lattice with each node connected by nonlinear springs to its nearest neighbours and by linear springs to diagonal ones. Each node moved freely within the plane and was subject to an onsite potential. A multiple-scale analysis (see Section 1.3.2), led to a generalised KG system, which was reduced to a (2+1)-dimensional NLS equation. The existence of breathers was shown to depend on both ellipticity and focusing conditions.

Although considerable attention has been devoted to square, triangular and honeycomb geometries, the Kagome lattice characterised by its unique symmetry and band structure remains relatively underexplored in mechanical contexts. Its ability to sustain localised wave phenomena in mechanical systems remains less well understood, despite extensive studies in photonic and topological contexts. Some progress has been made in identifying localised modes in Kagome structures [56–61], yet many questions remain.

In contrast to the well established electrical models of triangular and honeycomb lattices, their mechanical analogues particularly in the context of small amplitude breathers have not been systematically studied. This thesis addresses this gap by investigating breather existence and behaviour in 2D mechanical triangular and honeycomb lattices, as presented in Chapters 3 and 4.

1.4.7 Application: metamaterials

Metamaterials are artificially engineered structures designed to exhibit properties not typically found in natural materials. Their unique geometries allow them to manipulate energy mechanical, optical or acoustic in unconventional ways. Increasingly, DBs have been observed in various metamaterial configurations, both theoretically and experimentally.

Koukouloyannis *et al.* [62] studied 1D nonlinear left handed metamaterials (LHMs), characterised by a negative refractive index in which energy propagates opposite to the wave vector. Using a multiple scale asymptotic expansion

(see Section 1.3.2), they reduced the governing equations to a NLS equation (see Section 1.2), thereby demonstrating the existence of bright breather solutions.

In a mechanical context, Duran *et al.* [63] modelled a metamaterial composed of square rigid units connected via flexible hinges, allowing rotational motion between neighbouring cells. Their system incorporated both translational and rotational degrees of freedom, and through asymptotic reduction, also yielded an NLS equation supporting discrete breather solutions.

Experimental confirmation of such behaviours has emerged in several systems. For example, Deng *et al.* [64] reported the observation of solitary travelling waves in rotating square metamaterials, where square units are connected by flexible hinges and rotate about their corners or centres. These structures have been proposed for applications in waveguiding and mechanical signal processing.

Chong *et al.* [65] reviewed nonlinear wave dynamics in granular crystal chains mechanical metamaterials governed by FPUT models. They highlighted the influence of mass variation and geometric configuration on wave propagation. Specially, increasing the mass ratio in diatomic chains leads to wave attenuation, while smaller ratios promote resonant wave transmission. Strong interparticle interactions yield fast, highly localised waves with strong nonlinearity; in contrast, weak interactions result in slower, less localised dynamics.

Together, these studies demonstrate the versatility of metamaterials in supporting discrete breathers, with structural parameters such as mass ratio, geometry and coupling strength playing key roles in determining wave behaviour.

1.5 Overview of the Thesis

This thesis presents a comprehensive study of discrete nonlinear lattice systems, focusing on the dynamics of soliton-like structures, including breathers, travelling waves and kink solutions. It is organised into five chapters, each

addressing distinct aspects of nonlinear wave behaviour in 1D and 2D lattice configurations through analytical and numerical methods.

Chapter 1 introduces soliton phenomena and highlights the role of discrete nonlinear systems in modelling complex dynamical behaviours. The chapter outlines various waveforms, in particularly, breather solutions, and their relevance in electrical, mechanical and metamaterial contexts.

Chapter 2 investigates the MiM FPUT system using numerical simulations. The study explores the interplay between outer masses and inner nonlinear oscillators and derives reduced models, including the NLS and CGL equations. The system is classified into four cases based on the presence or absence of quadratic nonlinearities a, α: Case I: $a = \alpha = 0$; (symmetric breathers); Case II: $\alpha \neq 0$, $a = 0$ (non-symmetric breathers); Case III: $a \neq 0$, $\alpha = 0$ (breather-kink); Case IV: $a \neq 0$, $\alpha \neq 0$ (CGL regime).

The analysis covers both optical and acoustic modes, considering various wave numbers k and mass ratios μ. Stability regions for stationary and moving breathers are mapped out. For instance, in the optical mode at $k = 0$, breathers in Cases I and III remain stable, while Cases II and IV show marginal or full instability depending on linear interaction ρ. Moving breathers are long-lived in Case I, while Cases II and III exhibit stability only for large ρ. Case IV, the NLS equation, applies only at $k = 0$ and $k = \pi$, where stationary breathers show marginal stability for large ρ, while at $k = 0.1$ and 3.1, the system yields a CGL equation.

Chapter 3 develops a 2D mechanical triangular lattice model in which each node connects to six neighbours, forming a hexagonal pattern. The analysis distinguishes between optical and acoustic modes via dispersion relations, and derives a generalised KG system. Through multiple-scale analysis, the system reduces to a 2D NLS equation. Ellipticity and focusing conditions for breather existence are identified. This work is currently under preparation for publication.

Chapter 4 extends the analysis to a mechanical honeycomb lattice, composed

of left- and right-facing nodes within each unit cell. Using the multiple-scale method, the reduced dynamics are shown to yield distinct forms of NLS equations, depending on the wave vector (k, l). Five distinct cases are identified: Case 1: global minimum; Case 2: global maximum; Case 3: Dirac point refers to a conical intersection in the dispersion surface where two branches meet at a single point; Cases 4 and 5: acoustic and optical saddle points, respectively.

In Cases 1 and 2, the reduction leads to coupled NLS equations, while in Cases 4 and 5, the system reduces to a single (2+1)-dimensional NLS equation. Case 4 supports stationary breather modes, whereas the optical saddle (Case 5) does not. This chapter also is being prepared for publication.

Chapter 5 concludes the thesis by summarising the key results across all chapters. It also outlines several open questions and directions for future research, particularly concerning breather dynamics in 2D mechanical lattices and potential extensions to other geometrical configurations.

Chapter 2

Numerical simulation of a fully nonlinear mass-in-mass FPUT chain

This chapter presents numerical simulations of discrete breathers in the fully nonlinear MiM FPUT system. In this model, each outer mass is coupled to its nearest neighbours and to an inter nal nonlinear oscillator, creating a complex network of interactions. We focus specifically on the case where both the internal couplings and NNIs are governed by nonlinear forces.

The simulations confirm that the MiM FPUT system supports a variety of breather solutions, including stationary breathers both stable and unstable as well as breather-kink forms. Further, the results show the existence of moving breather and breather-kink solutions, which, even though unstable, exhibit long-lived behaviour before decay. This interplay between stability and instability highlights the diverse nonlinear behaviour of the MiM FPUT system and enhances our understanding of the mechanisms driving the emergence and longevity of these localised excitations.

2.1 Introduction

In this chapter, we numerically simulate a fully nonlinear MiM FPUT chain. We consider the case where all interactions have nonlinear components, following Wattis [1]. We simulate the system with different combinations of quadratic and cubic nonlinearities, and investigate the robustness properties of various breather and breather-kink modes derived therein. The system's linear frequency spectrum comprises two branches: an "optical" branch of higher frequency modes, and a lower-frequency "acoustic" branch. Nonlinear modes may exist in the gap between these, and above the optical branch. In Section 2.2 we summarise the asymptotic analysis of the fully nonlinear MiM chain, then we use solutions from this weakly nonlinear analysis as initial conditions for simulations. In sections 2.3 to 2.7, results of our simulations on stationary and moving modes are presented, illustrating the robustness and stability of these modes in terms of their lifetimes and measurements of decay rates. In section 2.13, we discuss the significance of these results and finish with concluding remarks.

2.2 Numerical investigation of breathers and breather-kink modes

2.2.1 The model

Here, we focus on the breather solution, that is, modes with small amplitude and whose envelope varies slowly over both space and time compared to the linear carrier oscillations. We summarise the asymptotic results of [1], using n to denote the position of the mass along the lattice or chain; the displacements of the outer oscillators of mass m are defined by $q_n(t)$, and the corresponding momenta are defined by $p_n(t)$. These outer particles are connected to their nearest neighbours ($n\pm1$), as well as to their inner masses (M), whose displace-

ments and momenta are given by $Q_n(t)$, $P_n(t)$, respectively. The equations of motion are derived from the Hamiltonian

$$H = \sum_n \frac{p_n^2}{2m} + \frac{P_n^2}{2M} + V(q_{n+1} - q_n) + W(q_n - Q_n), \tag{2.2.1}$$

where the potential energies, with a, α, b, β denoting the coefficients of the cubic and quartic nonlinear terms respectively, are given by

$$V(\phi) = \frac{\phi^2}{2} + a\frac{\phi^3}{3} + b\frac{\phi^4}{4}, \qquad W(\psi) = \rho\frac{\psi^2}{2} + \alpha\frac{\psi^3}{3} + \beta\frac{\psi^4}{4}, \tag{2.2.2}$$

for some linear interaction $\rho > 0$, with a, b, α, β of either sign. The equations of motion are thus

$$\begin{aligned} m\frac{d^2 q_n}{dt^2} &= \mathcal{F}_1(q_n, Q_n) := V'(q_{n+1} - q_n) - V'(q_n - q_{n-1}) - W'(q_n - Q_n), \\ M\frac{d^2 Q_n}{dt^2} &= \mathcal{F}_2(q_n, Q_n) := W'(q_n - Q_n). \end{aligned} \tag{2.2.3}$$

A small parameter $\varepsilon \ll 1$ is introduced, which is proportional to the amplitude of the breather solution; the mass ratio is defined by $\mu = M/m$. A large space scale $y = \varepsilon n$ and two long timescales $\tau = \varepsilon t$, $T = \varepsilon^2 t$ are introduced to make use of multiple-scale methods [20]. To find general breather modes, we use the ansatz

$$\begin{aligned} q_n(t) &= \varepsilon e^{i\theta} F_1(y, \tau, T) + \varepsilon F_0(y, \tau, T) + \varepsilon^2 [e^{2i\theta} G_2 + e^{i\theta} G_1 + G_0] \\ &\quad + \varepsilon^3 [e^{3i\theta} H_3 + e^{2i\theta} H_2 + e^{i\theta} H_1 + H_0] + ... + c.c, \end{aligned} \tag{2.2.4}$$

$$\begin{aligned} Q_n(t) &= \varepsilon e^{i\theta} P_1(y, \tau, T) + \varepsilon P_0(y, \tau, T) + \varepsilon^2 [e^{2i\theta} S_2 + e^{i\theta} S_1 + S_0] \\ &\quad + \varepsilon^3 [e^{3i\theta} R_3 + e^{2i\theta} R_2 + e^{i\theta} R_1 + R_0] + ... + c.c, \end{aligned} \tag{2.2.5}$$

where $e^{i\theta}$, with $\theta = kn - w(k)t$ describes the carrier wave; $F_j(y, \tau, T)$; $P_j(y, \tau, T)$ are the leading order shapes of the envelope and zero mode; and $G_j; H_j; S_j; R_j$ are higher-order correction terms in ε, which are all functions of (y, τ, T). These define the amplitudes of higher harmonic correction terms to the fun-

damental modes, which are generated by nonlinearities. After substituting these formulae into the equations of motion (2.2.3), all terms are expanded in powers of ε. The time derivative is expanded as $d/dt = \partial_t + \varepsilon\partial_\tau + \varepsilon^2\partial_T$. By combining terms with equal powers of ε and frequencies $e^{ij\theta}$, $j = 0, 1, 2, ...$, a sequence of connected pairs of equations determines the form of the envelopes $F_j; P_j; G_j; S_j$, etc.

As a result of equating terms at $\mathcal{O}(\varepsilon e^{i\theta})$, nonzero solutions for P_1, F_1 must satisfy the dispersion relation

$$\begin{aligned} \omega^2 &= \frac{1}{2mM}\left[\rho M + \rho m + 4M\sin^2\frac{k}{2} \pm \sqrt{D}\right], \\ D &= \left(\rho M + \rho m + 4M\sin^2\frac{k}{2}\right)^2 - 16Mm\rho\sin^2\frac{k}{2}. \end{aligned} \tag{2.2.6}$$

This has two branches: acoustic, ω_{ac} with a lower frequency, corresponding to the " $-$ " sign in (2.2.6); and optical, ω_{op} that has higher frequency, corresponding to " $+$ " sign in (2.2.6). In the zero limit of wave number k, the speed of sound c_0 is obtained as

$$c_0 = \lim_{k\to 0}\frac{\omega_{ac}(k)}{k} = \frac{1}{\sqrt{m(1+\mu)}}. \tag{2.2.7}$$

In both acoustic and optical cases, the ratio of the amplitude of inner and outer mass oscillations, $C(k) = P_1/F_1$, is given by

$$C(k) = \frac{\rho}{\rho - M\omega(k)^2}. \tag{2.2.8}$$

As the parameters ρ, μ change, the system exhibits various behaviours. To demonstrate these, we consider mass ratios μ on both sides of unity, namely 3 and 1/3, as well as spring constants above and below unity, namely $\rho = 1/3$, and 3. At $\mathcal{O}(\varepsilon^2 e^0), \mathcal{O}(\varepsilon^2 e^{2i\theta})$, we find expressions for the second and zeroth harmonics G_2, Q_2, G_0, Q_0. At $\mathcal{O}(\varepsilon^2 e^1)$, we obtain the corrections to the leading order mode and the speed of the envelope c, so that subsequent terms can be

written in terms of the travelling wave coordinate $Z = y - c\tau$.

At $\mathcal{O}(\varepsilon^3 e^{i\theta})$, corrections terms G_i combine with the leading order terms F_0, F_1, to yield the NLS or CGL equation

$$i\Omega F_{1,T} = D_3 F_{1,ZZ} + (\eta + i\zeta)|F_1|^2 F_1, \tag{2.2.9}$$

where

$$\begin{aligned}
\Omega &= -\frac{2m\omega(\rho + \mu\rho C - \mu m\omega^2)}{(\rho - \mu m\omega^2)}, && (2.2.10)\\
D_3 &= \frac{(\mu m\omega c)^2 C}{\rho - \mu m\omega^2} + (1+\mu C)mc^2 - \cos k \\
&\quad +2\rho\gamma_1(\sin k - (1-\mu)m\omega c), && (2.2.11)\\
\eta &= \frac{\mu m\omega^2(C-1)}{(\rho - \mu m\omega^2)}[3\beta(C-1)^2 + 2\alpha(\hat{\alpha}_g - \hat{\alpha}_s) + 4(\gamma_0 - \sigma_0)] \\
&\quad +48b\sin^4\frac{k}{2} + 16a^2\phi_0\sin^2\frac{k}{2} + 32a\hat{a}_g\sin^3\frac{k}{2}\cos\frac{k}{2}, && (2.2.12)\\
\zeta &= 32a\hat{\alpha}_g\sin^3\frac{k}{2}\cos\frac{k}{2} - \frac{2\alpha\mu m\omega^2(C-1)(\hat{a}_g - \hat{a}_s)}{(\rho - \mu m\omega^2)}, && (2.2.13)
\end{aligned}$$

where ϕ_0, $\hat{\alpha}_g$, $\hat{\alpha}_s$, γ_0, σ_0, $\hat{a}_g$, and $\hat{a}_s$ are given in [1]. Thus, the NLS equation (2.2.9) has been obtained, with an additional ζ term in front of the nonlinearity. If one or both of α and a are equal to zero, and if

$$\eta D_3 > 0, \tag{2.2.14}$$

then we have the focusing form of NLS and localised breather solutions are given by

$$F_1 = Ae^{-i\eta A^2 T/2\Omega}\text{sech}\left(AZ\sqrt{\frac{\eta}{2D_3}}\right), \tag{2.2.15}$$

where A is the amplitude and $Z = y - c\tau$ is a coordinate system moving with the wave. From equations of $\mathcal{O}(\varepsilon^3 e^{0i\theta})$ the zero mode, F_0 is determined by

$$F_0 = \frac{4Aa\sin^2(\frac{k}{2})}{(1+\mu)mc^2 - 1}\sqrt{\frac{2D_3}{\eta}}\tanh\left(AZ\sqrt{\frac{\eta}{2D_3}}\right), \tag{2.2.16}$$

which has the form of a kink travelling at speed c. This term only enters 2.2.4-2.2.5 when $a \neq 0$.

The behaviour of the system can be classified into four cases depending on the presence or absence of quadratic nonlinearities, namely:

- Case I: $\alpha = 0$, $a = 0$, where $F_0 = 0$, so breathers have the classic form and are symmetric (in that $q_n(t + \frac{T_p}{2}) = -q_n(t)$, where T_p is the period of oscillation, with a similar result holding for $Q_n(t)$);

- Case II: $\alpha \neq 0$, $a = 0$, where $F_0 = 0$, so breathers have the classic form (but are not symmetric);

- Case III: $\alpha = 0$, $a \neq 0$, where $F_0 \neq 0$, so modes are a combination of breather; and kink forms (the breather component being symmetric);

- Case IV: $\alpha \neq 0$, $a \neq 0$, where $F_0 \neq 0$ and, for general k, $\zeta \neq 0$ so (2.2.9) is CGL. However, at some values of the wavenumber k, such as $k = 0, \pi$, $\zeta = 0$ and the NLS will still be relevant. In such cases, the mode is a combination of breather and kink.

2.2.2 Numerical implementation

In this section, we explain the numerical simulation algorithm used to solve the equations of motion governing the MiM lattice (2.2.3). This infinite set of coupled second-order nonlinear ordinary differential equations are truncated to finite size N, and periodic boundary conditions (BCs) are applied. Typically, we choose lattice sites with $N \geq 200$ for wave numbers $k = 0, \pi$, since these wave numbers give stationary modes. We initiate the simulation with the wave centred at lattice site $n = N/2$. For other wave numbers, e.g. $k = 0.1, 3.1$, we use larger values of $N \geq 10^3$, since these cases allow moving waves, and we wish to follow the system's evolution for a considerable time ($t \sim 10^3$) without the body of the wave interacting with the boundary conditions. In these cases, we start the simulation with the mode at lattice site $N/4$ and with velocities

chosen so that it starts moving towards the centre.

We use the analytic equation for breather solutions presented in (2.2.15) and (2.2.16) to construct initial conditions setting $t = 0$ to determine initial data of (2.2.3) at each lattice site. From (2.2.15)- (2.2.16), we obtain

$$\begin{aligned} q_n(0) &= 2\varepsilon A\cos\left((kn-n_0)-\frac{\varepsilon^2A^2\eta(k))}{2\Omega(k)}\right)\operatorname{sech}\left(\varepsilon A(n-n_0)\sqrt{\frac{\eta(k)}{2D_3(k)}}\right) \\ &\quad +\frac{4Aa\sin^2(\frac{k}{2})}{(1+\mu)mc^2-1}\sqrt{\frac{2D_3}{\eta}}\tanh\left(AZ(n-n_0)\sqrt{\frac{\eta}{2D_3}}\right), \end{aligned} \tag{2.2.17}$$

from the leading order terms in (2.2.4)–(2.2.5), $q_n = \varepsilon F_0 + \varepsilon \mathbf{e}^{i\theta}F_1 + c.c.$ and $Q_n = \varepsilon F_0 + \varepsilon \mathbf{e}^{i\theta}CF_1 + c.c.$, and corresponding expressions for the initial velocities $p_n(0)/m = dq_n/dt|_{t=0}$ and $P_n(0)/M = Cp_n(0)$. We introduce the concept of the breather's half-height width, which helps determine the spread of the solitary wave. From (2.2.15), the width W_b is given by

$$W_b = \frac{2\log(2+\sqrt{3})}{\varepsilon A}\sqrt{\frac{2D_3}{\eta}}. \tag{2.2.18}$$

This width W_b helps us identify suitable parameter values of bright breathers, as illustrated in figure 2.1. If the width is too large (e.g. $W_b > 100$), then an extremely large value of N would be required, and so it is difficult to perform numerical simulations. If the width is too narrow (e.g. $W_b < 10$), then the quasi-continuum approximation used in the asymptotic analysis is not valid, and we would not expect the approximate breather solution (2.2.4)–(2.2.5) to be accurate where the breather may fall between two lattice sites. Hence, we choose values for b, β so that the width is at least ten lattice sites, but not so large that computations become impractical.

We use the MATLAB package ode45 to solve the equations of the motion (2.2.3). This is 4^{the} or 5^{the}-order Runge-Kutta-Fehlberg (RKF45). In section 2.3 and 2.7, we present our findings regarding simulations of stationary and

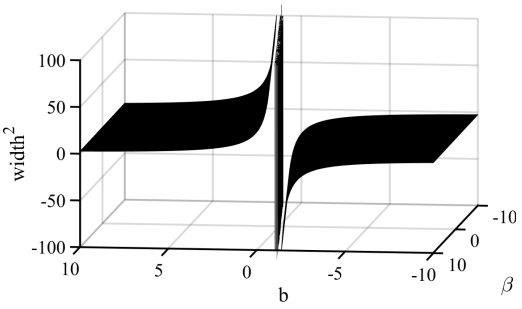

Figure 2.1: Plot of squared width of breather against parameter values of β and b for optical case I: $a = \alpha = 0$ when $k = \pi$ and $\rho = 3, \mu = 3$. The region where squared width is negative corresponds to the defocusing case.

moving breathers in MiM lattices in the four cases listed at the end of Section 2.2.1. We investigate whether the shape of the wave changes over time.

Since simulations are performed on a finite lattice, we choose to use periodic boundary conditions (BCs), which are implemented via

$$q_0(t) = q_N(t) - \Phi, \qquad q_{N+1}(t) = q_1(t) - \Phi, \tag{2.2.19}$$

$$\frac{d}{dt}q_0(t) = \frac{d}{dt}q_N(t), \qquad \frac{d}{dt}q_{N+1}(t) = \frac{d}{dt}q_1(t) \tag{2.2.20}$$

where Φ is the amplitude of any kink-component contained in the initial conditions (2.2.16), namely $\Phi = \lim_{N\to\infty} q_N(0) - q_{-N}(0) \neq 0$, or

$$\Phi = \frac{8Aa\sin^2(\frac{k}{2})}{(1+\mu)mc^2 - 1}\sqrt{\frac{2D_3}{\eta}} = \lim_{z\to\infty} F_0(z) - F_0(-z). \tag{2.2.21}$$

At early times, a small amount of radiation is sometimes emitted as the wave adjusts more precisely to the lattice. This radiation arises because the initial conditions are based on a leading-order, weakly nonlinear approximation. The transient radiation, resulting from initial conditions that only approximate the breather, does not propagate through the lattice or interfere with the main mode at later times. To mitigate this effect, we apply a small damping factor ($\lambda = 10^{-7}$) to the final 10% of lattice sites.

Hence for our numerical simulations, (2.2.3) is replaced by

$$\begin{aligned} \frac{d^2q_n}{dt^2} &= \mathcal{F}_1(q_n, Q_n) - \lambda\frac{dq_n}{dt}, \qquad (2.2.22) \\ \frac{d^2Q_n}{dt^2} &= \mathcal{F}_2(q_n, Q_n) - \lambda\frac{dQ_n}{dt}, \qquad (1 \le n \le N/10 \quad \text{and} \quad 9N/10 \le n \le N), \end{aligned}$$

where $\mathcal{F}_1(q_n, Q_n), \mathcal{F}_2(q_n, Q_n)$ are given by (2.2.3), and typically $N \approx 10^3$.

2.2.3 Numerical assessment of robustness

k	Type	Case	Waveform	Stability
0	Opt	I	Breather	Stable
0	Opt	II	Breather	Marginal (large ρ), Unstable (small ρ)
0	Opt	III	Breather	Stable
0	Opt	IV	Breather	Unstable
π	Opt	I	Breather	Stable
π	Opt	II	Breather	Marginal (large ρ, small μ)
π	Opt	III	Breather-Kink	Stable (large ρ, small μ)
π	Opt	IV	Breather-Kink	Stable (large ρ, small μ)
π	Ac	I	Breather	Stable
π	Ac	II	Breather	Unstable (small ρ), Marginal (large ρ)
π	Ac	III	Breather-Kink	Stable small (ρ)
π	Ac	IV	Breather-Kink	Unstable

Table 2.1: Summary of stability status of stationary breather modes based on numerical simulations of fully nonlinear MiM FPUT lattice: Case I corresponds to $a = 0 = \alpha$; Case II to $a = 0 \neq \alpha$, Case III to $a \neq 0 = \alpha$, and Case IV to $a \neq 0 \neq \alpha$. α, a are coefficients of quadratic nonlinear in 2.2.2.

We local energy $e_n(t)$ investigate the position and lifetime of breather modes and to confirm the validity of asymptotic analyses. We aim to understand whether the energy remains localised or disperses. We define the local energy at lattice site n at time t as

$$e_n(t) = \frac{p_n^2}{2m} + \frac{P_n^2}{2M} + \frac{1}{2}\left(V(q_{n+1} - q_n) + V(q_n - q_{n-1})\right) + W(q_n - Q_n). \quad (2.2.23)$$

The *total* energy is then $H = \sum_{n=1}^{N} e_n(t)$, which should be constant. While $q_n(t)$ and $Q_n(t)$ oscillate rapidly in both n and t, the quantity $e_n(t)$ is strictly positive and varies much more slowly over both n and t. Consequently, $e_n(t)$

is a much more useful way of determining the location of the breather mode at each value of t. In particular, the breather location can be defined by

$$L(t) = \frac{\sum_n n e_n^v(t)}{\sum_n e_n^v(t)}, \qquad (v \geq 1), \tag{2.2.24}$$

where the exponent $v \geq 2$ gives us the L_v norms. This is particularly important for moving breathers, where $L(t)$ is used to determine the velocity of moving waves. After calculating the location of the breather, we measure the localised energy as the energy within two breather widths (2.2.18) of its location

$$LocEn(t) = \sum_{n=L(t)-W_b}^{L(t)+W_b} e_n(t), \qquad \Delta E = \frac{H(t) - LocEn(t)}{H(t)}. \tag{2.2.25}$$

Here, the relative change in the energy ΔE is given by the proportion of energy outside the breather. This quantity helps us determine how significant is energy loss to the rest of the lattice. The total energy $H(t)$ will only decrease from $H(0)$, due to the absorption of radiated energy by the ends of the lattice, because of the damping terms λ in (2.2.22). A summary of our study of stability, robustness and lifetime results is given in Tables 2.1 and 2.2.

2.3 Numerical Results for Stationary Modes

In this section, we consider three types of stationary breather: (i) optical breathers with $k = 0$, which are slowly varying over lattice sites n and have inner and outer particles moving out of phase (so that $\dot{q}_{n+1} \approx \dot{q}_n \approx \dot{Q}_n/C$ with $C < 0$); (ii) optical breathers with $k = \pi$, where nearest neighbours move out of phase, as well as inner and outer particles being out of phase (so that $-\dot{q}_{n+1} \approx \dot{q}_n \approx \dot{Q}_n/C$ with $C < 0$); and (iii) acoustic breathers with $k = \pi$, where inner and outer oscillators are in phase but neighbouring nodes are out of phase (so that $-\dot{q}_{n+1} \approx \dot{q}_n \approx \dot{Q}_n/C$ with $C > 0$). The fourth combination, of acoustic mode with $k = 0$, occurs when both motions are

Wave-number	Optical/ Acoustic	Case	Waveform	Stability / Lifetime
$k = 0$	Ac	cubic	Travelling kink	Long-lived
$k = 0$	Ac	quartic	Travelling kink	Splits in two
$k = 3.1$	Opt / Ac	I	Moving breather	Long-lived
$k = 3.1$	Opt	II	Moving breather	Long-lived for $\rho = 3, \mu = 1/3$
	Ac	II	Moving breather	Long-lived for $\rho = 3$
$k = 3.1$	Opt	III	Moving breather-kink	Long-lived for $\rho = 3, \mu = 1/3$
$k = 3.1$	Ac	III	Moving breather-kink	Long-lived for $\rho = 3, \mu = 3$
$k = 3.1$	n/a	IV	n/a - CGL with $\zeta \neq 0$	n/a
$k = 0.1$	Opt	I	Moving breather	Long-lived for $\rho = 3$, unstable for $\rho = 1/3$
$k = 0.1$	Opt	II	Moving breather	Long-lived for $\rho = 3$ Unstable for $\rho = 1/3$
$k = 0.1$	Opt	III	Moving breather	Long-lived
$k = 0.1$	n/a	IV	n/a/ - CGL since $\zeta \neq 0$	n/a
$k = 0.1$	Ac	I	Moving breather	Unstable
$k = 0.1$	Ac	II	Moving breather	Unstable
$k = 0.1$	Ac	III	(defocusing)	n/a
$k = 0.1$	n/a	IV	n/a - CGL since $\zeta \neq 0$	n/a

Table 2.2: Summary of stability status of moving kink, breather, and kink-breather waves based on numerical simulations of fully nonlinear MiM FPUT lattice: Case I corresponds to $a = 0 = \alpha$; Case II to $a = 0 \neq \alpha$, Case III to $a \neq 0 = \alpha$, and Case IV to $a \neq 0 \neq \alpha$.

in phase ($\dot{q}_{n+1} \approx \dot{q}_n \approx \dot{Q}_n/C$ with $C > 0$) and leads to kink-type travelling waves, which are considered separately in Section 2.8. In each of these cases, we discuss simulations of four sub-cases corresponding to smaller and larger values of the nearest-neighbour interaction constant ρ and smaller and larger values of the mass ratio μ.

2.4 Optical modes for $k = 0$

In this section, we systematically investigate the four fundamental cases that arise depending on whether the coefficients a and α of the quadratic nonlinearities are zero or non-zero. For each case, we explore two different values of the mass ratio, $\mu = 3, 1/3$ and the linear interaction strength $\rho = 3, 1/3$,

focusing on their impact on breather formation and stability.

2.4.1 Case I: even potentials ($a = 0 = \alpha$)

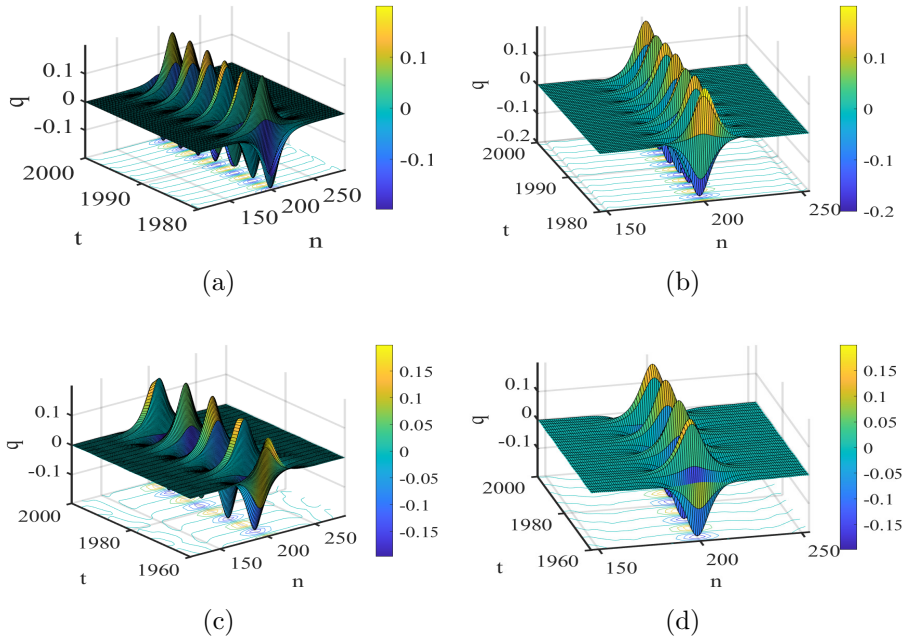

Figure 2.2: Stationary breather profiles for Optical Case I ($k = 0, \alpha = 0, a = 0$) showing $q_n(t)$ plotted against (n, t). Top row: $\rho = 3$; bottom row: $\rho = 1/3$; left column: $\mu = 3$; right column: $\mu = 1/3$. For full parameter values, see Table A.1 in Appendix A.

Figure 2.2 displays simulations for all combinations of weak ($\rho = 1/3$) and strong ($\rho = 3$) linear coupling, as well as small ($\mu = 1/3$) and large ($\mu = 3$) mass ratios. The selected parameters (b, β) satisfy the NLS focusing criterion (2.2.14) and yield suitable breather widths when $\varepsilon = 0.1$. In all cases, over 99% of the energy remains confined within the central breather width W_b. A small energy loss due to edge damping is observed, but remains negligible. Each simulation begins with the breather centred within the lattice. As shown in Figure 2.2, the breather maintains localisation throughout the entire simulation time ($t_{\text{end}} = 2000$), shedding only minor radiation.

Figure 2.2(d), corresponding to $\rho = 1/3$, $\mu = 1/3$, shows a localised breather. Figure 2.3(d) further supports this by illustrating parallel evolution of total energy $H(t)$ and localised energy $\text{LocEn}(t)$, indicating minimal radiation loss.

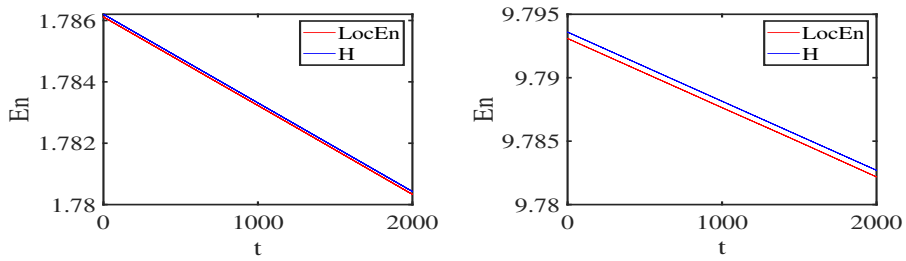

(a) Local and total energy

(b) Local and total energy

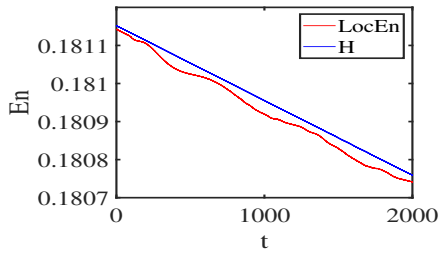

(c) Local and total energy

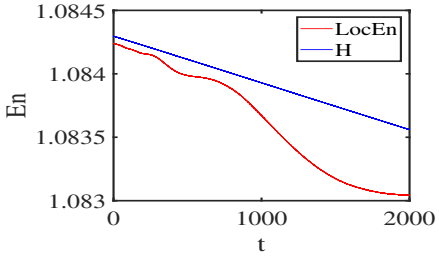

(d) Local and total energy

Figure 2.3: Time evolution of localised and total energy $H(t) = \sum_n e_n$ and LocEn(t) defined in (2.2.23) and (2.2.25), for $0 \leq t \leq 2000$, under Optical Case I. Top row: $\rho = 3$; bottom row: $\rho = 1/3$; left column: $\mu = 3$; right column: $\mu = 1/3$. See Table A.1 in Appendix A for parameter details.

The small gap between the two curves is consistent with minor energy loss due to damping at the lattice boundaries. Compared to Case (b), Case (d) demonstrates superior long term localisation and dynamic stability.

2.4.2 Case II: potentials at $(a = 0, \alpha \neq 0)$

We now examine the case where $\alpha = 1$, introducing a quadratic nonlinearity in the interaction between the inner and outer masses, while maintaining $a = 0$. We choose values for β and b that satisfy the focusing condition (2.2.14) and ensure that the resulting breather width remains within relevant range.

Figure 2.4 illustrates the qualitative behaviour of breather modes under varying strengths of linear coupling ρ and mass ratio μ. For strong coupling ($\rho = 3$), stationary breathers are long-lived regardless of the value of μ. In contrast, for weak coupling ($\rho = 1/3$), the breathers exhibit instability and decay quickly, again independently of the value of μ.

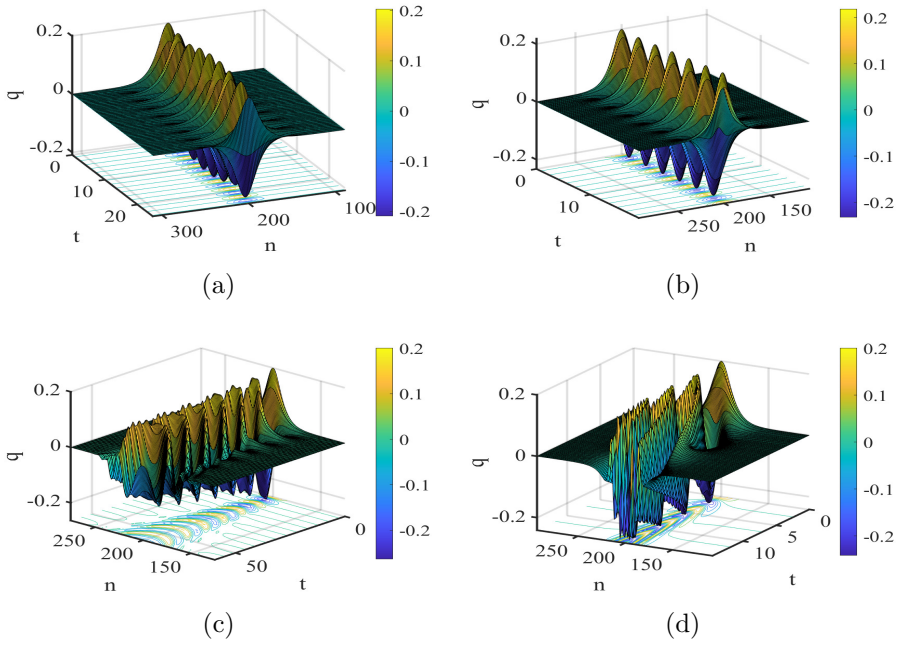

Figure 2.4: Evolution of $q_n(t)$ versus (n, t) for Optical Case II with $k = 0$, showing the central region of the lattice for early times ($N = 400$, $t = 1000$). Top row: $\rho = 3$; bottom row: $\rho = 1/3$; left column: $\mu = 3$; right column: $\mu = 1/3$. Full simulation parameters of Case II are provided in Table A.1 in Appendix A.

2.4.3 Case III: potentials at $(a \neq 0, \alpha = 0)$

Here, we investigate the case where only the along-chain interactions have quadratic nonlinearity, setting $a = 1$ and $\alpha = 0$. Although equation (2.2.16) permits breather-kink solutions for $a \neq 0$, the choice $k = 0$ eliminates the kink component, resulting in pure breather waves.

Simulations for this case, conducted with $t_{\max} = 1000$, $N = 1000$, and various values of β, demonstrate that the breather remains highly stable. No significant deformation or amplitude decay is observed in the interval $500 < t < 1000$. This confirms that the breathers in Case III are long-lived and structurally robust over time.

The corresponding simulation parameters for Case III are summarised in Table A.1 in Appendix A, including the values of β, W_b, and mass ratio μ under each (ρ, μ) configuration.

2.4.4 Case IV: the general case $(a \neq 0, \alpha \neq 0)$

We now consider the general scenario where both the along-chain and inner-outer mass interactions possess quadratic nonlinearities, setting $a = 1$ and $\alpha = 1$. The parameters are chosen to satisfy the focusing condition (2.2.14). Figure 2.5(a) and (b) show breather profiles over the intervals $0 < t < 250$ and $100 < t < 500$, respectively; panel (c) displays the local and total energy for $0 < t < 200$. The parameters are $b = 1$, $\beta = 2.98$, $W_b = 20.3510$, and $\omega = 0.6667$.

Unlike the stability seen in Case III, the breather mode in Case IV is short-lived. As shown in Figure 2.5, a rapid decline in amplitude occurs within the early simulation $0 < t < 200$. Panel 2.5(a) clearly illustrates the onset of breather destabilisation and energy dispersion around $t > 100$. Panel 2.5(c) confirms this with a sharp drop in localised energy, indicating a loss of coherence and structural integrity.

These results underline the sensitivity of breather dynamics in fully nonlinear systems, where even minor adjustments in nonlinearity parameters can significantly influence stability.

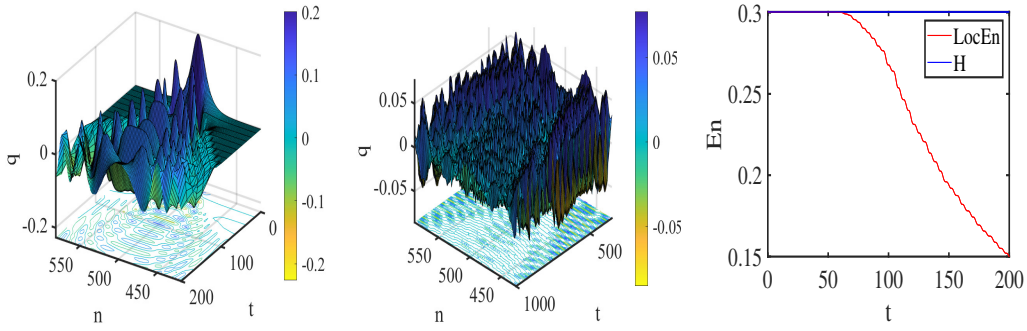

(a) (b) (c) Local and total Energy

Figure 2.5: Breather evolution for Optical Case IV with $k = 0$, $\rho = 1/3$, $\mu = 3$, $N = 1000$, and $t_{\max} = 1000$.

Thus far, we have examined all four combinations of nonlinear coefficients (a, α) under stationary optical modes with $k = 0$. For each case, we varied the mass ratio μ and the linear coupling strength ρ, revealing a rich diversity of

breather behaviours from long-lived to rapidly-unstable regimes.

Next, we turn our attention to the case $k = \pi$, where adjacent lattice sites oscillate out of phase, introducing new dynamics and stability patterns in the breather solutions.

2.5 Optical modes for $k = \pi$

Continuing with optical modes, where the inner and outer masses oscillate out of phase ($\dot{Q}_n = C\dot{q}_n$, with $C < 0$), we now shift from the case $k = 0$ (in phase motion, $\dot{q}_{n+1} \approx \dot{q}_n$) to the case $k = \pi$, where adjacent nodes oscillate in opposite phase ($\dot{q}_{n+1} \approx -\dot{q}_n$). This phase inversion leads to distinct breather dynamics, which we explore across four nonlinear interaction cases.

2.5.1 Case I: even potentials $(a = 0 = \alpha)$

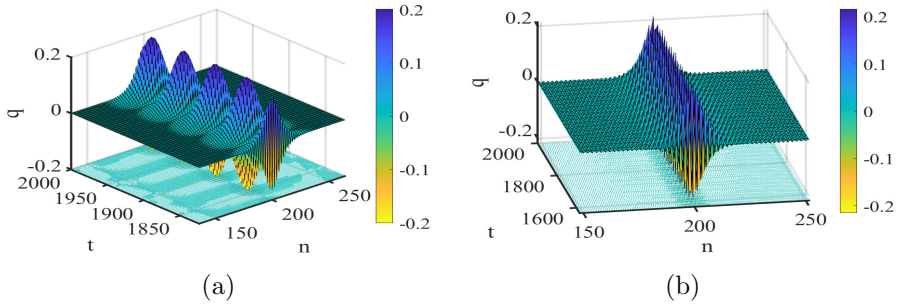

(a) (b)

Figure 2.6: Optical Case I for $k = \pi$, with $t_{\max} = 2000$ and $N = 400$, under the condition $a = \alpha = 0$. Left column: $\rho = \mu = 3$, $\beta = 1$, $b = 0.001$, $W_b = 16.0573$; right column: $\rho = \mu = 1/3$, $\beta = 1$, $b = 0$, $W_b = 12.8933$.

Simulations performed with $N = 400$ and over a time interval up to $t_{\max} = 2000$ indicate that the breather remains well localised and dynamically stable in both strong and weak coupling regimes, such as in the cases $(\rho = \mu = 3)$ and $(\rho = \mu = 1/3)$ shown in Figure 2.6. These results confirm the robustness of breather dynamics in systems governed by even potentials.

2.5.2 Case II: potentials with $(a = 0, \alpha \neq 0)$

Numerical simulations with $\alpha = 1$ indicate that breathers are long-lived under strong coupling ($\rho = 3$) with small mass ratio ($\mu = 1/3$), but unstable under other parameter combinations. Figure 2.7 shows how varying ρ and μ influences stability.

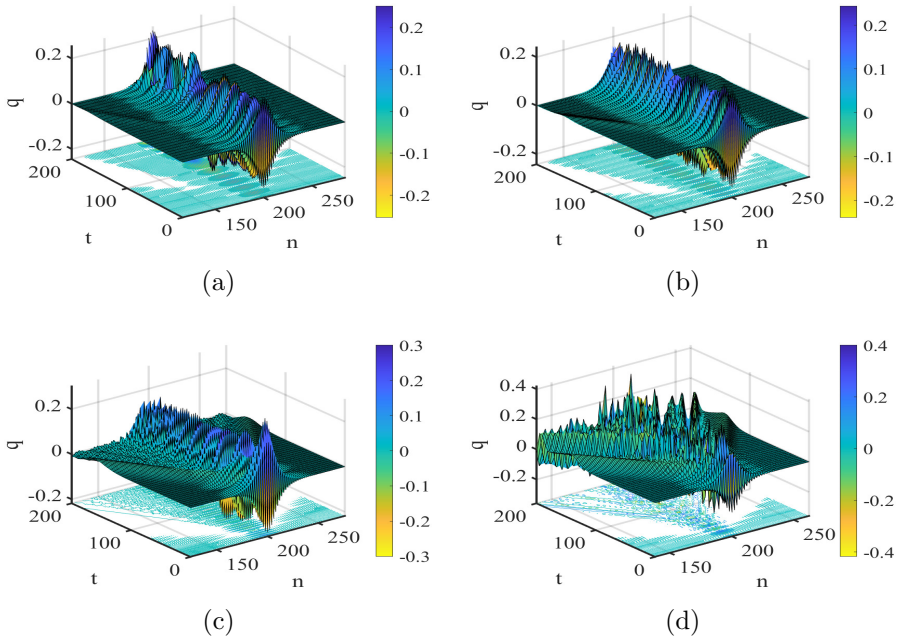

Figure 2.7: Optical Case II for $k = \pi$, $t_{\max} = 1000$, $N = 400$, $a = 0$, $\alpha = 1$. Top row: $\rho = 3$; bottom row: $\rho = 1/3$; left column: $\mu = 3$; right column: $\mu = 1/3$. The parameters used in this case are summarised Table A.2 in Appendix A.

2.5.3 Cases III & IV: potentials with $a \neq 0$

With $a = 1$ and $k = \pi$, simulations of the optical mode reveal the emergence of breather-kink and wobbling kink modes. These structures are generally unstable across all combinations of (ρ, μ), with one notable exception: when $\rho = 3$ and $\mu = 1/3$, a wobbling-kink mode develops that retains coherence over a longer duration and undergoes comparatively less amplitude reduction. In contrast, all other parameter settings result in rapid destabilisation and decay of the breather lattice structure. Figures 2.8 and 2.9 illustrate the corresponding time evolving profiles and energy decay.

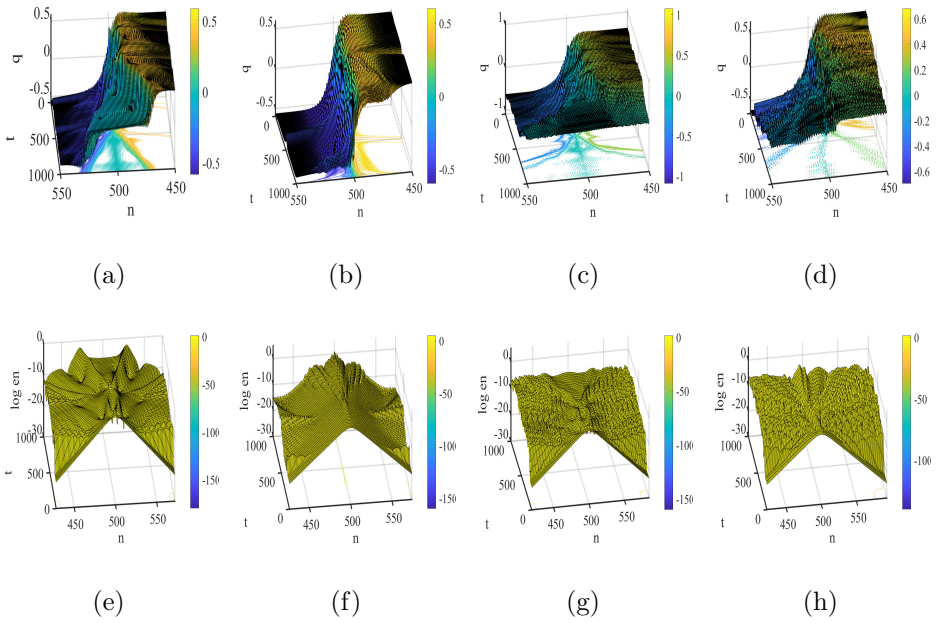

Figure 2.8: Breather-kink profiles (top) and energy evolution (bottom) for Optical case III with $a = 1$, $\alpha = 0$, $k = \pi$, $N = 1000$, $t_{\max} = 1000$. Parameters for this case are listed in Table A.2 in Appendix A.

These complex oscillations are referred to as *wobbling kinks*, which retain their kink-like structure. Thus, Figure 2.9(b) appears to exhibit a wobbling-kink type mode. In contrast, Figures 2.9(a) split in two kinks, (c), and (d) lose their kink structure. This behaviour, extensively studied in ϕ^4 models [5, 66, 67], reflects the dynamically rich and non-integrable nature of the MiM system. Our findings show that the presence of dual nonlinearities ($a \neq 0$, $\alpha \neq 0$) significantly amplifies instability in the system.

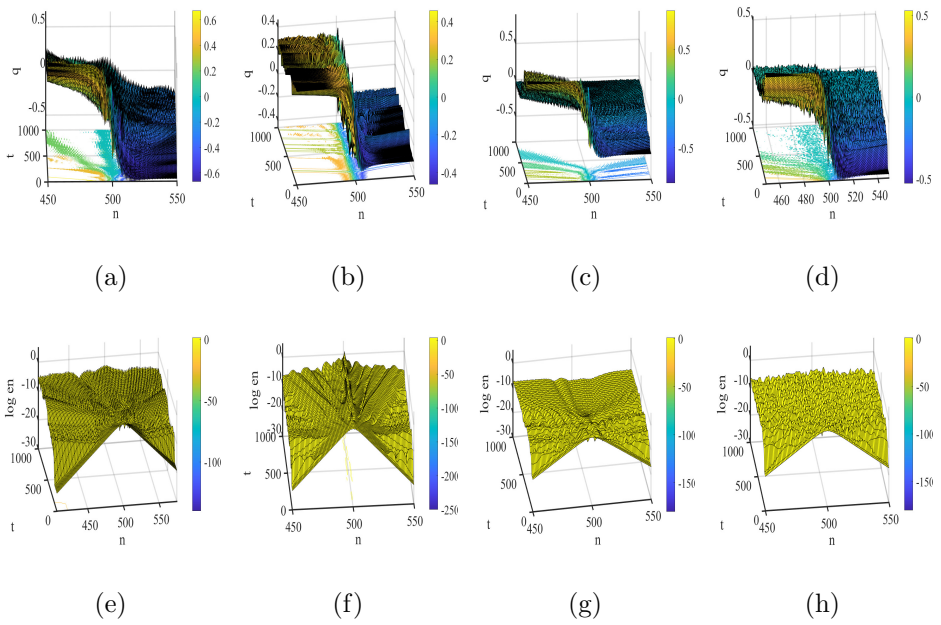

Figure 2.9: Profiles and energy decay for Optical Case IV with full nonlinearity ($a = \alpha = 1$), $k = \pi$, $t_{\max} = 1000$, $N = 1000$. Refer to Table A.2 in Appendix A for the parameters used in this case.

In this section, we have examined four principal nonlinear configurations for optical modes at $k = \pi$. The simulations demonstrate that, while both the even potential and the potential with $\alpha \neq 0$ at $\rho = 3$ and $\mu = 1/3$ yield stable breathers, the presence of dual nonlinearities gives rise to complex and unstable breather–kink dynamics.

We now proceed to investigate the acoustic modes for $k = \pi$, where energy transfer and stability profiles reveal additional nonlinear behaviours in MiM systems.

2.6 Acoustic modes for $k = \pi$

For acoustic modes, we present simulation results under both strong and weak linear interaction regimes ($\rho = 3, 1/3$) and for large and small mass ratios ($\mu = 3, 1/3$). The simulation parameters are configured as follows: lattice size $N = 400$ for Cases I and II, and $N = 1000$ for Cases III and IV, so the decay of the mode dose not interact with the body of the wave. The values of $\varepsilon = 0.1$,

along with appropriately chosen β and b, ensure the formation of breathers with reasonable spatial width, while satisfying the NLS focusing condition (2.2.14). In all cases, the breather or breather-kink is initially positioned at the centre of the lattice ($n = N/2$). Simulations are run up to $t_{\max} = 2000$ for Cases I and II, and $t_{\max} = 1000$ for Cases III and IV.

2.6.1 Case I: potentials with $a = 0 = \alpha$

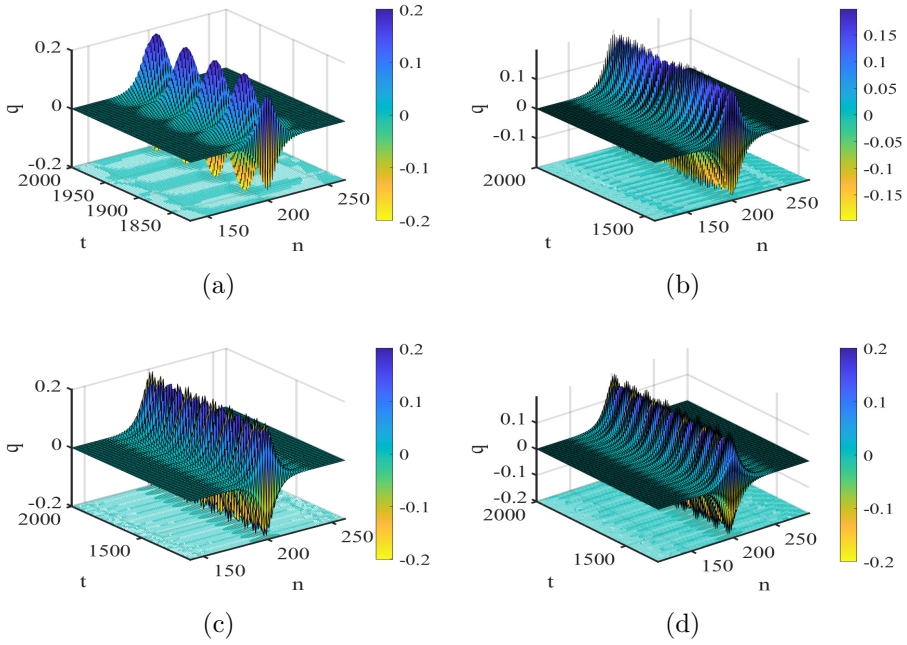

Figure 2.10: Plots of $q_n(t)$ against (n, t) for Acoustic Case I at $k = \pi$, taken in the late simulation $950 < t < 2000$, with $N = 400$. Top row $\rho = 3$, bottom row $\rho = 1/3$; left column $\mu = 3$, right column $\mu = 1/3$. Specific parameter sets of Case I are provided in Table A.3 in Appendix A.

Figure 2.10 presents the simulation results towards the end of the simulation period ($t_{\max} = 2000$). Across all combinations of ρ and μ, the wave profiles remain spatially localised and maintain a steady amplitude. This demonstrates that under even potential conditions ($a = \alpha = 0$), acoustic breather modes are dynamically stable for the full simulation duration, regardless of the interaction strength or mass ratio.

2.6.2 Case II: potentials with $(a = 0, \alpha \neq 0)$

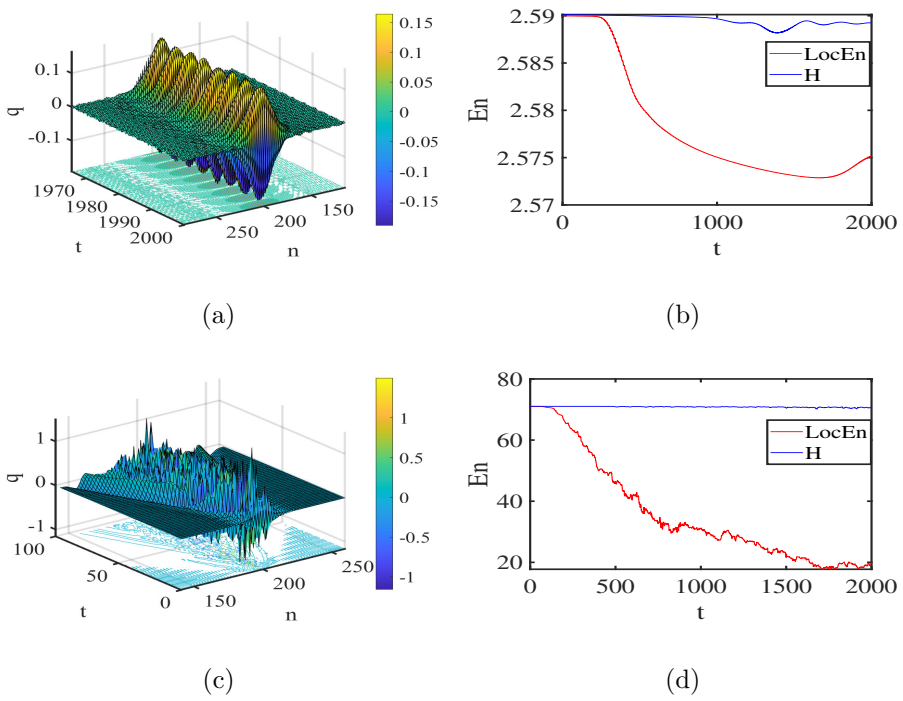

Figure 2.11: Plots of $q_n(t)$ against (n, t) for Acoustic Case II ($\alpha = 1$, $a = 0$) at $k = \pi$. Simulations are run with $\varepsilon = 0.1$, up to $t_{\max} = 2000$, with $N = 400$; only the range $100 \leq n \leq 300$ is shown. The parameter values for this case are provided in Table A.3 in Appendix A.

In this case, where $\alpha = 1$, acoustic breather modes display strong dependence on the strength of the linear interaction. Figure 2.11(a)–(b): The parameters are $\rho = \mu = 3$, with $\beta = b = 0.15$, yielding $W_b = 21$. Panel (a) shows the wave profile at late times; panel (b) shows the corresponding local and total energy, with only 0.58% loss in localised energy over 2000 time units.

For large coupling ($\rho = 3$), the breathers are long-lived and retain their structure over the entire simulation duration. This is evident in the upper panels of Figure 2.11, where the energy decay is minimally less than 1×10^{-5} per unit time. Similar stable behaviour is observed for $\rho = 3$, $\mu = 1/3$, as seen in Appendix A.3. In contrast, for weak coupling ($\rho = 1/3$), the breathers are highly unstable. Figure 2.11 (c)–(d): The parameters are $\rho = \mu = 1/3$, with $\beta = 2.82$, $b = 4.5$, $W_b = 14.89$. Panel (c) shows the early-time breather profile, which decays rapidly; panel (d) confirms this instability via a sharp

decline in local and total energy. As seen in the lower panels of Figure 2.11, the wave rapidly loses coherence, with its structure deteriorating within the first 100 time units. The accompanying energy plot shows a significant decline, confirming the short-lived nature of the breather under these conditions. Overall, the stability of acoustic breathers in the presence of ($\alpha = 1$) is strongly enhanced by stronger linear coupling and unstable under weak coupling.

2.6.3 Case III: potentials with $(a \neq 0, \alpha = 0)$

In this case, we investigate the dynamics when only the along-chain interactions are nonlinear, setting $a = 1$ and $\alpha = 0$, with $k = \pi$. The resulting wave solutions in $(q_n(t))$ exhibit a combination of breather and kink modes as presented in Figure 2.12.

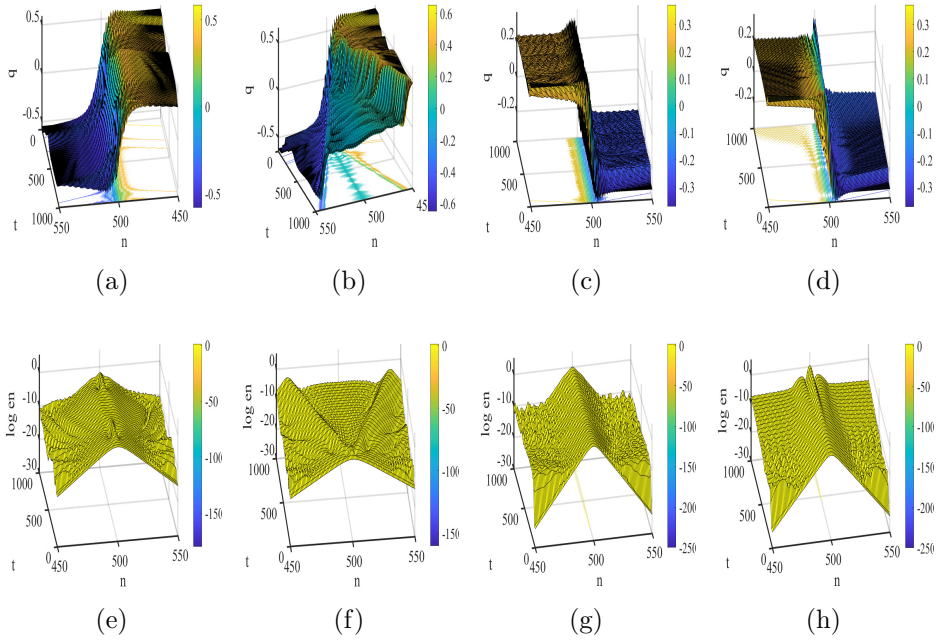

Figure 2.12: Wave profiles and energy evolution for Acoustic Case III at $k = \pi$, with $t_{\max} = 1000$, $N = 1000$, $a = 1$, $\alpha = 0$. The (a) $\rho = 3 = \mu$, (b)$\rho = 3, \mu = 1/3$, (c)$\rho = 1/3, \mu = 3$, and (d) $\rho = \mu = 1/3$. (a)-(d): Plots of $q_n(t)$ against (n, t); (e)-(h): Corresponding log energy plots. The relevant parameters for this case are listed in Table A.3 in Appendix A.

Across all parameter regimes, we observe initial transients characterised by small amplitude kinks. The simulations reveal that instability is more pronounced under strong coupling ($\rho = 3$). In contrast, for weak coupling ($\rho =$

1/3), the breather-kink may exhibit a wobbling behaviour involves a dynamic oscillation of the kink core, sustained over time before eventual decay and possible long-live as seen in Figure 2.12(h). This wobbling mode illustrates the interplay between localised breather dynamics and kink structure.

These findings highlight the emergence of complex breather–kink dynamics when only along-chain nonlinearity is present, with stability strongly influenced by the coupling strength. Further analysis of the combined nonlinear case ($a \neq 0$, $\alpha \neq 0$) is presented in the next section.

2.6.4 Case IV: the general case $(a \neq 0, \alpha \neq 0)$

We now consider the fully nonlinear scenario with $a \neq 0$ and $\alpha \neq 0$, focusing on the behaviour of breather-kink structures in the acoustic regime at $k = \pi$. Simulation results are summarised in Table A.3 for a total run time of $t_{\max} = 1000$. As shown in Figure 2.13, the system exhibits unstable behaviour under strong coupling ($\rho = 3$), while for weak coupling ($\rho = 1/3$) the dynamics become defocusing.

Figures 2.13(a)–2.13(b) display short-lived breather-kink modes for $\rho = 3$, $\mu = 1/3$. Initially, the structure retains coherence, but energy loss from the body of the wave becomes significant as time progresses. In Figures 2.13(c) and 2.13(d), we observe that instability begins to emerge around $t = 200$. By $t = 300$ in Figure 2.13(d) and $t = 500$ in Figure 2.13(c), the kink has extended and begins to separate into two distinct structures. This behaviour may be attributed to energy redistribution within the breather-kink mode. In the early stages, the breather and kink act as a single, coupled entity. However, as instability grows, internal energy shifts from the breather to the kink, leading to a breakdown of coherence and the eventual formation of two decoupled kink-like modes.

In this section, we examined acoustic breather and breather-kink dynamics under four distinct nonlinear configurations at $k = \pi$. For even potentials

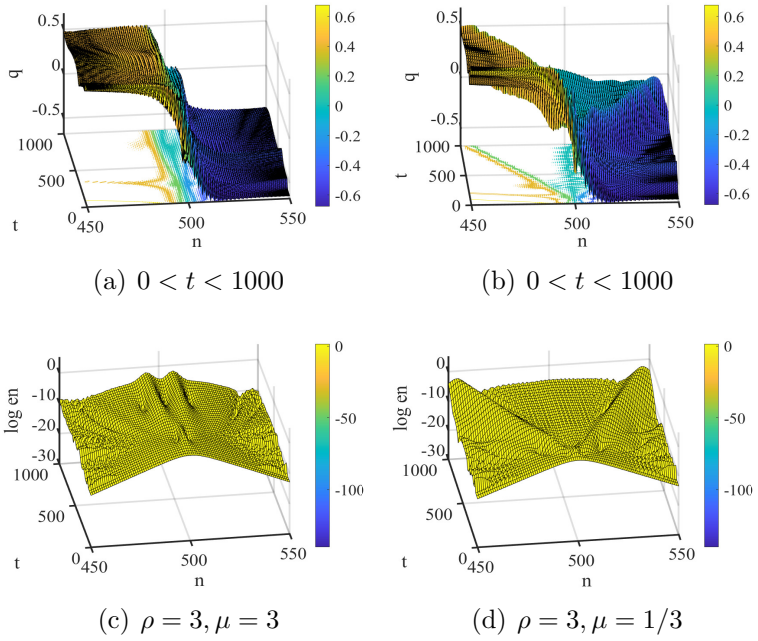

(a) $0 < t < 1000$ (b) $0 < t < 1000$

(c) $\rho = 3, \mu = 3$ (d) $\rho = 3, \mu = 1/3$

Figure 2.13: Breather-kink evolution for Acoustic Case IV at $k = \pi$, with $t_{\max} = 1000$, $N = 1000$, $a = 1$, $\alpha = 1$. (a)-(b): Profiles of $q_n(t)$ for $\rho = 3$, $\mu = 3$ (right) and $\mu = 1/3$ (left); (c)-(d): Corresponding local and total energy plots. Parameter values are given in Table A.3 in Appendix A.

$(a = 0 = \alpha)$, breathers remained well-localised and stable across all parameter regimes. When nonlinearity was applied only to the inner mass interaction $(a = 0, \alpha \neq 0)$, long-lived breathers were sustained under strong coupling, while weak coupling led to rapid decay. The introduction of a long-chain nonlinearity $(a \neq 0, \alpha = 0)$ produced breather-kink modes, with wobbling behaviour observed under weak coupling and instability under strong coupling. Finally, in the fully nonlinear case $(a \neq 0, \alpha \neq 0)$, instability dominated, culminating in energy redistribution and kink separation. These results highlight the sensitive dependence of breather stability on the nonlinear structure and interaction strength of the system.

We now turn our attention to the dynamics of moving modes.

2.7 Numerical results for moving modes

In the previous section, we focused on stationary wave configurations at $k = 0$ and $k = \pi$ for both optical and acoustic modes, where the breather

structures were centred and static within the lattice. Motivated by a desire to explore the effects of small deviations in the wave number, we now examine the dynamic response of the system under slight perturbations in k, specifically at $k = 0.1$ and $k = 3.1$, where we anticipate the formation of slow moving waves. This section is structured in two parts. The first case investigates acoustic travelling waves at $k = 0$, where a pure travelling wave is expected; that is, there is no breather component. The second part is divided into two subsections: one devoted to moving wave behaviour at $k = 0.1$; and the other at $k = 3.1$ in both these cases we expect breather or breather-kink modes. For each case, we examine the four standard interaction regimes Cases I to IV in order to assess whether the introduction of movement produces significant changes in wave stability, structure or localisation compared with the stationary configurations. We consider four combinations of the mass ratio μ and the linear interaction strength ρ.

To quantitatively evaluate wave propagation, we compare numerically computed wave speeds c_n with analytically derived asymptotic predictions c_a, as given by Wattis [1]. The relative error between the numerical and analytical speeds is defined as

$$\text{Relative Error} = \frac{|c_a - c_n|}{c_a}. \tag{2.7.1}$$

The asymptotic wave speed is given by

$$c(k) = \frac{\sin(k)}{m\omega\left(1 + \mu C^2\right)}, \tag{2.7.2}$$

where C is defined in equation (2.2.8).

In all simulations, the wave is initiated at position $n = N/4$, and the lattice size is fixed at $N = 1000$. Each simulation is run up to time units $t_{\max} = 1000$, with $\varepsilon = 0.01$, and parameters are selected to satisfy the NLS focusing criterion (2.2.15).

It is important to note that in Case IV, where both $a \neq 0$ and $\alpha \neq 0$, the system no longer permits a reduction to the NLS equation, as $\zeta \neq 0$. Instead, the dynamics are governed by a CGL system, introducing significantly more complex behaviours that lie beyond the scope of this thesis. Consequently, Case IV is excluded from the moving wave simulations.

In the following sections, we focus on Cases I, II, and III. We begin with the travelling wave solutions for $k = 0$, followed by a detailed analysis for $k = 0.1$ and $k = 3.1$.

2.8 Numerical simulations of travelling kinks

In this section, we numerically investigate the mobility of travelling waves in lattices governed by either a cubic ($b = 0, a \neq 0$) or quartic ($b \neq 0, a = 0$) NNI potential. These modes represent the limiting case as $k \to 0$ in the acoustic regime, where the kink–breather solution simplifies into a pure travelling kink wave without a breather component. The asymptotic form of these kink solutions, which is considerably simpler than that of breathers, is outlined in the appendix of Wattis [1].

2.8.1 Kinks in the cubic lattice ($a \neq 0, b = 0$)

We consider several configurations of mass ratio and linear interaction parameters, specifically $\rho, \mu \in \{3, 1/3\}$, along with fixed nonlinear parameters $a = 2$, $b = 0$, and $\alpha = \beta = 2$. Following the approach in Wattis [1], we adopt the approximate formula for slowly varying travelling kink solutions, which is derived under the assumptions of small lattice spacing h, and rescaled coordinate $z = h(n - ct) = \mathcal{O}(1)$. To leading order, the kink solution is given by

$$Q_n(t) = q_n(t) = \frac{3h}{a}\sqrt{2\gamma c_1}\tanh\left(z\sqrt{\frac{c_1}{\gamma}}\right), \quad z = h(n - ct), \tag{2.8.1}$$

were

$$\gamma = \frac{1}{12} + \frac{\mu^2}{\rho(1+\mu)^2}, \qquad c = c_0(1 + c_1 h^2), \qquad c_0 = \frac{1}{\sqrt{m(1+\mu)}} = \frac{1}{\sqrt{m+M}}. \tag{2.8.2}$$

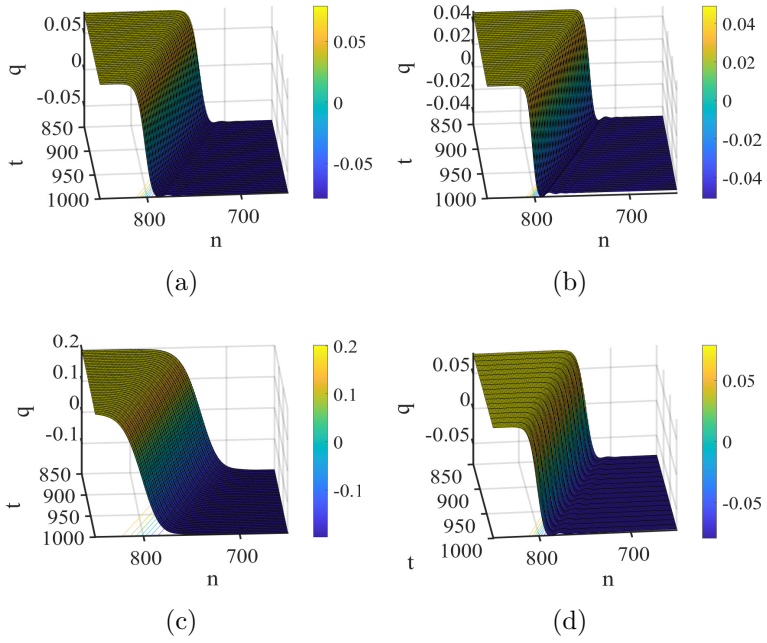

Figure 2.14: Evolution of a travelling kink in a lattice with cubic NNI potential from initial conditions (2.8.1).

Figure 2.14 illustrates the evolution of kink waves under both strong ($\rho = 3$, top row) and weak ($\rho = 1/3$, bottom row) linear coupling, with large ($\mu = 3$, right column) and small ($\mu = 1/3$, left column) mass ratios. We plot the displacements of the outer masses, $q_n(t)$, for $850 < t < 1000$ and $650 < n < 850$, using the parameter values: $a = 2$, $b = 0$, $N = 1200$, $\alpha = 2$, $\beta = 2$, $c_1 = 0.5$, $h = 0.1$. Top row: $\rho = 3$; bottom row: $\rho = 1/3$; left column: $\mu = 1/3$; right column: $\mu = 3$.

In each simulation, we initiated the kink at lattice site $n = N/4 = 300$. Over the duration $0 < t < 1000$, the kink propagates to approximately $n = 800$, yielding a numerically observed speed of $c \approx 0.5$. This result is in close agreement with the theoretical sound speed $c_0 = 0.5$, given by equation (2.8.2), using $m = 3, M = 1$ or $m = 1, M = 3$. Overall, the travelling kink solutions remain long-lived and structurally stable across all configurations considered.

2.8.2 Kinks in the quartic lattice ($a = 0$, $b \neq 0$)

In this subsection, we present the results from simulations of travelling kinks in a quartic lattice. We consider a purely quartic interaction scenario with $a = 0$ and $b = \alpha = \beta = 2$, and investigate both strong ($\rho = 3$) and weak ($\rho = 1/3$) linear coupling regimes, along with varying mass ratios ($\mu = 3$ and $\mu = 1/3$). According to Wattis [1], the leading order asymptotic approximation for kinks in a lattice with quartic NNI is given by

$$Q_n(t) = q(z) = \pm\sqrt{\frac{2\gamma}{b}}\tan^{-1}\left(\sinh\left(z\sqrt{\frac{2c_1}{\gamma}}\right)\right),\ z = h(n - ct), \quad (2.8.3)$$

where γ, c are defined in equation (2.8.2), $Q_n(t) = q_n(t)$, and c_1 arbitrary. Following the simulations, we observed that the initial kink often bifurcates into two distinct waves propagating in opposite directions through the lattice. Figures 2.15 and 2.16 illustrate the kink dynamics for the full range of tested parameter regimes: $\rho = 3, 1/3$ and $\mu = 3, 1/3$. The Figures 2.15 and 2.16 correspond to the parameter values: $a = 0$, $b = 2$, $N = 1200$, $\alpha = 2$, $\beta = 2$, $h = 0.1$, $t_{\max} = 1000$. In panels (a)–(d), a splitting into two kinks is visible at $0 < t < 100$, with approximate speeds: Panel (a) $c_{a11} = 0.46$, $c_{a12} = -0.36$; Panel (b) $c_{b11} = -0.5$, $c_{b12} = 0.5$. Panel (c) shows minimal splitting.

The kinks propagate at a speed similar to that observed in the cubic lattice case, though the quartic kinks exhibit slightly higher amplitude profiles.

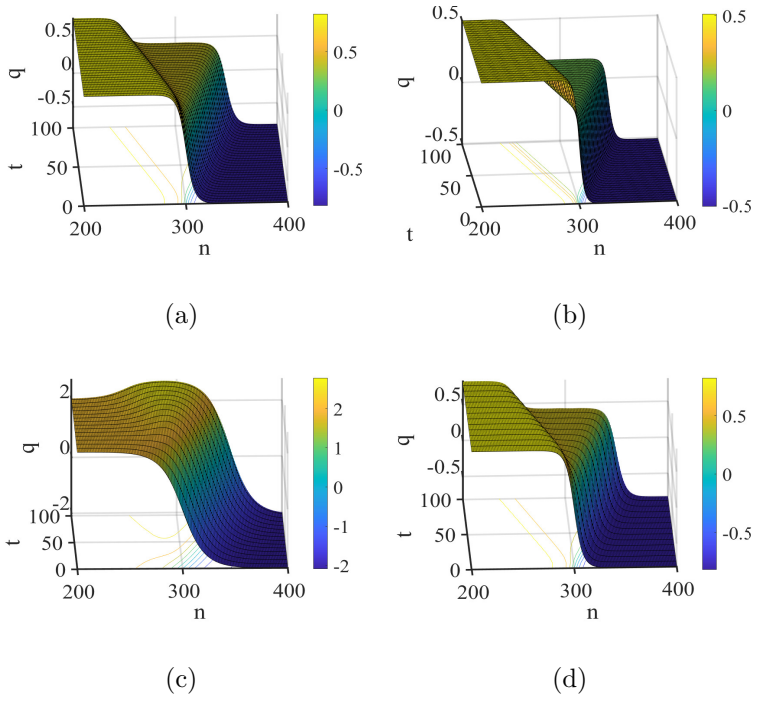

Figure 2.15: Propagation of kink waves in a lattice with quartic NNI potential. Displacements of the outer masses $q_n(t)$ are shown at early times ($200 < t < 400$) within the window $0 < n < 400$. Top row: $\rho = 3$; bottom: $\rho = 1/3$; left column: $\mu = 1/3$; right column: $\mu = 3$.

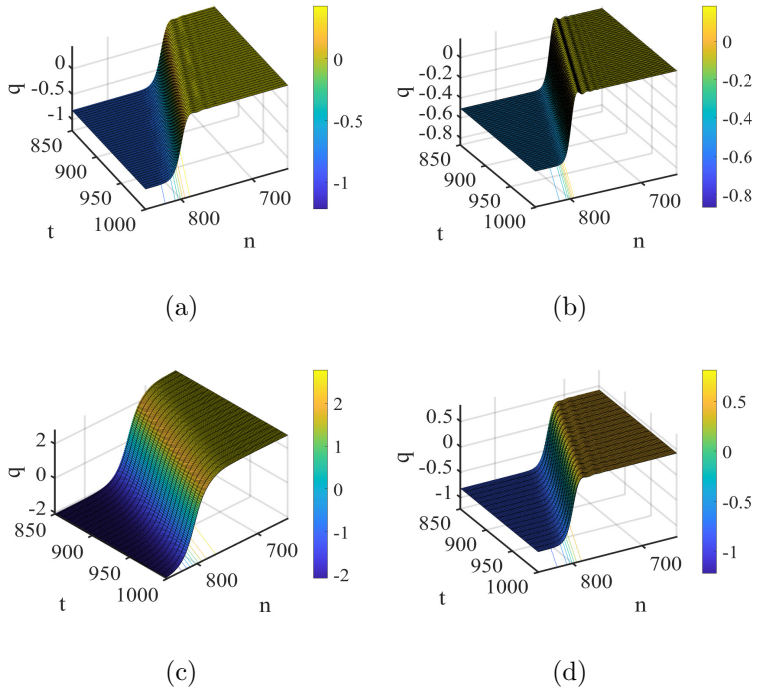

Figure 2.16: Later-time evolution of kink waves ($850 < t < 1000$) in a quartic lattice. Displacements $q_n(t)$ are shown with the same parameter values as in Figure 2.15. Top row: $\rho = 3$; bottom: $\rho = 1/3$; left column: $\mu = 1/3$; right column: $\mu = 3$.

In this study of quartic lattice kink dynamics, we observed interesting behaviour associated with strong linear coupling. Initially, as shown in Figure 2.15, the kink is localised around $n = 300$. By the middle of the simulation ($200 < t < 400$), the kink begins propagating, reaching approximately $n = 800$ by the end of the simulation ($850 < t < 1000$), as shown in Figure 2.16. The propagation speed was measured to be $c \approx 0.5$ in most configurations, aligning well with the asymptotic sound speed given in equation (2.8.2). One exception is the case $\rho = 1/3$, $\mu = 3$, where a slightly higher speed of $c \approx 0.55$ was observed (see Figure 2.16(c)).

During the early stages shown in Figure 2.15, the original kink was found to bifurcate into two distinct wave forms. These kinks then propagated in opposite directions: the larger amplitude component continued towards higher n values with positive speed, while the smaller amplitude component moved in the opposite direction with speed approximately $c \approx -0.5$. This behaviour highlights the capacity of quartic lattices to support kinks across a range of amplitudes and under varying values of interaction parameters.

2.9 Optical breather at $k = 0.1$

In this section, we investigate moving breather solutions for the optical case at wave number $k = 0.1$, where wave propagation is expected to be slow. We select appropriate parameter values for b and β to ensure a reasonable breather width, as summarised in Table A.6. The analysis is structured according to the four standard cases, beginning with Case I: even potentials ($a = 0 = \alpha$). The asymptotic wave speeds, derived from equation (2.2.8), for each panel in Table A.6 are:

$$\text{(a) } c_a = 0.037, \quad \text{(b) } c_a = 0.0041, \quad \text{(c) } c_a = 0.1126, \quad \text{(d) } c_a = 0.0126. \tag{2.9.1}$$

2.9.1 Case I: even potentials $(a = 0 = \alpha)$

Figure 2.17 presents simulation results for Case I. Across all configurations, the breather waves appear long-lived but slightly unstable, exhibiting minor radiation. Particularly, the measured breather speeds remain consistent within each panel. The numerical speeds for panels (a)–(d) are $c_n = 0.037$, 0.0041, 0.113, and 0.013 respectively, with the first two matching the theoretical predictions exactly, and relative errors of 0.36% and 3.17% for panels (c) and (d) respectively.

These results confirm the reliability of the asymptotic theory and indicate that, even in weakly moving regimes, the breather maintains coherence over time.

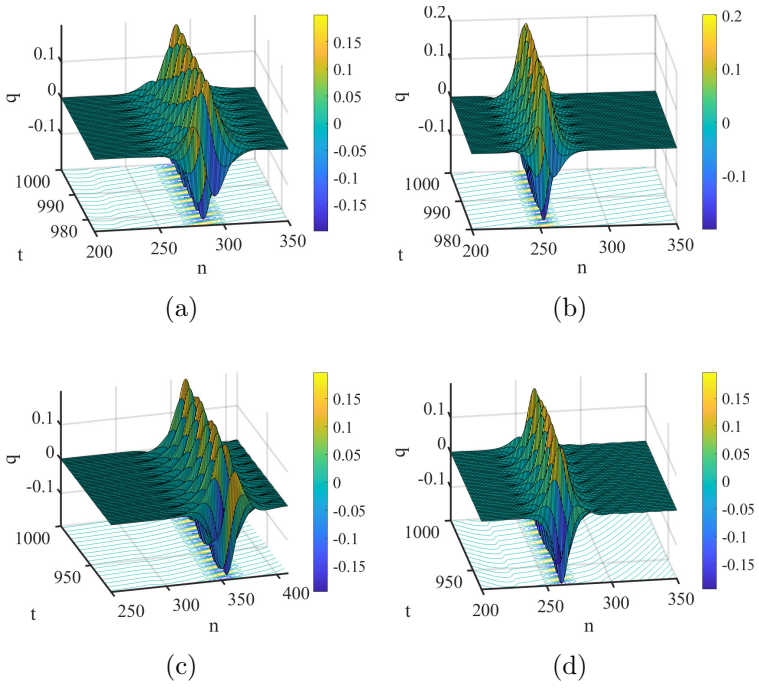

Figure 2.17: Optical Case I at $k = 0.1$, for $t_{\max} = 1000$, $N = 1000$. Top row: $\rho = 3$; bottom row: $\rho = 1/3$; left column: $\mu = 3$; right column: $\mu = 1/3$. Displayed region: $200 \leq n \leq 450$. Parameter values are given in Table A.6 in Appendix A.

In summary, breather modes for even potentials at $k = 0.1$ are characterised by slow movement, high persistence and marginal instability. The next subsection will explore the effect of introducing a non zero quadratic interaction potential $(\alpha \neq 0)$ in Case II.

2.9.2 Case II: potentials with $a = 0, \alpha \neq 0$

In this subsection, we present numerical simulations for the system with setting $\alpha = 1$ at $k = 0.1$. Appropriate values were chosen for the parameters b and β to ensure reasonable breather widths. The simulation results, shown in Figure 2.18, reveal that the breathers remain long-lived under strong coupling ($\rho = 3$), but become significantly unstable in cases with weak coupling ($\rho = 1/3$). In particular, the waveform increasingly distorts over time in the weaker interaction regimes.

The computed wave speeds for panels (a) and (b) are $c_n = 0.036$ and $c_n = 0.004$ respectively. When compared with the theoretical speeds from equation (2.9.1), these yield relative errors of 2.70% and 2.44% as defined in equation (2.7.1). For panels (c) and (d), reliable speed measurements are not feasible due to early waveform distortion, which makes precise tracking difficult.

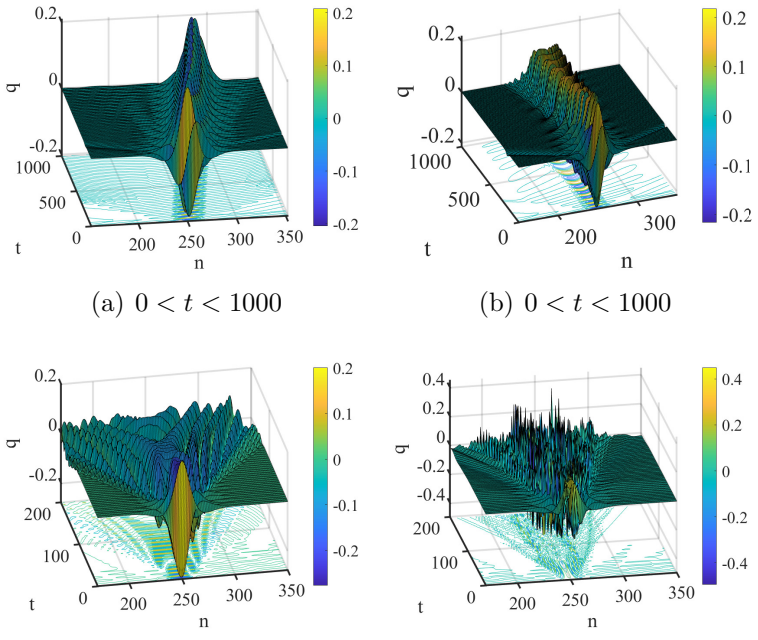

(a) $0 < t < 1000$ (b) $0 < t < 1000$

(c) $0 < t < 200$ (d) $0 < t < 200$

Figure 2.18: Optical Case II at $k = 0.1$, with $t_{\max} = 1000$, $N = 1000$, $a = 0$, $\alpha = 1$. Top row: $\rho = 3$; bottom row: $\rho = 1/3$; left column: $\mu = 3$; right column: $\mu = 1/3$. See Table A.6 in Appendix A for the corresponding parameter set.

Overall, in cases with $\alpha \neq 0$, the breather modes demonstrate significantly unstable behaviour under weak coupling ($\rho = 1/3$), whereas strong coupling

($\rho = 3$) maintains long-lived coherence. These findings highlight that even a slight deviation from $k = 0$ to $k = 0.1$ can drastically affect breather stability, with strong coupling yielding much more robust solutions. The next subsection explores the dynamics of moving breathers with ($a \neq 0$).

2.9.3 Case III: potentials with $a \neq 0, \alpha = 0$

In this subsection, we present numerical simulations for the case $a = 1$ and $k = 0.1$, representing a scenario where nonlinearity is applied along the chain, but not between the inner and outer masses. The results show that the breather maintains a long-lived, marginally unstable profile under movement. The transition from the stationary case at $k = 0$ to the slowly moving case at $k = 0.1$ does not significantly compromise the stability of the breather. The numerical speeds obtained for panels (a)–(d) are $c_n = 0.037$, 0.0040, 0.113, and 0.013, respectively, with corresponding relative errors of 0%, 2.44%, 0.36% and 3.17%. These speeds are in strong agreement with the theoretical predictions listed in equation (2.9.1), and are nearly identical to those observed for the even-potential case (Case I; see Subsection 2.9.1). This suggests that the along-chain nonlinearity ($a \neq 0$) does not disrupt breather coherence in the $k = 0.1$ regime.

In summary, for $a \neq 0$ and $k = 0.1$, the breather exhibits consistent, long-lived dynamic structure with only marginal instability across tested configurations. The comparison between numerical and asymptotic speeds confirms that the theoretical framework remains robust even when breather movement is introduced. Although motion at $k = 0.1$ slightly modifies the waveform, it does not compromise stability in otherwise stable regimes, and only slightly exacerbates instability in more sensitive cases.

In the following section, we investigate how similar movement influences the acoustic cases at $k = 0.1$.

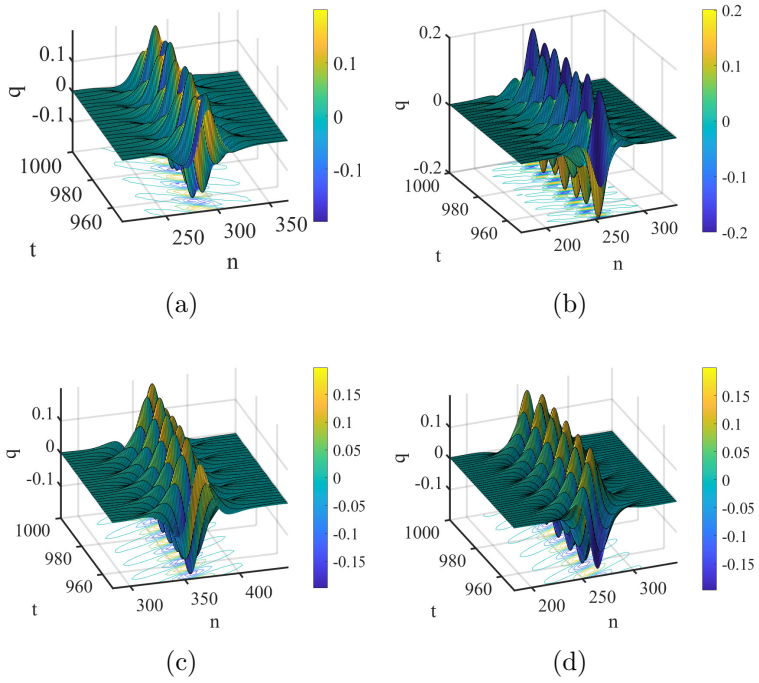

Figure 2.19: Optical Case III at $k = 0.1$, with $t_{\max} = 1000$, $N = 1000$, $a = 1$, $\alpha = 0$. Plots show late-time behaviour over $250 < n < 400$. Top row: $\rho = 3$; bottom row: $\rho = 1/3$; left column: $\mu = 3$; right column: $\mu = 1/3$. A summary of the parameter choices appears in Table A.6 in Appendix A.

2.10 Acoustic breather at $k = 0.1$

Following the optical cases, we now present results for acoustic wave dynamics at $k = 0.1$, as summarised in Table A.7. Since $k = 0.1$ is close to the stationary case $k = 0$, we might anticipate the emergence of kink-like structures, as previously observed in Section 2.8, or breather solutions, as seen in Sections 2.4.3 and 2.4.4. However, the simulations in Subsection 2.10.1 show that the breather–kink component may split into separate breather and kink structures as it propagates.

2.10.1 Case I and Case II: potentials with $a = 0$, $\alpha = 0$ and $\alpha \neq 0$

This subsection presents results for acoustic breathers with even potentials ($a = 0$) and both $\alpha = 0$ and $\alpha \neq 0$ at $k = 0.1$. For the case $\alpha = a =$

0, the waveforms exhibit significantly broader spatial widths than in other configurations. Despite their breadth, these breathers demonstrate unstable dynamics.

In Figure 2.20, the top row is $\rho = \mu = 1/3$. Early and later time panels show the transition from breather-kink to kink–anti kink dynamics, with parameters: $b = \beta = 10$, $W_b = 61$, $\omega = 0.0499$, and energy loss $\Delta E = 0.0095$. Bottom row is $\rho = 1/3$, $\mu = 3$, with $b = \beta = 10$, $W_b = 156.5307$, $\omega = 0.0496$, $c_n = 0.478$, $c_a = 0.48$ with error 0.41%, and $\Delta E = 2 \times 10^{-6}$.

As shown in Figure 2.20, panels from both the early and later stages of the simulation are presented for $\rho = 1/3$ with $\mu = 1/3$, or $\rho = 3$ with $\mu = 3$. In the case $\rho = \mu = 1/3$, a breather-kink splits into two modes: a kink–anti kink pair moving in opposite directions at speeds $c_n = 0.5$, as shown in Figure 2.20, panel (c). The corresponding theoretical value is $c_a = 0.497$, resulting in a small relative error of just 0.60%, confirming the accuracy of the asymptotic prediction.

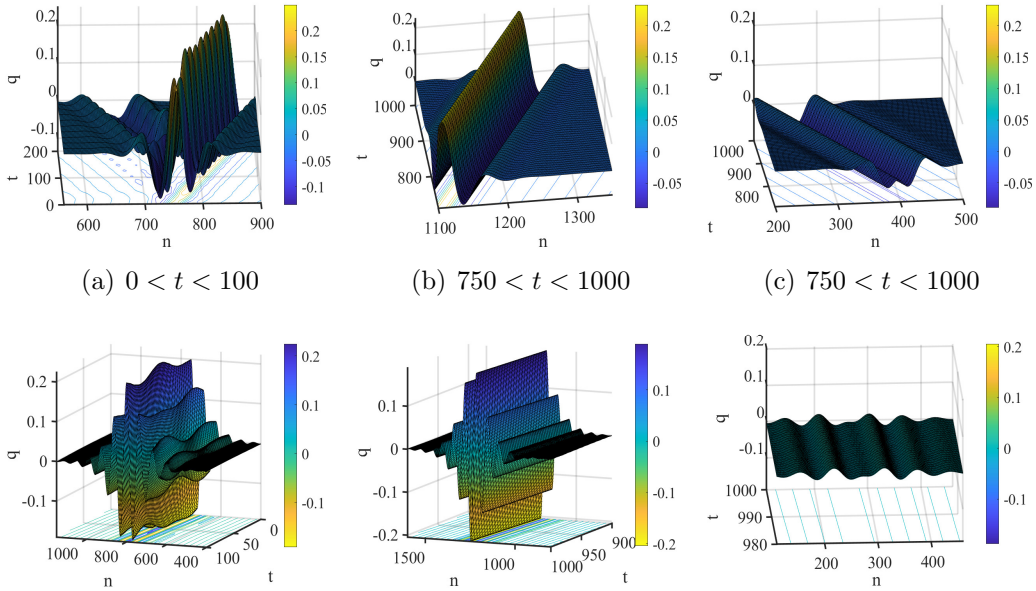

(a) $0 < t < 100$ (b) $750 < t < 1000$ (c) $750 < t < 1000$

(d) $0 < t < 200$ (e) $900 < t < 1000$ (f) $980 < t < 1000$

Figure 2.20: Acoustic Case I at $k = 0.1$, for $N = 3000$, $t_{\max} = 1000$.

When either ρ or μ is small, the system exhibits initial breather-kink behaviour that evolves over time into a broader breather, as seen in panels (d) and (e) of

Figure 2.20. A special delocalised mode is depicted in panel (f) of Figure 2.20. These modes are weakly unstable but persist over long durations.

2.10.2 Case III: potentials with $a \neq 0, \alpha = 0$

For the acoustic case with $a = 1$ and $\alpha = 0$, in the parameter range $(-10 \leq \beta, b \leq 10)$. We explored all configurations; the system consistently exhibited defocusing behaviour.

In summary, for acoustic waves at $k = 0.1$, breather-kink or kink–anti kink dynamics are observed when both ρ and μ are small or large. These solutions are marginally unstable. Similar behaviour is observed when $\alpha \neq 0$. Theoretical and numerical speeds agree closely. In contrast, systems with $a \neq 0$ consistently show defocusing behaviour, with no coherent localised structures observed.

2.11 Optical breather at $k = 3.1$

In Section 2.5, we analysed the stationary case at $k = \pi$, where the system exhibited distinct dynamical properties, as summarised in Table 2.1. In this section, we explore how a small deviation from the stationary case specifically, setting $k = 3.1$ affects breather dynamics. This allows us to assess the sensitivity of the system's behaviour to perturbations in wavenumber.

We begin by investigating Case I: even potentials. For each configuration, we compute the asymptotic breather speed using equation (2.2.8), and compare it with the numerically observed speeds. The asymptotic values for panels (a) to (d) are

$$(a)\ c_a = 0.0142, \quad (b)\ c_a = 0.0026, \quad (c)\ c_a = 0.0199, \quad (d)\ c_a = 0.0110. \tag{2.11.1}$$

2.11.1 Case I: even potentials ($a = 0 = \alpha$)

We now consider even potentials with $\alpha = a = 0$. The wave forms corresponding to all four parameter combinations are shown in Figure 2.21. In each case, the breather remains long-lived and exhibits only marginal instability.

To quantify the stability of these modes, we computed the energy difference between the localised and total energy. The results showed minimal energy loss over the course of the simulation $\Delta E \sim 3 \times 10^{-6}$ (a), $\Delta E \sim 6 \times 10^{-5}$ (b), $\Delta E \sim 1.7 \times 10^{-6}$ (c), and $\Delta E \sim 2 \times 10^{-6}$ (d), indicating strong localisation and excellent energy retention throughout the breather's evolution.

The numerically measured speeds for the same panels are (a) $c_n = 0.014$, (b) $c_n = 0.003$, (c) $c_n = 0.020$; and (d) $c_n = 0.011$. These values yield relative errors of (a) 1.41%, (b) 0.50%, (c) 4.52%; and (d) 0%, all of which show an agreement with the asymptotic predictions in equation (2.11.1).

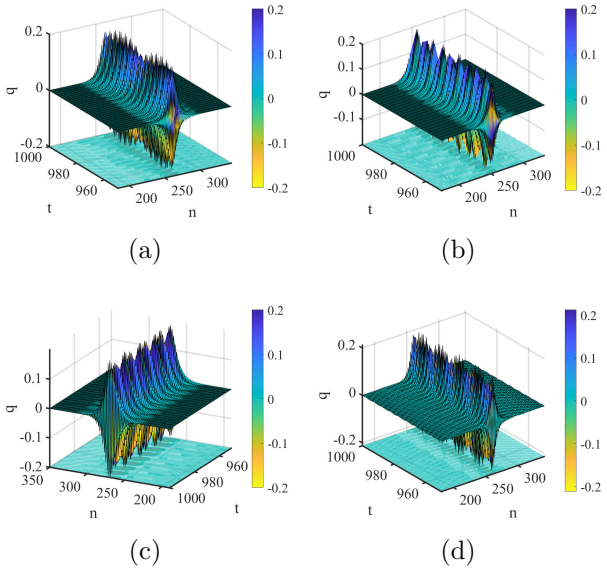

Figure 2.21: Optical Case I at $k = 3.1$, with $t_{\max} = 1000$, $N = 1000$, $a = \alpha = 0$. Top row: $\rho = 3$; bottom row: $\rho = 1/3$; left column: $\mu = 3$; right column: $\mu = 1/3$. All parameter settings applied in this case are detailed in Table A.4 in Appendix A.

In conclusion, while the stationary case at $k = \pi$ yields robust, localised solutions, a small deviation to $k = 3.1$ produces slowly moving, long-lived breathers with negligible energy loss. The close match between asymptotic and numerical speeds confirms the persistence of coherent structures under weak perturba-

tions in wave number.

2.11.2 Case II: Potentials with $a = 0, \alpha \neq 0$

We now present numerical simulations for the system with $k = 3.1$ and $\alpha = 1$, as illustrated in Figure 2.22. The breather behaviour strongly depends on the interaction strength ρ and mass ratio μ. For small ρ, the breathers are short-lived and unstable, whereas for large ρ when μ is small, the breather becomes more localised and longer-lived. These trends are confirmed in the energy plots of Figure 2.23, where the breather for small μ (panel b) remains confined with minimal energy dispersion.

Further insight is gained by comparing the numerical and theoretical wave speeds. However, in Figure 2.22 (a), (c), and (d), the breather decays significantly, resulting in distorted waveforms. As such, the measured wave speeds in these cases become meaningless, and any comparison with the theoretical predictions is unreliable. Only in Figure 2.22 (b) does the breather maintain coherence, allowing a meaningful comparison. Here, the numerically measured speed is $c_n = 0.0020$, with an associated energy difference of $\Delta E \sim 3 \times 10^{-6}$. When compared to the asymptotic prediction from equation (2.11.1), this corresponds to a relative error of approximately 23.08%, reflecting a reasonable agreement.

In conclusion, although breathers remain relatively long-lived at $k = 3.1$ under strong coupling their stability is significantly affected by the mass ratio. Small μ enhances localisation and energy retention, while large μ increases instability. The numerical speeds align poorly with asymptotic predictions in cases where energy dispersion dominates, especially for panels (a), (c) and (d). The next section investigates the role of a non-zero a.

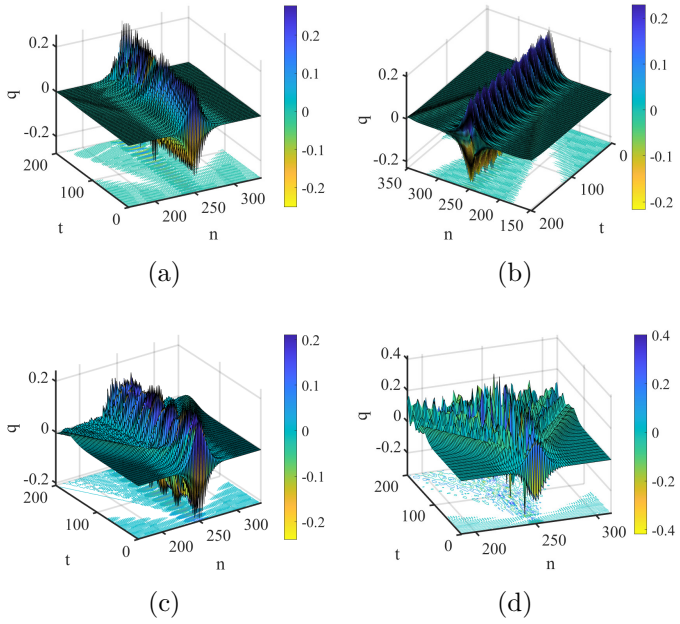

Figure 2.22: Optical Case II at $k = 3.1$, with $N = 1000$, $a = 0$, $\alpha = 1$. Top row: $\rho = 3$; bottom row: $\rho = 1/3$; left column: $\mu = 3$; right column: $\mu = 1/3$. Complete details of the simulation parameters can be found in Table A.4 in Appendix A.

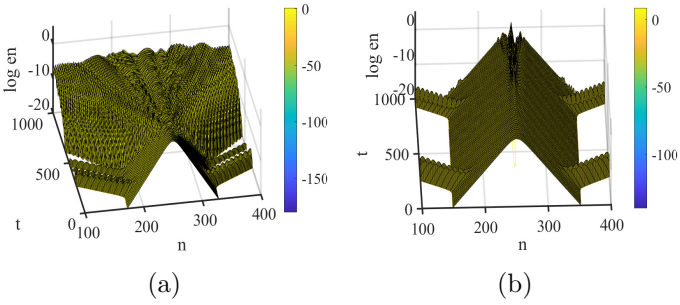

Figure 2.23: Energy plots for Optical Case II at $k = 3.1$, $N = t_{\max} = 1000$, corresponding to panels (a) and (b) in Figure 2.22. Shared parameters: $a = 0$, $\alpha = 1$.

2.11.3 Case III: potentials with $a \neq 0, \alpha = 0$

In this section, we present numerical results for breathing–kink modes with $a = 1$, $\alpha = 0$ and $k = 3.1$, as shown in Figure 2.24. The aim is to assess how a small shift from the stationary case at $k = \pi$ affects the dynamics, particularly regarding the persistence and stability of breather- kink structures.

The simulations reveal varying behaviours across configurations. In panel (b), corresponding to $\rho = 3, \mu = 1/3$, the breather-kink mode persists over time, demonstrating a long-lived but unstable structure. In contrast, panel (a) and

panel (d) show it splitting into two separate kinks, indicating significant different response. In panel (c), the breather- kink decays rapidly, providing evidence of strong instability under this configuration.

The numerically observed in cases (a), (c), and (d), the wave structure breaks down as the breather splits into multiple parts, making the notion of a numerically speed meaningless. Only in case (b) does the breather retain a coherent structure, allowing a meaningful and reasonably accurate comparison with the theoretical prediction in equation (2.11.1) as $c_n = 0.010$, error $= 29.58\%$.

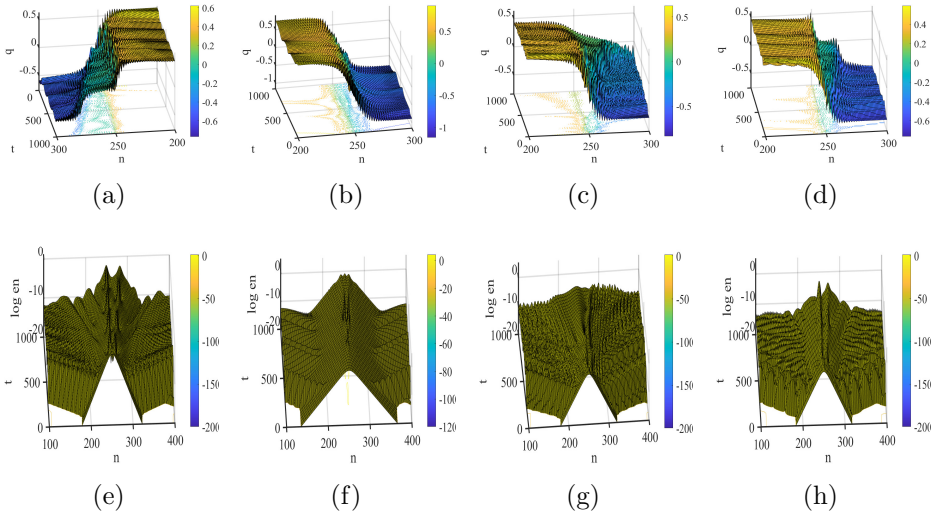

Figure 2.24: Evaluation of $q_n(t)$ and log energy plots for optical case III at $k = 3.1$, with $t_{\max} = 1000$, $N = 1000$, $a = 1$, $\alpha = 0$. The (a) $\rho = 3 = \mu$; (b) $\rho = 1/3, \mu = 3$; (c) $\rho = 1/3, \mu = 3$;(d) $\rho = \mu = 1/3$. All parameter settings applied are detailed in Table A.4 in Appendix A.

Log energy plots corresponding to Figure 2.24, as shown in panels (e) to (h), indicate that, in most configurations, the breather–kink structure eventually splits into two distinct modes. In particular, panel (g) exhibits rapid energy dispersal and significant waveform distortion, highlighting the strong instability present in this case.

The results demonstrate that even a small deviation from $k = \pi$ affects the breather-kink stability to a significantly extent. Configurations with large ρ and small μ produce longer-lived modes.

Having examined the optical breather dynamics at $k = 3.1$, we now turn our attention to the acoustic case. This section explores how small deviations

from the stationary state at $k = \pi$ influence the behaviour of acoustic breather modes under various nonlinear interaction regimes.

2.12 Acoustic Breather at $k = 3.1$

In this section, we extend our investigation to the acoustic regime at $k = 3.1$. Previously, we analysed the stationary case at $k = \pi$ (see Subsection 2.6), where the system exhibited stable dynamics in Case I, and long-lived behaviour for large ρ and weak instability for small ρ in Case II. Case III showed prominent instability, at $\rho = 3, \mu = 1/3$.

Here, we evaluate how introducing a small deviation in wave number, specifically $k = 3.1$, influences the acoustic breather dynamics. This approach allows us to explore how near-stationary movement affects breather localisation and energy propagation. To quantify these effects, we compute both asymptotic and numerically obtained wave speeds, enabling comparison of analytical predictions with simulated behaviour. The asymptotic speeds for panels (a)–(d) are

$$\begin{aligned} &(a):\ c_a = 0.00381, \quad (b):\ c_a = 0.00867, \\ &(c):\ c_a = 0.00027, \quad (d):\ c_a = 0.00070 \end{aligned} \tag{2.12.1}$$

2.12.1 Case I: even potentials $(a = 0 = \alpha)$

We first consider the case of even potentials, with $\alpha = a = 0$. As shown in Figure 2.25, the acoustic breather remains long-lived across all tested configurations of ρ and μ. These results closely resemble the behaviour observed in the optical counterpart at the same wave number (see Subsection 2.11.1).

The numerical simulations yield the following wave speeds and energy variations: (a) $c_n = 0.004$, $\Delta E \sim 1.5 \times 10^{-6}$; (b) $c_n = 0.009$, $\Delta E \sim 7 \times 10^{-7}$; (c) $c_n = 0$, $\Delta E \sim 4 \times 10^{-8}$; and (d) $c_n = 0.0010$, $\Delta E \sim 2 \times 10^{-6}$ faster than expected.

The relative error between the analytical and numerical speeds, calculated using equation (2.12.1), is given by: (a) 5.07%; (b) 3.75%; (c) 100%; and (d) 43.53%.

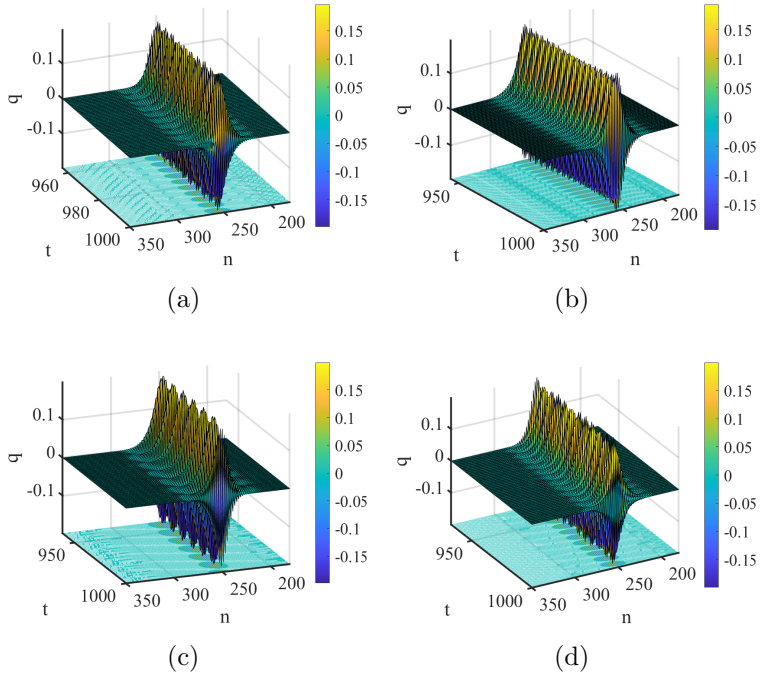

Figure 2.25: Acoustic Case I at $k = 3.1$, simulated for $t_{\max} = 1000$ with $N = 1000$, $a = 0$, $\alpha = 0$. Top row: $\rho = 3$; bottom row: $\rho = 1/3$; left column: $\mu = 3$; right column: $\mu = 1/3$. A summary of the parameter choices appears in Table A.5 in Appendix A.

The results for Case I at $k = 3.1$ show that breather modes remain long-lived, regardless of the interaction strength.While the energy loss is minimal, the numerical speeds c_n deviate from the asymptotic predictions c_a. The agreement is significantly less accurate for $\rho = 1/3$, but remains reasonable for $\rho = 3$. This discrepancy may be due to the sensitivity of the system for a small deviation in wave number. In the following subsection, we investigate the influence of non-zero α.

2.12.2 Case II: potentials with $a = 0, \alpha \neq 0$

We now consider the acoustic breather modes at $k = 3.1$ in the presence of nonlinear coupling, with $\alpha = 1$ and $a = 0$. Figure 2.26 illustrates the behaviour of the breather across two configurations with strong linear interaction ($\rho = 3$),

for both large and small mass ratios. In both cases, the breather remains long-lived but exhibits weak instability. The numerically observed wave speeds are (a) $c_n = 0.004$ and (b) $c_n = 0.009$.

These values are consistent with those found in Case I (see Subsection 2.12.1). The corresponding relative errors, computed using the asymptotic predictions in Equation (2.12.1), are 5.07% and 3.75% respectively.

For weak linear interactions ($\rho = 1/3$), we were unable to satisfy the NLS focusing condition (2.2.15) within the range $-10 \leq b, \beta \leq 10$. As a result, no breather modes could be identified in these parameter regimes, as the system exhibited defocusing behaviour.

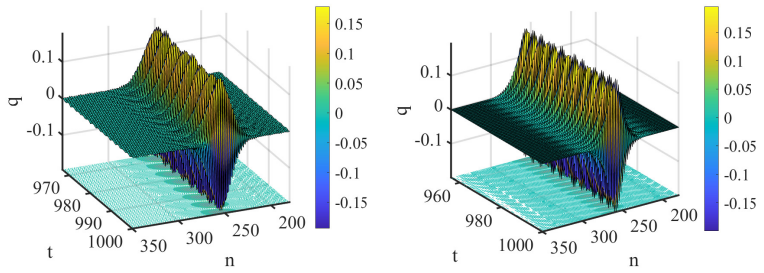

(a) (b)

Figure 2.26: Acoustic Case II at $k = 3.1$, with $t_{\max} = 1000$, $N = 1000$, $a = 0$, $\alpha = 1$. This figure at $\rho = 3$ corresponds to the setup described in Table A.5 in Appendix A. Configurations with $\rho = 1/3$ were found to be defocusing.

These results indicate that in the acoustic regime at $k = 3.1$, a non-zero α leads to weakly unstable, but long-lived breather dynamics under strong coupling. In contrast, weak coupling ($\rho = 1/3$) prevents the formation of localised breathers, underscoring the importance of interaction strength in maintaining wave coherence. The following subsection investigates the effect of a non-zero a.

2.12.3 Case III: potentials with $a \neq 0, \alpha = 0$

This subsection presents the acoustic case at $k = 3.1$ for $a = 1$, illustrated in Figure 2.27. Under strong linear interactions ($\rho = 3$), the system exhibits breather-kink dynamics that vary significantly with the mass ratio μ. For large

μ, the kink mode is long-lived but weakly unstable. In contrast, for small μ, the mode becomes highly unstable and splits into two components. This behaviour contrasts with the optical regime discussed in Subsection 2.11.3, where the dynamics were more stable for small mass ratios.

A notable case arises for $\mu = 1/3$, as shown in Figure 2.27(b), where the kink amplitude diminishes and subsequently divides into two distinct kink structures. Conversely, for $\mu = 3$ (Figure 2.27(a)), the breather-kink maintains its form but exhibits reduced amplitude and gradual dispersion.

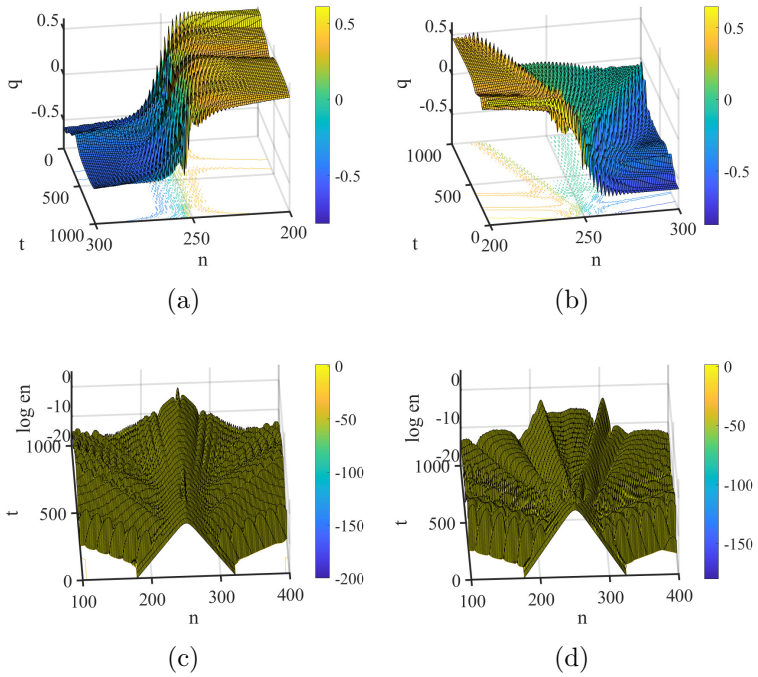

Figure 2.27: Acoustic Case III at $k = 3.1$, with $t_{\max} = 1000$, $N = 1000$, $a = 1$, $\alpha = 0$. Bottom panels show corresponding log energy plots. The relevant parameters for this case at $\rho = 3$ are listed in Table A.5 in Appendix A. Configurations with $\rho = 1/3$ are defocusing. Only $100 \leq n \leq 400$ is displayed.

The log energy plots in Figures 2.27(c)–2.27(d) confirm significant energy dispersal, especially for small μ. In panel (a), the breather-kink shows mild energy loss, with $\Delta E \sim 8.1 \times 10^{-6}$ whereas in panel (b), stronger energy dispersion occurs, with $\Delta E \sim 7.4 \times 10^{-4}$.

The comparison between the numerical and asymptotic wave speeds is ultimately meaningless in this context. In panel (a), the wave remains stationary at $n = 250$ throughout the simulation, indicating no actual propagation. In

panel (b), the initial wave splits into two distinct components, further complicating the interpretation due to the lack of coherent wave motion.

In summary, the results reveal that the breather-kink structure at $k = 3.1$ is highly sensitive to the mass ratio μ. For smaller values of μ, the mode becomes unstable and splits; while, for larger values, it remains coherent, but loses amplitude. These findings contrast with those of the optical case and emphasise the impact of acoustic dynamics on breather-kink behaviour under nonlinear interactions.

2.13 Discussion

This chapter presented a numerical investigation into the robustness and dynamics of the MiM FPUT lattice. Initial conditions were derived from asymptotic reductions to the NLS equation, as described in [1]. The lattice was shown to support localised modes when the focusing condition $\eta(k)D_3(k) > 0$ is met, imposing constraints on the wave number k; the nonlinear parameters a, b, α, β; the mass ratio μ; and the linear interaction strength ρ.

We analysed both stationary and moving cases for a range of interaction settings labelled as Cases I to IV under four primary configurations: (a) $\rho = 3, \mu = 3$; (b) $\rho = 3, \mu = 1/3$; (c) $\rho = 1/3, \mu = 3$; and (d) $\rho = 1/3, \mu = 1/3$. To satisfy the focusing condition, we selected parameter values within the range $-10 < b, \beta < 10$. Our simulations included both stationary modes ($k = 0, \pi$) and slow moving cases ($k = 0.1, 3.1$), across optical and acoustic regimes. In addition, we examined travelling kink solutions in the cubic and quartic lattice configurations, using the approximate solutions (2.8.1) and (2.8.3). These results reveal a nuanced relationship between system parameters and the emergence, persistence and decay of localised modes.

While analytical results exist for stationary breather solutions [68, 69], there are no general results for moving breathers in such discrete systems. Our numerical simulations demonstrate how stability is maintained or lost under

perturbations in both wave number and system parameters.

Across many simulations, the observed numerical speeds c_n closely matched the asymptotic predictions c_a, notably in Subsections 2.9.1, 2.9.2 and 2.11.1. This agreement indicates that the speed is primarily governed by ρ, μ, m, M and $\omega(k)$, with minimal influence from nonlinear coefficients a, b, α, β. However, other cases, particularly those presented in Subsections 2.11.2, 2.11.3, and 2.12.3, are also rendered meaningless due to the lack of coherent motion.

In stationary simulations ($k = 0$ and $k = \pi$), Case I ($a = \alpha = 0$) demonstrated persistent, stable behaviour for both optical and acoustic regimes. Introducing non-zero α destabilised the breather at small ρ, particularly in the acoustic case. The mass ratio μ emerged as a key factor at $k = \pi$: lower μ values found long-lived modes, even under strong nonlinearity.
For Case III ($a \neq 0, \alpha = 0$), we observed breather-kink structures. These remained intact when ρ was large (optical) or small (acoustic), but otherwise split into two propagating kinks. This behaviour, detailed in Subsections 2.6.3 and 2.6.4, is consistent with energy redistribution, damping and loss of coherence. Our findings indicate that small μ and large ρ resulting in wobbling-kink behaviour aligns with the work by Wattis [1].

Moving wave simulations ($k = 0.1, 3.1$) showed slower evolution compared to stationary modes. In Cases I and II, long-lived solutions persisted for large μ. Case III yielded more distinctive dynamics: for $k = 3.1$ in the optical regime, kinks remained long-lived only when ρ was large and μ was small. Conversely, in the acoustic case, large μ improved stability. These trends echo the findings of Wallen *et al.* [48], Kevrekidis *et al.* [44, 45], and Liu *et al.* [46], which underscore the mass ratio's critical influence on breather stability.

In the acoustic regime at $k = 0.1$, Case III exhibited defocusing behaviour, preventing the formation of stable breathers. Additionally, travelling kinks in

the quartic NNI case at $k = 0$ were observed to split into two distinct structures during propagation. Case IV across several simulations was not analysed further due to the emergence of CGL dynamics, making direct comparisons inappropriate.

At $k = 0.1$, breather-kink modes in Case III frequently split into separate breather and kink–antikink structures. This behaviour reported by Alonso-Izquierdo *et al.* [70], who examined resonant energy transfer in kink dynamics within scalar field models. Although their context differs, a continuous system with multiple shape modes, the underlying mechanism of energy redistribution is likely comparable. Similar interpretations arise in the works of Cadet [36, 37] and Theocharis *et al.* [51], who reported energy bifurcation and asymmetric breather behaviour in heterogeneous nonlinear lattices.

The stationary regime at $k = 0$ showed stability for all ρ, while the introduction of non-zero α caused decay for small ρ. At $k = 0.1$, splitting dynamics emerged. For $k = \pi$, low μ supported stability at large ρ, whereas at $k = 3.1$, long-lived behaviour required large μ in the acoustic regime and small μ in the optical case. The deviation from the stationary state ($k = 0, \pi$) to moving regimes ($k = 0.1, 3.1$) consistently demonstrated heightened sensitivity to μ, ρ and weak nonlinear interactions.

In this chapter, we have numerically simulated the dynamics of MiM FPUT chains. The insights gained highlight the intricate relationship between mass ratio, coupling strength, and nonlinearity in shaping the localised solutions. In Chapter 2, we turn to the analytical investigation of breather propagation in mechanical triangular lattices, extending our exploration to more complex geometries.

Chapter 3

Breather modes in mechanical triangular lattice

This chapter presents a 2D mechanical triangular lattice in which each node is connected to six nearest neighbours, forming a symmetric hexagonal arrangement. The model incorporates linear NNI and a nonlinear onsite potential at each node. Two types of mode: optical and acoustic are identified from the dispersion relation, each supporting distinct propagation characteristics. Using asymptotic techniques, we derive small amplitude breather solutions, leading to a NLS equation. The existence of these breathers requires the satisfaction of ellipticity and focusing conditions, which are analysed in detail. Part of this chapter are being prepared for publication.

3.1 Introduction

In this chapter, we investigate the existence and properties of discrete stationary breather modes in a 2D mechanical triangular KG lattice. Each node connects to six nearest neighbours, resulting in a triangular configuration. The primary objective is to establish the dynamic behaviour of these localised modes through analytical methods. To achieve this, we apply multiple scale techniques to systematically derive the conditions under which discrete

breathers emerge. It is important to acknowledge certain modelling simplifications adopted in this study. Specifically, we assume only linear NNIs and simplify the onsite potential. These assumptions facilitate the tractability of the analysis without significantly altering the core dynamic insights.

The chapter is structured as follows. Section 3.2 derives the fundamental equations of motion for the triangular lattice. In Section 3.3, we perform a multiple scale expansion of the equations. Section 3.3.5 simplifies the expanded system to a (2+1)-dimensional NLS equation. To support the existence of localised breather solutions, we introduce the focusing condition and the ellipticity criterion [15]. Finally, in Section 3.4, we further simplify the model enabling explicit determination of stationary breather solutions.

3.2 Derivation of model equations

In this section, we analyse a symmetric triangular lattice of particles connected as illustrated in Figure 3.1. We define the orthonormal basis vectors $\mathbf{B} = \{\mathbf{i}, \mathbf{j}\}$, where $\mathbf{i} = [1, 0]^T$ and $\mathbf{j} = [0, 1]^T$. The position of the (m, n)-th node in the triangular lattice is $\mathbf{r}_{m,n} = m\mathbf{i} + n\sqrt{3}\,\mathbf{j}$, which ensures the regularity of the triangular structure. Each particle is connected to its six nearest neighbours, and the position of each node is allowed to vary within the plane of the lattice through perturbations denoted by $(u_{m,n}(t), v_{m,n}(t))$. Consequently, we have a fully 2D Hamiltonian $H(u_{m,n}, v_{m,n})$, neglecting nonlinear NNI.

3.2.1 Horizontal spring extension and potential energy

In order to derive the equations of motion for the lattice, we first calculate the horizontal distance between neighbouring nodes. Consider two adjacent nodes located at (m, n) and $(m + 2, n)$ in the triangular lattice. Their displacements are given by $(u_{m,n}, v_{m,n})$ and $(u_{m+2,n}, v_{m+2,n})$, respectively. The rest length between these nodes is denoted by h. The relative displacements are $\Delta u = u_{m+2,n} - u_{m,n}, \Delta v = v_{m+2,n} - v_{m,n}$. The deformed relative vector is $\Delta\mathbf{r} =$

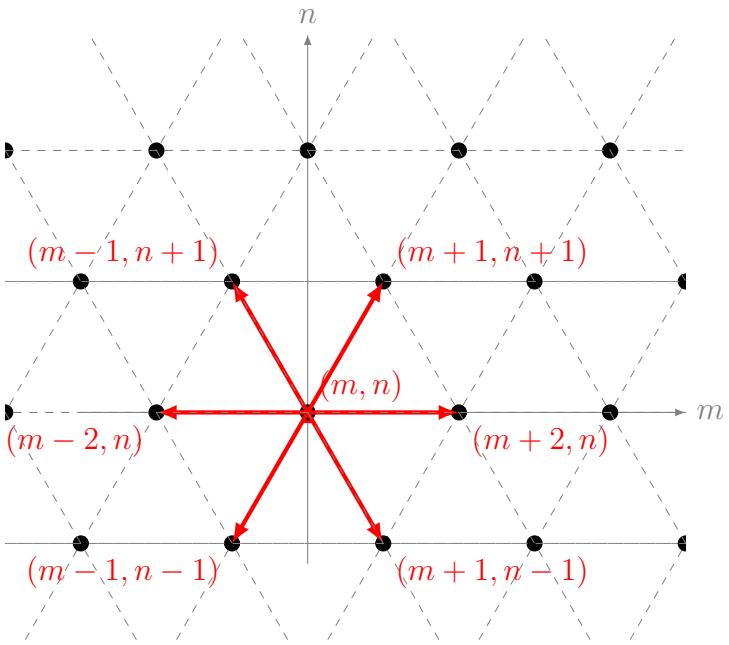

Figure 3.1: A mechanical triangular lattice.

$(h + \Delta u, \Delta v)$. Thus, the actual distance between the nodes becomes

$$d = \sqrt{(h + \Delta u)^2 + (\Delta v)^2} \tag{3.2.1}$$

$$= h\sqrt{1 + \frac{2}{h}\Delta u + \frac{1}{h^2}\left((\Delta u)^2 + (\Delta v)^2\right)}. \tag{3.2.2}$$

Introducing the notation $\delta^2 = (\Delta u)^2 + (\Delta v)^2$, we can write

$$d = h\sqrt{1 + \frac{2}{h}\Delta u + \frac{1}{h^2}\delta^2}. \tag{3.2.3}$$

For small displacements, $(\Delta u, \Delta v \ll h)$, we apply a Taylor expansion for the square root keeping terms to first order, we obtain

$$\sqrt{1 + \frac{2}{h}\Delta u + \frac{1}{h^2}\delta^2} \approx 1 + \frac{1}{2}\left(\frac{2}{h}\Delta u + \frac{1}{h^2}\delta^2\right). \tag{3.2.4}$$

Thus, the deformed distance is approximated by

$$d \approx h + \Delta u + \frac{1}{2h}\delta^2. \tag{3.2.5}$$

The spring extension relative to the rest length, denoted by $\phi_{m,n,ho}$, where the

subscript h refers to the horizontal NNI, is given by

$$\phi_{m,n,h} = d - h \tag{3.2.6}$$

$$= (u_{m+2,n} - u_{m,n}) + \frac{1}{2h}\left[(u_{m+2,n} - u_{m,n})^2 + (v_{m+2,n} - v_{m,n})^2\right]. \tag{3.2.7}$$

The potential energy associated with the horizontal spring, V_h, is given by

$$V_h(\phi) = \frac{1}{2}\rho\,\phi^2. \tag{3.2.8}$$

3.2.2 Diagonal spring extensions and potential energy

To derive the diagonal spring extension, denoted by d subscript, in a manner similar to the horizontal case discussed in Section 3.2.1, we consider neighbouring nodes located at (m, n) and $(m+1, n+1)$. Their displacements are $(u_{m,n}, v_{m,n})$ and $(u_{m+1,n+1}, v_{m+1,n+1})$, respectively. The reference (undeformed) vector between these nodes has components $\left(\frac{h}{2}, \frac{\sqrt{3}h}{2}\right)$. The relative displacements are defined as $\Delta u = u_{m+1,n+1} - u_{m,n}$, $\Delta v = v_{m+1,n+1} - v_{m,n}$. The deformed relative vector becomes $\Delta\mathbf{r} = \left(\frac{h}{2} + \Delta u, \frac{\sqrt{3}h}{2} + \Delta v\right)$. Thus, the squared distance is

$$d^2 = \left(\frac{h}{2} + \Delta u\right)^2 + \left(\frac{\sqrt{3}h}{2} + \Delta v\right)^2 \tag{3.2.9}$$

$$= h^2 + h(\Delta u + \sqrt{3}\Delta v) + \delta^2, \tag{3.2.10}$$

taking the square root and expanding for small displacements, we find

$$d = h\sqrt{1 + \frac{\Delta u + \sqrt{3}\Delta v}{h} + \frac{\delta^2}{h^2}} \tag{3.2.11}$$

$$\approx h + \frac{1}{2}(\Delta u + \sqrt{3}\Delta v). \tag{3.2.12}$$

The diagonal spring extension relative to h, denoted by $\phi_{m,n,d}$, is therefore

$$\phi_{m,n,d} = d - h \tag{3.2.13}$$

$$= \frac{1}{2}\left(u_{m+1,n+1} - u_{m,n} + \sqrt{3}(v_{m+1,n+1} - v_{m,n})\right). \tag{3.2.14}$$

Thus, to leading order,

$$\phi_{m,n,d} \approx \frac{1}{2}(\Delta u + \sqrt{3}\Delta v). \tag{3.2.15}$$

The potential energy associated with these diagonal interactions, V_d, is given by

$$V_d = \frac{\rho}{8}(\Delta u)^2 + \frac{3\rho}{8}(\Delta v)^2 + \frac{\sqrt{3}\rho}{4}(\Delta u)(\Delta v). \tag{3.2.16}$$

Similarly, for the diagonal spring denoted by e subscript, which connects nodes (m, n) and $(m-1, n-1)$, defining $\Delta u = u_{m-1,n-1} - u_{m,n}, \Delta v = v_{m-1,n-1} - v_{m,n}$, the corresponding potential energy V_e is

$$V_e = \frac{\rho}{8}(\Delta u)^2 + \frac{3\rho}{8}(\Delta v)^2 - \frac{\sqrt{3}\rho}{4}(\Delta u)(\Delta v). \tag{3.2.17}$$

3.2.3 Hamiltonian of the System

The full Hamiltonian for the two-dimensional triangular lattice is given by

$$H(u_{m,n}, v_{m,n}) = \sum_m \sum_n \left\{ \frac{m}{2}\left(\frac{du_{m,n}}{dt}\right)^2 + \frac{m}{2}\left(\frac{dv_{m,n}}{dt}\right)^2 \right.$$
$$\left. + V_o(u_{m,n}, v_{m,n}) + V_h(\phi_{m,n,h}) + V_d(\phi_{m,n,d}) + V_e(\phi_{m,n,e}) \right\}, \tag{3.2.18}$$

where V_o is the onsite potential energy, given by

$$V_o = \frac{1}{2}\Omega^2(u_{m,n}^2 + v_{m,n}^2) + \frac{1}{4}\lambda(u_{m,n}^2 + v_{m,n}^2)^2 + \frac{1}{3}\eta\, u_{m,n}(u_{m,n}^2 - 3v_{m,n}^2) + \frac{1}{3}\zeta\, v_{m,n}(v_{m,n}^2 - 3u_{m,n}^2), \tag{3.2.19}$$

where Ω represents the harmonic frequency, λ characterises the isotropic quartic nonlinearity, and η, ζ quantify the degree of anisotropy.

When $\eta = \zeta = 0$, the onsite potential V_o is isotropic, meaning the restoring force is the same in all directions. However, if either η or ζ is nonzero, the onsite potential becomes anisotropic, leading to direction-dependent restoring forces.

The onsite potential must be symmetric under reflections $k \leftrightarrow -k$, and invariant under 120° rotations. In multilayer configurations, the arrangement of atoms can produce anisotropy, even if the distance and angles between neighbouring atoms remain unchanged. Such cases with nonzero η and ζ are illustrated in Figures 3.2 and 3.3.

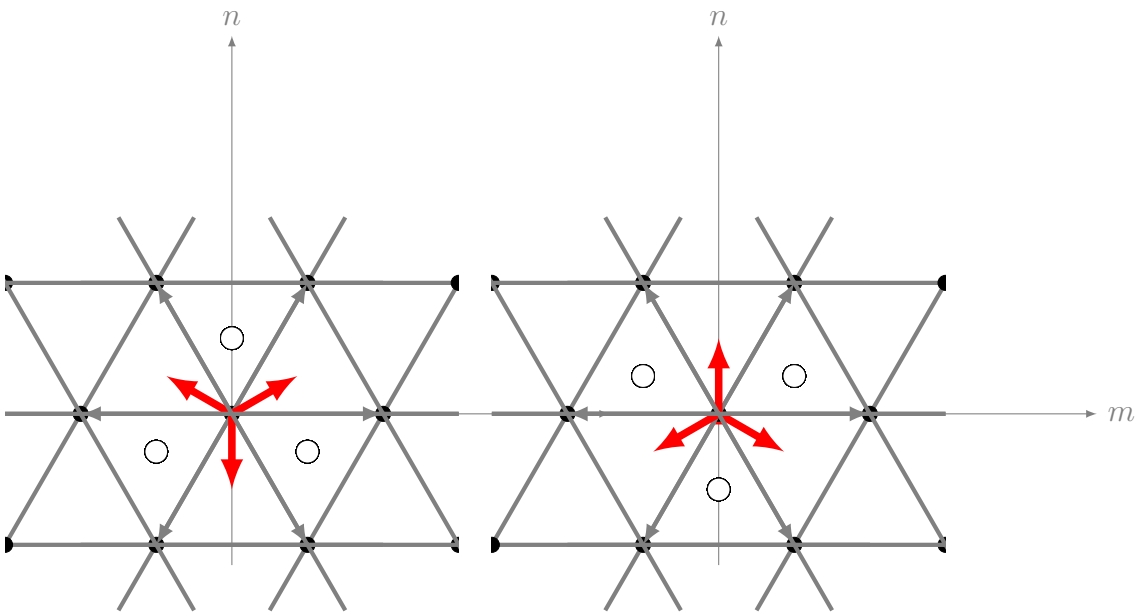

Figure 3.2: A 2D triangular lattice configuration shows the onsite potential V_o, which arises due to atoms in the layers above and below.

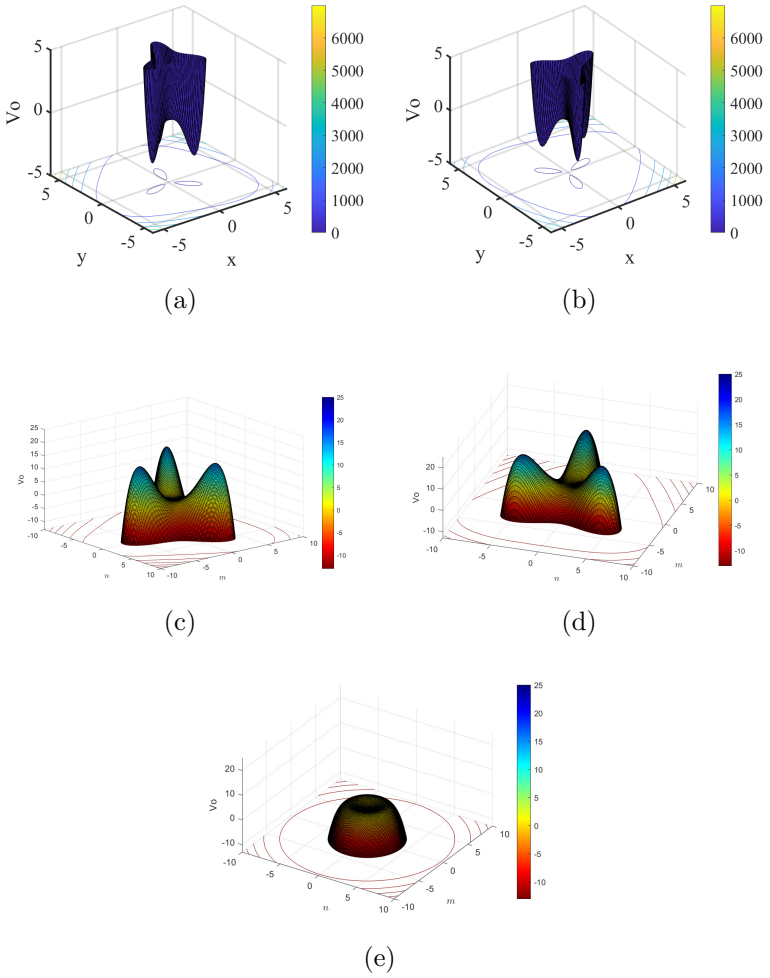

Figure 3.3: 3D plots of the onsite potential energy V_o. (a) $\eta = 0$, $\zeta = 2\sqrt{2}$; (b) $\eta = 0$, $\zeta = -2\sqrt{2}$, $\Omega = 1$, $\lambda = 1$; (c) $\eta = \zeta = 0$, $\Omega = 1$, $\lambda = -1$; (d) $\eta = 0$, $\zeta = 1$, $\Omega = 1$, $\lambda = -1$; (e) $\eta = 0$, $\zeta = -1$, $\Omega = 1$, $\lambda = -1$.

The equations of motion derived from the Hamiltonian (3.2.18) are given by

$$\begin{aligned} m\frac{d^2u_{m,n}}{dt^2} =& -\Omega^2 u_{m,n} - \lambda u_{m,n}\left(u_{m,n}^2 + v_{m,n}^2\right) - \eta u_{m,n}^2 + \eta v_{m,n}^2 + 2\zeta u_{m,n}v_{m,n} \\ &+ \rho\left(u_{m+2,n} - 2u_{m,n} + u_{m-2,n}\right) \\ &+ \frac{\rho}{4}\left[u_{m+1,n+1} - 4u_{m,n} + u_{m-1,n-1} + u_{m+1,n-1} + u_{m-1,n+1}\right] \\ &+ \frac{\sqrt{3}\rho}{4}\left[v_{m+1,n+1} + v_{m-1,n-1} - v_{m+1,n-1} - v_{m-1,n+1}\right], \qquad (3.2.20) \\ m\frac{d^2v_{m,n}}{dt^2} =& -\Omega^2 v_{m,n} - \lambda v_{m,n}\left(u_{m,n}^2 + v_{m,n}^2\right) + 2\eta v_{m,n}u_{m,n} - \zeta v_{m,n}^2 + \zeta u_{m,n}^2 \\ &+ \frac{3\rho}{4}\left[v_{m+1,n+1} - 4v_{m,n} + v_{m-1,n-1} + v_{m-1,n+1} + v_{m+1,n-1}\right] \\ &+ \frac{\sqrt{3}\rho}{4}\left[u_{m+1,n+1} + u_{m-1,n-1} - u_{m+1,n-1} - u_{m-1,n+1}\right]. \qquad (3.2.21) \end{aligned}$$

3.3 Asymptotic Analysis

To obtain an asymptotic solution to the equations of motion, we introduce a small parameter $\varepsilon \ll 1$, representing the amplitude of the leading-order envelope. We define a long spatial scale via the transformations $x = \varepsilon m$ and $y = \varepsilon n\sqrt{3}$, along with two time scales $\tau = \varepsilon t$ and $T = \varepsilon^2 t$, following the method of multiple scales [20]. The phase of the linear waves is represented by $\theta = km + l\sqrt{3}n - \omega(k,l)t$, where $\omega(k,l)$ is the dispersion relation. We denote $F(x,y,\tau,T)$ and $P(x,y,\tau,T)$ as the slowly varying complex envelopes of the $u_{m,n}$ and $v_{m,n}$, respectively. We seek solutions in the form

$$\begin{aligned} u_{m,n}(t) &= \varepsilon e^{i\theta} F(x,y,\tau,T) + \varepsilon^2 \left[e^{2i\theta} G_2 + e^{i\theta} G_1 + G_0\right] \\ &\quad + \varepsilon^3 \left[e^{3i\theta} H_3 + e^{2i\theta} H_2 + e^{i\theta} H_1 + H_0\right] + \cdots + \text{c.c.}, \end{aligned} \tag{3.3.1}$$

$$\begin{aligned} v_{m,n}(t) &= \varepsilon e^{i\theta} P(x,y,\tau,T) + \varepsilon^2 \left[e^{2i\theta} Q_2 + e^{i\theta} Q_1 + Q_0\right] \\ &\quad + \varepsilon^3 \left[e^{3i\theta} R_3 + e^{2i\theta} R_2 + e^{i\theta} R_1 + R_0\right] + \cdots + \text{c.c.}, \end{aligned} \tag{3.3.2}$$

where G_j, Q_j represent second-order corrections in ε, and H_j, R_j represent third-order corrections, with $j = 0, 1, 2$. All correction terms are functions of (x,y,τ,T) and account for nonlinear contributions that generate additional harmonic modes. Substituting the expansions (3.3.1)–(3.3.2) into the equations of motion (3.2.20)–(3.2.21), we expand all terms in powers of ε. The time derivative expanded as

$$\frac{d}{dt} = \frac{\partial}{\partial t} + \varepsilon \frac{\partial}{\partial \tau} + \varepsilon^2 \frac{\partial}{\partial T} \tag{3.3.3}$$

By collecting terms of the same order in ε and harmonics $e^{si\theta}$ for $s = 0, 1, 2, \ldots$, we derive a hierarchy of equations that determine the evolution of the envelope functions F, P, and their associated correction terms.

To perform a systematic asymptotic analysis, we expand the right-hand side of the equations of motion (3.2.20)–(3.2.21) term by term, and collect coefficients

of each harmonic component at successive orders of the small parameter ε. This expansion allows us to isolate the behaviour of each mode and extract the relative amplitudes, including the relative amplitude $C(k,l)$, which describes the coupling between F and P components.

3.3.1 Dispersion relation at $\mathcal{O}(\varepsilon e^{i\theta})$

At leading order $\mathcal{O}(\varepsilon e^{i\theta})$, the reduced system yields the linear dispersion relation:

$$\mathbf{M}\begin{pmatrix} F \\ P \end{pmatrix} = \begin{pmatrix} 0 \\ 0 \end{pmatrix}, \tag{3.3.4}$$

where the coefficient matrix $\mathbf{M}$ is given by

$$\mathbf{M} = \begin{pmatrix} \Omega^2 - \omega^2 + 4\rho\sin^2 k + \rho - \rho\cos k\cos(\sqrt{3}l) & \sqrt{3}\rho\sin k\sin(\sqrt{3}l) \\ \sqrt{3}\rho\sin k\sin(\sqrt{3}l) & \Omega^2 - \omega^2 + 3\rho - 3\rho\cos k\cos(\sqrt{3}l) \end{pmatrix}. \tag{3.3.5}$$

A non-trivial solution $(F,P) \neq 0$ exists only if $\det(\mathbf{M}) = 0$. Solving this condition yields a quartic equation in ω, which can be expressed as

$$\omega^4 - \mathrm{tr}\omega^2 + \det = 0,$$

where

$$\begin{aligned} \mathrm{tr} &= 2\Omega^2 + 4\rho\sin^2 k + 4\rho - 4\rho\cos k\cos(\sqrt{3}l), \\ \det &= \left(\Omega^2 - \omega^2 + 4\rho\sin^2 k + \rho - \rho\cos k\cos(\sqrt{3}l)\right), \\ &\quad \left(\Omega^2 - \omega^2 + 3\rho - 3\rho\cos k\cos(\sqrt{3}l)\right) - 3\rho^2\sin^2 k\sin^2(\sqrt{3}l). \end{aligned} \tag{3.3.6}$$

Solving the resulting equation provides two branches of the dispersion relation

$$\omega^2(k,l) = \frac{1}{2}\left(\mathrm{tr} \pm \sqrt{\mathrm{tr}^2 - 4\det}\right). \tag{3.3.7}$$

We identify DB solutions either on the upper (optical) or lower (acoustic)

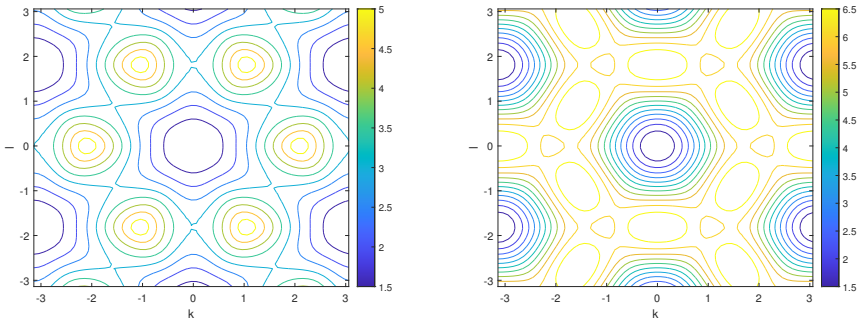

(a) ω_{ac}^2 (b) ω_{op}^2

Figure 3.4: Contour plots of $\omega_{ac}^2, \omega_{op}^2$ for $\Omega = \rho = 1$. Wavenumbers span the ranges $-\pi \leq k \leq \pi$, $-2.5 \leq l \leq 2.5$.

branches, or at specific Dirac points, special points in the dispersion relation where two branches intersect linearly, leading to conical band crossings. To minimise resonance with linear waves, DBs are typically near band edges (maxima or minima) or Dirac crossings. Figure 3.4 shows contour plots of $\omega(k, l)$ for $\rho = \Omega = 1$. The Dirac points are located by solving $\mathrm{tr}^2 = 4\,\mathrm{det}$, and five special points are summarised in Table 3.1.

Description	**Frequency**	**Example Points**
Case 1: Global minimum	$\omega = \Omega$	$(0,0)$, $\left(0, \frac{\pm 2\pi}{\sqrt{3}}\right)$, $\left(\pm\pi, \frac{\pm\pi}{\sqrt{3}}\right)$
Case 2: Saddle points	$\omega_{ac} = \sqrt{\Omega^2 + 2\rho}$	$\left(0, \frac{\pm\pi}{\sqrt{3}}\right)$, $\left(\frac{\pm\pi}{2}, \frac{\pm\pi}{2\sqrt{3}}\right)$
Case 3: Global maximum	$\omega_{op} = \sqrt{\Omega^2 + 6\rho}$	Same as Case 3 points
Case 4: Dirac	$\omega = \sqrt{\Omega^2 + 4.5\rho}$	$\left(\frac{\pm\pi}{3}, \frac{\pm\pi}{\sqrt{3}}\right)$, $\left(\frac{\pm 2\pi}{3}, 0\right)$
Case 5: Saddle points	$\omega_{op} = \sqrt{\Omega^2 + 5\rho}$	$\left(\pm\cos^{-1}\left(\frac{-1}{8}\right), 0\right)$, $\left(\frac{\pm 1}{2}\cos^{-1}\left(\frac{-1}{8}\right), \frac{\pm\sqrt{3}}{2}\cos^{-1}\left(\frac{-1}{8}\right)\right)$

Table 3.1: Summary of special points, including Dirac points.

The condition $\det(\mathbf{M}) = 0$ ensures the existence of non-trivial solutions $(F, P) \neq 0$ in equation (3.3.5). To determine C, we define the vector $(1, C)^T$ to lie in the null space of the matrix $\mathbf{M}$. This vector is orthogonal to the range of $\mathbf{M}$, which

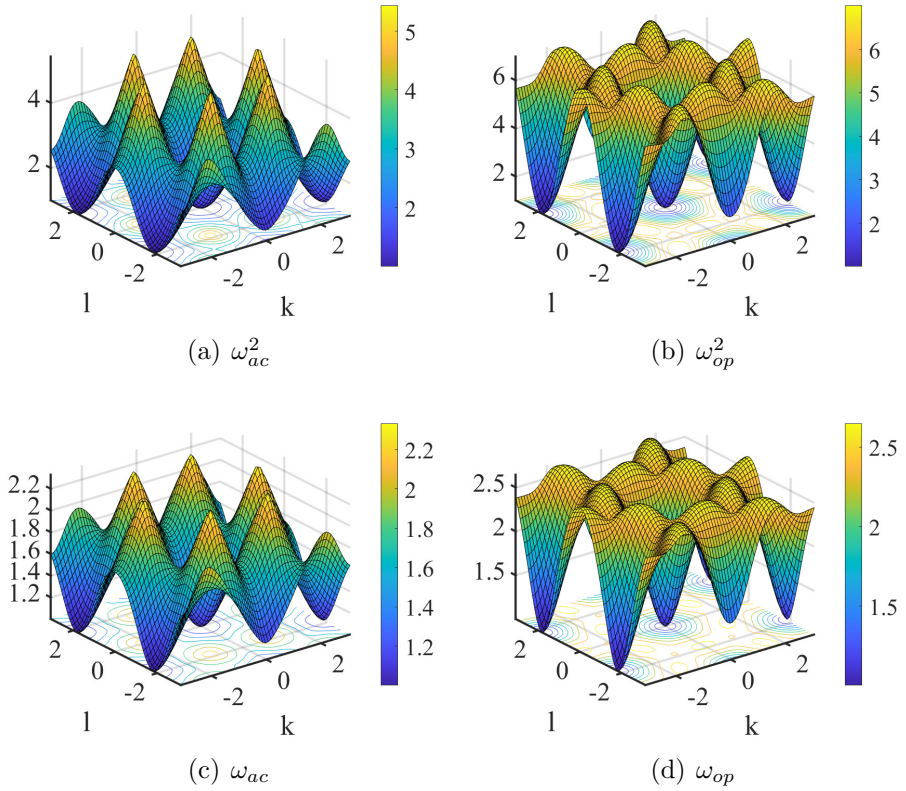

Figure 3.5: 3D plots of ω^2 and ω for both optical and acoustic branches, with $\Omega = \rho = m = 1$, over the domain $-\pi \leq k, l \leq \pi$.

is spanned by $(C, -1)^T$. We now determine the corresponding relative amplitude by the form $(F, P) = F(1, C)^T$, which then allows us to solve explicitly for C yields

$$C_{op} = \frac{-\sqrt{3}\rho \sin k \sin(\sqrt{3}l)}{-\left(\Omega^2 - \omega_{op}^2 + 3\rho(1 - \cos k \cos(\sqrt{3}l))\right)}, \tag{3.3.8}$$

$$C_{ac} = \frac{-\sqrt{3}\rho \sin k \sin(\sqrt{3}l)}{-\left(\Omega^2 - \omega_{ac}^2 + 3\rho(1 - \cos k \cos(\sqrt{3}l))\right)}. \tag{3.3.9}$$

Figure 3.6 shows 3D plots of C for both optical and acoustic branches.

3.3.2 Zeroth harmonic $\mathcal{O}(\varepsilon^2 e^0)$ terms

We now calculate the zeroth harmonic terms arising at order $\mathcal{O}(\varepsilon^2 e^0)$, obtained by substituting the expansions (3.3.1)–(3.3.2) into the equations of mo-

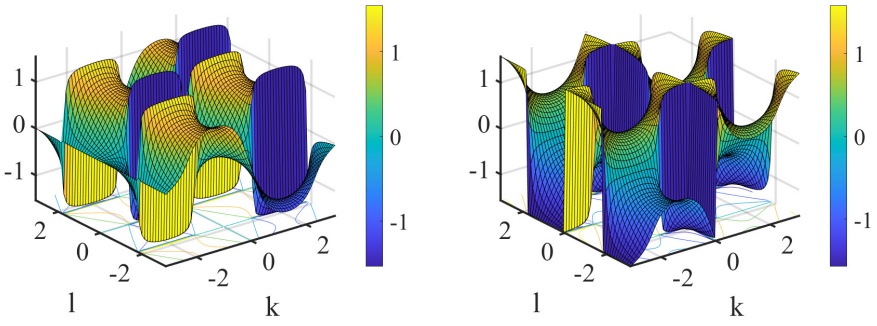

(a) $\tan^{-1}(C_{ac})$ (b) $\tan^{-1}(C_{op})$

Figure 3.6: Plots of C_{ac} and C_{op}, including $\tan^{-1}(C)$, for $\Omega = \rho = m = 1$. The wavenumber ranges are given by $-\pi \leq k, l \leq \pi$.

tion (3.2.20)–(3.2.21). This yields the following equations

$$0 = -\Omega^2 \left(G_0 + G_0^*\right) - 2\eta|F|^2 + 2\eta|P|^2 + 2\zeta \left(P\bar{F} + F\bar{P}\right), \tag{3.3.10}$$

$$0 = -\Omega^2 \left(Q_0 + Q_0^*\right) + 2\eta \left(F\bar{P} + \bar{F}P\right) + 2\zeta \left(|F|^2 - |P|^2\right), \tag{3.3.11}$$

where we assume $G_0 = G_0^*$ and $Q_0 = Q_0^*$, such that the imaginary parts $\mathrm{Im}(G_0)$ and $\mathrm{Im}(Q_0)$ vanish. This assumption is justified since the imaginary components do not appear in the leading-order ansatz expansions for $u_{m,n}$ and $v_{m,n}$ in equations (3.3.1)–(3.3.2). Using the relation $P = CF$, the expressions simplify, yielding

$$G_0 = |F|^2 \frac{(\eta(C^2 - 1) + 2C\zeta)}{\Omega^2} = |F|^2 \gamma_0, \tag{3.3.12}$$

$$Q_0 = |F|^2 \frac{(2C\eta - \zeta(C^2 - 1))}{\Omega^2} = |F|^2 \bar{\gamma}_0, \tag{3.3.13}$$

where γ_0 and $\bar{\gamma}_0$ are the corresponding nonlinear coefficients.

3.3.3 Second harmonic $\mathcal{O}(\varepsilon^2 e^{2i\theta})$ terms

Next, we collect the second harmonic terms at order $\mathcal{O}(\varepsilon^2 e^{2i\theta})$, resulting in the matrix equation

$$\mathbf{M}_2 \begin{pmatrix} G_2 \\ Q_2 \end{pmatrix} = \begin{pmatrix} \eta(C^2-1) + 2C\zeta \\ 2C\eta - (C^2-1)\zeta \end{pmatrix} F^2, \tag{3.3.14}$$

where the matrix $\mathbf{M}_2$ is defined as

$$\mathbf{M}_2 = \begin{pmatrix} -4\omega^2 + \Omega^2 + 4\rho\sin^2(2k) + \rho a_1 & \sqrt{3}\rho\sin(2k)\sin(2\sqrt{3}l) \\ \sqrt{3}\rho\sin(2k)\sin(2\sqrt{3}l) & -4\omega^2 + \Omega^2 + 3\rho a_1 \end{pmatrix}, \tag{3.3.15}$$

with $a_1 = 1 - \cos(2k)\cos(2\sqrt{3}l)$. Solving equation (3.3.14) gives

$$\begin{pmatrix} G_2 \\ Q_2 \end{pmatrix} = F^2 \mathbf{M}_2^{-1} \begin{pmatrix} \eta(C^2-1) + 2C\zeta \\ 2C\eta - (C^2-1)\zeta \end{pmatrix}. \tag{3.3.16}$$

Expanding the inverse explicitly, we obtain

$$G_2 = F^2 \frac{M_{22}\left(\eta(C^2-1) + 2C\zeta\right) - M_{21}\left(2C\eta - (C^2-1)\zeta\right)}{M_{11}M_{22} - M_{12}^2} = F^2\gamma_2, \tag{3.3.17}$$

$$Q_2 = F^2 \frac{M_{11}\left(\eta(C^2-1) + 2C\zeta\right) - M_{12}\left(2C\eta - (C^2-1)\zeta\right)}{M_{11}M_{22} - M_{12}^2} = F^2\bar{\gamma}_2. \tag{3.3.18}$$

The γ_2 and $\bar{\gamma}_2$ are the coefficients of second-harmonic generation in the system.

3.3.4 Harmonic $\mathcal{O}(\varepsilon^2 e^{i\theta})$ terms

Following the asymptotic expansion, we obtain the system

$$\mathbf{M} \begin{pmatrix} G_1 \\ Q_1 \end{pmatrix} = \begin{pmatrix} A_1 \\ B_1 \end{pmatrix}, \tag{3.3.19}$$

where the matrix $\mathbf{M}$ is defined in equation (3.3.5), and the right-hand side components A_1 and B_1 are given by

$$\begin{aligned} A_1 &= 2i\omega F_\tau - 4i\rho\sin(2k)F_x \\ &\quad + \sqrt{3}\rho\left(iCF_x\cos(k)\sin(\sqrt{3}l) + i\sqrt{3}CF_y\sin(k)\cos(\sqrt{3}l)\right) \\ &\quad + i\rho F_x\sin(k)\cos(\sqrt{3}l) + i\rho\sqrt{3}F_y\cos(k)\sin(\sqrt{3}l), \qquad (3.3.20) \\ B_1 &= 2i\omega P_\tau + \sqrt{3}\rho\left(iF_x\cos(k)\sin(\sqrt{3}l) + i\sqrt{3}F_y\sin(k)\cos(\sqrt{3}l)\right) \\ &\quad + 3\rho\left(iCF_x\sin(k)\cos(\sqrt{3}l) + i\sqrt{3}CF_y\cos(k)\sin(\sqrt{3}l)\right). \qquad (3.3.21) \end{aligned}$$

Since the right-hand side of equation (3.3.19) contains only first-order derivatives of F and P, we seek a travelling wave solution. Substituting $P = CF$ and introducing the travelling variables

$$\begin{aligned} F(x,y,\tau,T) = F(Z,W,T), \qquad P(x,y,\tau,T) = P(Z,W,T), \\ Z = x - U\tau, \qquad W = y - V\tau, \qquad (3.3.22) \end{aligned}$$

where Z, W are travelling wave coordinates, the expressions for A_1 and B_1 become

$$\begin{aligned} A_1 = &-2i\omega(F_Z U + F_W V) + 4i\rho\sin(2k)F_Z \\ &+ \rho\left(iCF_Z\sqrt{3}\cos(k)\sin(\sqrt{3}l) + i3CF_W\sin(k)\cos(\sqrt{3}l)\right) \\ &+ iF_Z\sin(k)\cos(\sqrt{3}l) + i\sqrt{3}F_W\cos(k)\sin(\sqrt{3}l), \qquad (3.3.23) \\ B_1 = &-2i\omega C(F_Z U + F_W V) + \sqrt{3}\rho\left(iF_Z\cos(k)\sin(\sqrt{3}l) + i\sqrt{3}F_W\sin(k)\cos(\sqrt{3}l)\right) \\ &+ 3\rho\left(iCF_Z\sin(k)\cos(\sqrt{3}l) + i\sqrt{3}CF_W\cos(k)\sin(\sqrt{3}l)\right). \qquad (3.3.24) \end{aligned}$$

To solve for G_1 and Q_1, we derive the consistency condition

$$A_1 + CB_1 = 0. \qquad (3.3.25)$$

The system has a solution only if the right-hand side vector $(A_1, B_1)^T$ lies in

the range of $\mathbf{M}$. Since the range of $\mathbf{M}$ is orthogonal to the vector $(1, C)$, then solvability condition is given by

$$\begin{aligned} 0 = {} & 2i\omega U(1+C^2)F_Z + 2i\omega V(1+C^2)F_W \\ & + i\rho F_Z \left[4\sin(2k) + 2\sqrt{3}C\cos(k)\sin(\sqrt{3}l) + (1+3C^2)\sin(k)\cos(\sqrt{3}l)\right] \\ & + i\rho F_W \left(6C\cos(\sqrt{3}l)\sin(k) + \sqrt{3}(1+3C^2)\cos(k)\sin(\sqrt{3}l)\right). \end{aligned} \tag{3.3.26}$$

Solving this condition yields expressions for the group velocities U and V

$$U = \frac{-\rho}{2\omega(1+C^2)}\left[4\sin(2k) + 2\sqrt{3}C\cos(k)\sin(\sqrt{3}l) + (1+3C^2)\sin(k)\cos(\sqrt{3}l)\right], \tag{3.3.27}$$

$$V = \frac{-\rho}{2\omega(1+C^2)}\left[6C\cos(\sqrt{3}l)\sin(k) + \sqrt{3}(1+3C^2)\cos(k)\sin(\sqrt{3}l)\right]. \tag{3.3.28}$$

These velocity components are illustrated in Figure 3.7. The total wave speed is given by $S = \sqrt{U^2 + V^2}$.

The general solution to equation (3.3.19) takes the form

$$\begin{pmatrix} G_1 \\ Q_1 \end{pmatrix} = \hat{G}\begin{pmatrix} 1 \\ C \end{pmatrix} + \tilde{G}\begin{pmatrix} C \\ -1 \end{pmatrix}, \tag{3.3.29}$$

where $(1, C)^T$ lies in the kernel of $\mathbf{M}$. The term $\hat{G}$ can be absorbed into F via the transformation $F \to F + \varepsilon\hat{G}$, and without loss of generality, we take $\hat{G} = 0$. Thus, we solve

$$\begin{pmatrix} A_1 \\ B_1 \end{pmatrix} = \tilde{G}\,\mathbf{M}\begin{pmatrix} C \\ -1 \end{pmatrix}. \tag{3.3.30}$$

The solution for $\tilde{G}$ can be written as

$$\tilde{G} = i\tilde{U}F_Z + i\tilde{V}F_W, \tag{3.3.31}$$

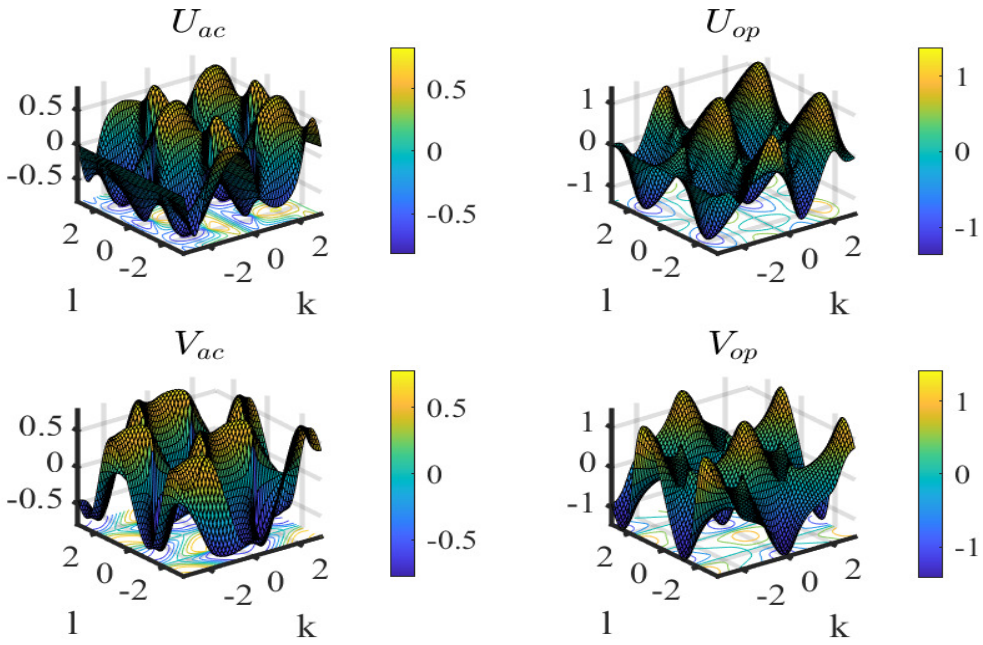

(a)

Figure 3.7: The plots of optical and acoustic mods of U, V for both $(U, V)_{ac}, (U, V)_{op}$, and at $\Omega = \rho = m = 1$, and wave number $-\pi \leq k \leq \pi, -\pi \leq l \leq \pi$.

which leads to the expressions

$$G_1 = -iC\tilde{U}F_Z - iC\tilde{V}F_W, \quad Q_1 \qquad = i\tilde{U}F_Z + i\tilde{V}F_W. \tag{3.3.32}$$

Here, $\tilde{U}$ and $\tilde{V}$ are defined as

$$\tilde{U} = \frac{2\omega CU + \rho\left[\sqrt{3}\cos(k)\sin(\sqrt{3}l) + 3C\sin(k)\cos(\sqrt{3}l)\right]}{C\rho\sqrt{3}\sin(k)\sin(\sqrt{3}l) - \left[\Omega^2 - \omega^2 + 3\rho(1 - \cos(k)\cos(\sqrt{3}l))\right]}, \tag{3.3.33}$$

$$\tilde{V} = \frac{2\omega CV + \rho\left[\sqrt{3}\sin(k)\cos(\sqrt{3}l) + 3\sqrt{3}C\cos(k)\sin(\sqrt{3}l)\right]}{C\rho\sqrt{3}\sin(k)\sin(\sqrt{3}l) - \left[\Omega^2 - \omega^2 + 3\rho(1 - \cos(k)\cos(\sqrt{3}l))\right]}. \tag{3.3.34}$$

These quantities are illustrated in Figure 3.8. The $\tilde{U}$ and $\tilde{V}$ correspond to spatial shifts in the Z and W directions and describe corrections to the phase propagation of the breather. The total correction is given by $\tilde{S} = \sqrt{\tilde{U}^2 + \tilde{V}^2}$, analogous to the group speed $S = \sqrt{U^2 + V^2}$. Both are plotted in Figure 3.9.

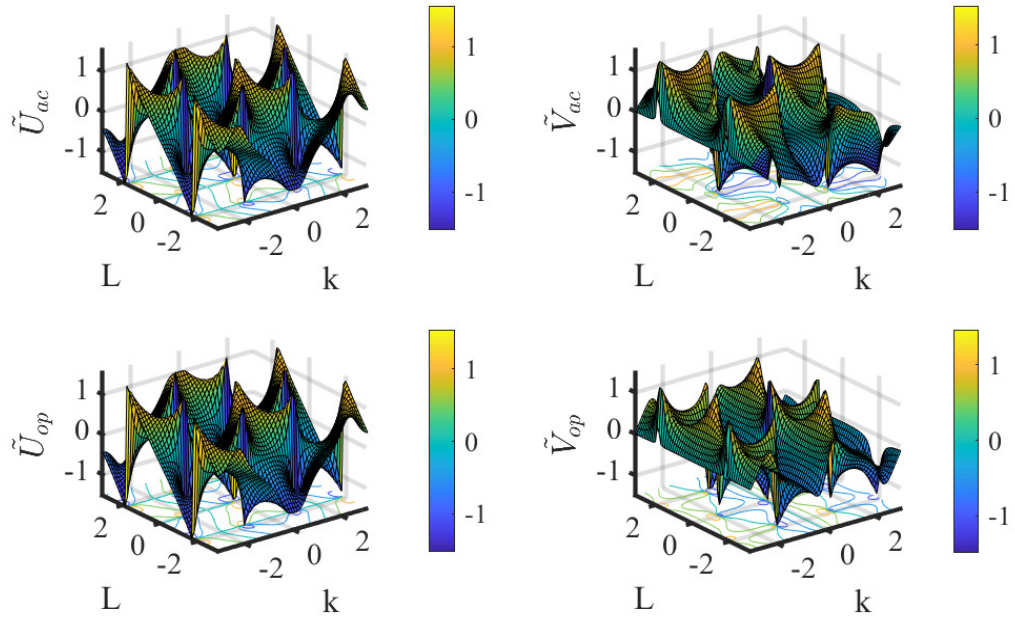

(a)

Figure 3.8: The plots of $\tan^{-1}$ of optical and acoustic mods of $\tilde{U}, \tilde{V}$ for both $(\tilde{U}, \tilde{V})_{ac}, (\tilde{U}, \tilde{V})_{op}$, and at $\Omega = \rho = m = 1$, and wave number $-\pi \leq k \leq \pi, -\pi \leq l \leq \pi$.

3.3.5 Harmonic at $\mathcal{O}(\varepsilon^3 e^{i\theta})$ terms

At this order, we collect the asymptotic terms to $\mathcal{O}(\varepsilon^3 e^{i\theta})$. This yields the following

$$\mathbf{M} \begin{pmatrix} H_1 \\ R_1 \end{pmatrix} = \begin{pmatrix} A_2 \\ B_2 \end{pmatrix}, \tag{3.3.35}$$

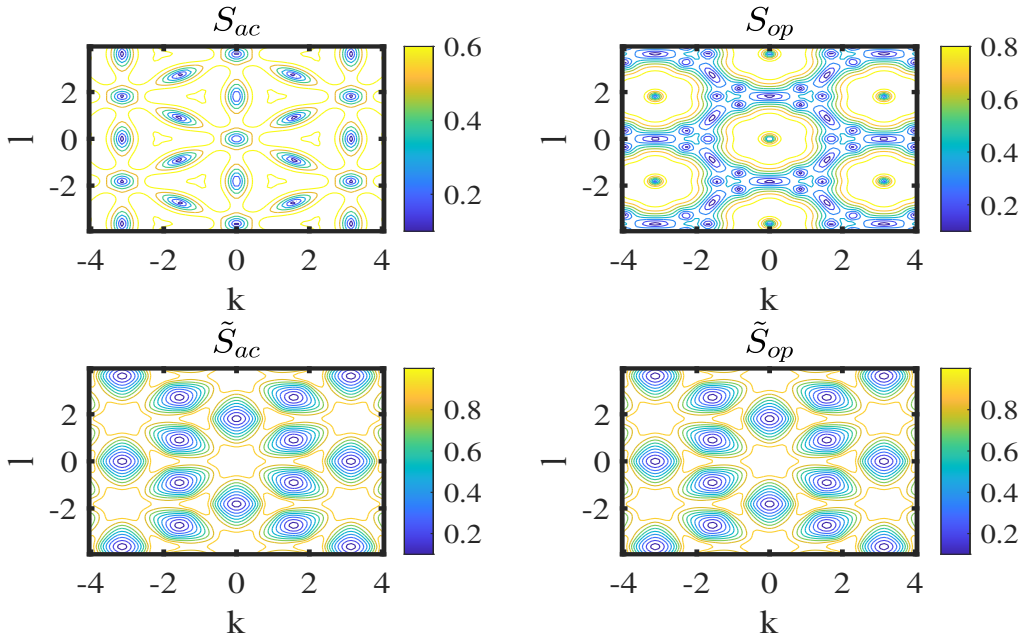

(a)

Figure 3.9: Contour plots of optical $\tan^{-1}(S), \tan^{-1}(\tilde{S})$ in right panel and acoustic mods in left panel , both at $\Omega = \rho = m = 1$, and wave number $-4 \leq k \leq 4$,$-4 \leq l \leq 4$.

where $\mathbf{M}$ is defined in equation (3.3.5), and the components A_2 and B_2 are given explicitly by the following expressions

$$\begin{aligned}
A_2 =& 2i\omega\left(F_T + G_{1\tau}\right) - F_{\tau\tau} + 2\eta\left(PQ_0 + \bar{P}Q_2 + P\bar{Q}_0 - \bar{F}Q_2 - FG_0 - F\bar{G}_0\right) \\
&+ 2\zeta\left(G_2\bar{P} + FQ_0 + \bar{F}Q_2 + PG_0 + P\bar{G}_0 + F\bar{Q}_0\right) - \lambda\left(3|F|^2F + 2|P|^2F + \bar{F}P^2\right) \\
&+ 4i\rho\sin(2k)G_{1Z} + 4\rho\cos(2k)F_{ZZ} \\
&+ \frac{\rho}{4}\Big[4i\cos(l\sqrt{3})\sin(k)G_{1Z} + 4i\sqrt{3}\sin(l\sqrt{3})\cos(k)G_{1W} \\
&\quad + \cos(l\sqrt{3})\cos(k)(2F_{ZZ} + 6F_{WW}) - 4\sqrt{3}\sin(l\sqrt{3})\sin(k)F_{ZW}\Big] \\
&+ \frac{\sqrt{3}\rho}{4}\Big[4i\cos(k)\sin(l\sqrt{3})Q_{1Z} + 4i\sqrt{3}\sin(k)\cos(l\sqrt{3})Q_{1W} \\
&\quad - \sin(l\sqrt{3})\sin(k)(2P_{ZZ} + 6P_{WW}) + 4\sqrt{3}\cos(l\sqrt{3})\cos(k)P_{ZW}\Big].
\end{aligned} \tag{3.3.36}$$

$$
\begin{aligned}
B_2 =& 2i\omega\left(P_T + Q_{1\tau}\right) - P_{\tau\tau} + 2\eta\left(PQ_0 + \bar{P}Q_2 + P\bar{Q}_0 - \bar{F}Q_2 - FG_0 - F\bar{G}_0\right) \\
&+ 2\zeta\left(G_2\bar{P} + FQ_0 + \bar{F}Q_2 + PG_0 + P\bar{G}_0 + F\bar{Q}_0\right) - \lambda\left(3|P|^2P + 2|F|^2P + \bar{P}F^2\right) \\
&+ \frac{3\rho}{4}\Big[4i\cos(l\sqrt{3})\sin(k)Q_{1Z} + 4i\sqrt{3}\sin(l\sqrt{3})\cos(k)Q_{1W} \\
&\quad + \cos(l\sqrt{3})\cos(k)(2P_{ZZ} + 6P_{WW}) - 4\sqrt{3}\sin(l\sqrt{3})\sin(k)P_{ZW}\Big] \\
&+ \frac{\sqrt{3}\rho}{4}\Big[4i\cos(k)\sin(l\sqrt{3})G_{1Z} + 4i\sqrt{3}\sin(k)\cos(l\sqrt{3})G_{1W} \\
&\quad - \sin(l\sqrt{3})\sin(k)(2F_{ZZ} + 6F_{WW}) + 4\sqrt{3}\cos(l\sqrt{3})\cos(k)F_{ZW}\Big].
\end{aligned}
\tag{3.3.37}
$$

We now substitute the expressions for $G_{1Z}, G_{1W}, Q_{1Z}, Q_{1W}$ using equations (3.3.22), (3.3.32), (3.3.33),(3.3.34), and set $P = CF$, where $C = \sqrt{3}$. By applying the solvability condition $A_2 + CB_2 = 0.$, we collect and simplify terms to obtain the governing evolution equation for F. Rearranging the terms, we express the resulting evolution equation in the form of a 2D NLS equation

$$
0 = i\Theta F_T + D_Z F_{ZZ} + D_W F_{WW} + D_{ZW} F_{ZW} + D_N|F|^2F, \tag{3.3.38}
$$

where the coefficients Θ, D_Z, D_W, D_{ZW}, and D_N are defined by

$$
\Theta = 2\omega(1 + C^2), \tag{3.3.39}
$$

$$
\begin{aligned}
D_Z =& -(1 + C^2)U^2 + 4\rho\cos(2k) + 4C\tilde{U}\rho\sin(2k) - 2C\tilde{U}\rho\sin(k)\cos(l\sqrt{3}) \\
&+ \sqrt{3}\tilde{U}\rho(C^2 - 1)\cos(k)\sin(l\sqrt{3}) + \tfrac{1}{2}(1 + 3C^2)\cos(k)\cos(l\sqrt{3}) \\
&- \sqrt{3}\rho C\sin(k)\sin(l\sqrt{3}),
\end{aligned}
\tag{3.3.40}
$$

$$
\begin{aligned}
D_W =& -(1 + C^2)V^2 - 3\sqrt{3}C\sin(k)\sin(l\sqrt{3}) - 2\rho C\sqrt{3}\tilde{V}\sin(k)\cos(l\sqrt{3}) \\
&+ 3\rho(C^2 - 1)\tilde{V}\sin(k)\cos(l\sqrt{3}) + \tfrac{3}{2}\rho(1 + 3C^2)\cos(k)\cos(l\sqrt{3}),
\end{aligned}
\tag{3.3.41}
$$

$$
\begin{aligned}
D_{ZW} = &-2UV(1+C^2) + 4C\tilde{V}\rho\sin(2k) - 2C\tilde{V}\rho\sin(k)\cos(l\sqrt{3}) \\
&+ \sqrt{3}\tilde{V}\rho(C^2-1)\cos(k)\sin(l\sqrt{3}) \\
&+ \rho\tilde{U}\left[3(C^2-1)\cos(l\sqrt{3})\sin(k) - 2\sqrt{3}C\sin(l\sqrt{3})\cos(k)\right] \\
&+ 6C\rho\cos(k)\cos(l\sqrt{3}) - \sqrt{3}\rho(1+3C^2)\sin(k)\sin(l\sqrt{3}), \qquad (3.3.42)
\end{aligned}
$$

$$
\begin{aligned}
D_N = &\ 4\eta\left(2C\bar{\gamma}_0 + \gamma_0(C^2-1)\right) - 3\lambda(1+C^2)^2 + 2\eta\left(2C\bar{\gamma}_2 + \gamma_2(C^2-1)\right) \\
&+ 4\zeta\left(2C\gamma_0 - \bar{\gamma}_0(C^2-1)\right) + 2\eta\left(2C\gamma_2 - \bar{\gamma}_2(C^2-1)\right). \qquad (3.3.43)
\end{aligned}
$$

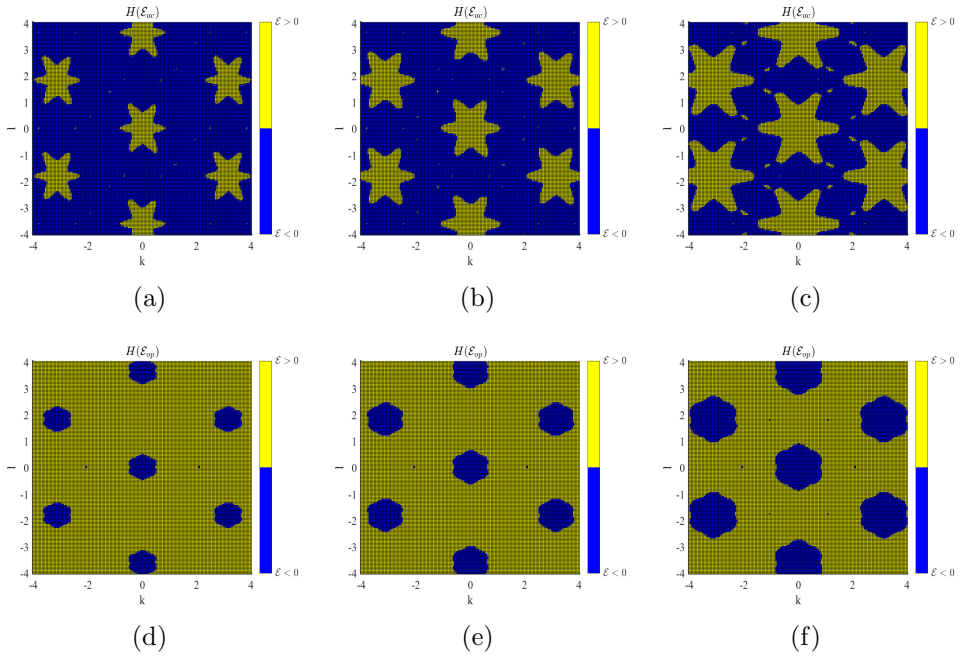

Figure 3.10: Top-view plots of $H(\mathcal{E}(k,l))$ for the acoustic(top) and optical(bottom) branches at $\Omega = 0.5$ (left), $\Omega = 1$ (middle), and $\Omega = 5$ (right), with $\lambda = 1$, $\zeta = 0$, and $\eta = 0$. The yellow region corresponds to $\mathcal{E} > 0$, while the blue region indicates $\mathcal{E} < 0$.

To eliminate the mixed derivative term F_{ZW}, we apply the change of variables

$$
\xi = W - \frac{D_{ZW}}{2D_Z}Z, \qquad (3.3.44)
$$

which diagonalises the dispersive part of the equation. Under this substitution,

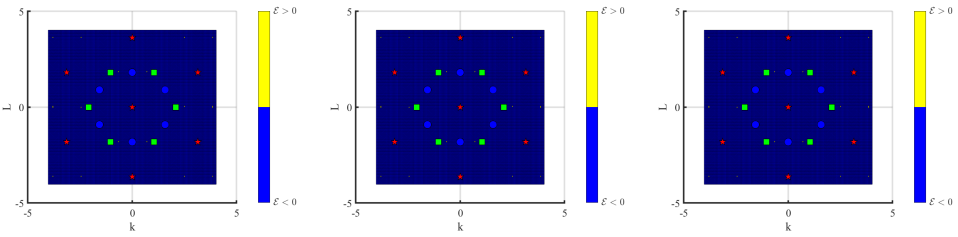

(a) $H(\mathcal{E}_{\text{ac}})H(D_N D_Z)_{\text{ac}}$ (b) $H(\mathcal{E}_{\text{ac}})H(D_N D_Z)_{\text{ac}}$ (c) $H(\mathcal{E}_{\text{ac}})H(D_N D_Z)_{\text{ac}}$

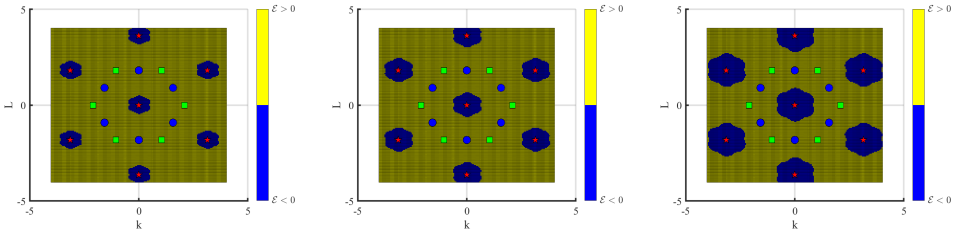

(d) $H(\mathcal{E}_{\text{op}})H(D_N D_Z)_{\text{op}}$ (e) $H(\mathcal{E}_{\text{op}})H(D_N D_Z)_{\text{op}}$ (f) $H(\mathcal{E}_{\text{op}})H(D_N D_Z)_{\text{op}}$

Figure 3.11: Top-view plots of the product $H(\mathcal{E}(k,l))H(D_N D_Z)$ for acoustic (blue) and optical (yellow and blue) branches, with $\zeta = 0$, $\eta = 0$, $\lambda = 1$, and $\rho = 1$. Panels from left to right correspond to $\Omega = 0.5$, $\Omega = 1$, and $\Omega = 5$. Star markers denote Case 1, circles represent Case 2 and 3, squares indicate Case 4, and diamonds highlight the optical Case 5 from Table 3.1.

the differential operators transform as

$$\partial_Z = \partial_Z - \frac{D_{ZW}}{2D_Z}\partial_\xi, \qquad \partial_W = \partial_\xi,$$

and the NLS equation simplifies to

$$i\Theta F_T = D_N|F|^2F + D_Z\left(F_{ZZ} + \mathcal{E}F_{\xi\xi}\right), \tag{3.3.45}$$

equation (3.3.45) is a 2D NLS whose qualitative behaviour depends critically on the sign of the dispersion and nonlinearity coefficients D_N, D_Z. The coefficient

$$\mathcal{E}(k,l) = 4D_W D_Z - D_{ZW}^2 > 0 \tag{3.3.46}$$

is known as the *ellipticity condition*. It ensures that the spatial part of the NLS equation is elliptic rather than hyperbolic. Only in the elliptic regime corresponding to the yellow regions where both the ellipticity condition $\mathcal{E}(k,l) > 0$ is satisfied does the equation support solutions that are localised in both spatial

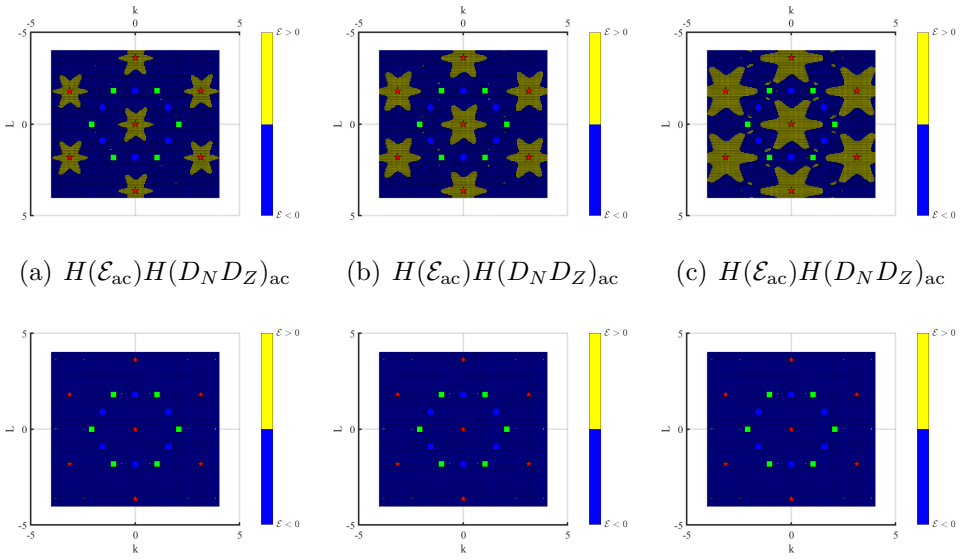

(a) $H(\mathcal{E}_{\mathrm{ac}})H(D_N D_Z)_{\mathrm{ac}}$ (b) $H(\mathcal{E}_{\mathrm{ac}})H(D_N D_Z)_{\mathrm{ac}}$ (c) $H(\mathcal{E}_{\mathrm{ac}})H(D_N D_Z)_{\mathrm{ac}}$

(d) $H(\mathcal{E}_{\mathrm{op}})H(D_N D_Z)_{\mathrm{op}}$ (e) $H(\mathcal{E}_{\mathrm{op}})H(D_N D_Z)_{\mathrm{op}}$ (f) $H(\mathcal{E}_{\mathrm{op}})H(D_N D_Z)_{\mathrm{op}}$

Figure 3.12: Top-view plots of $H(\mathcal{E}(k,l))H(D_N D_Z)$ for optical (blue) and acoustic (yellow and blue) branches with $\zeta = 0$, $\eta = 0$, $\lambda = -1$, and $\rho = 1$. Panels correspond to $\Omega = 0.5$ (left), $\Omega = 1$ (middle), and $\Omega = 5$ (right). Marker symbols indicate special cases from Table 3.1.

directions [8], [15]. In contrast, the blue regions represent non-elliptic domains where such solution becomes hyperbolic, and no localised soliton solutions are supported in 2D. These results demonstrate the sensitivity of breather existence to both the wave numbers and the choice of Ω, with the elliptic regime becoming more notable as Ω increases. Figure 3.10 presents top-view contour plots of the ellipticity condition $H(\mathcal{E}(k,l))$ for both optical and acoustic branches, evaluated at three different values of the on-site potential parameter $\Omega = 0.5, 1,$ and 5.

In addition, the product

$$\mathcal{F}(k,l) = D_N D_Z > 0, \tag{3.3.47}$$

defines the *focusing condition*, which determines whether the nonlinearity and dispersion act constructively to support bright breather-type solutions. If the focusing condition $\mathcal{F}(k,l) > 0$ is satisfied, this together with (3.3.46) indicates parameter regimes where the NLS equation is of the focusing elliptic type and

capable of supporting breather solutions [8, 9, 19]. Figure 3.11 demonstrates the sensitivity of the breather-supporting regions to changes in Ω under an isotropic onsite potential ($\zeta = \eta = 0$) with ($\lambda = 1$), while Figure 3.12 explores the impact of a negative quartic nonlinearity ($\lambda = -1$) on the existence zones. Together, the constraints $\mathcal{E} > 0$ and $\mathcal{F} > 0$ identify the regions in wavenumber space (k, l) where spatially localised breather modes can exist.

3.4 Simplification of the System at $\zeta = \eta = 0$

While the methodology developed in previous sections yields valid results for most values of (k, l), singularities arise at certain key points. For instance, the expressions for C in equations (3.3.8) and (3.3.9) become undefined at $(k, l) = (0, 0)$. In this section, we simplify the governing system by setting $\zeta = \eta = 0$, which implies $G_0 = Q_0 = G_2 = Q_2 = 0$. However, for non-zero values of either $\tilde{U}$ or $\tilde{V}$, the terms G_1 and Q_1 may still contribute.

A summary of the key stationary cases is presented in Table 3.2, with the corresponding derivations detailed in Appendix B. Cases 1 and 2, as well as the Dirac points, are analysed in Section 3.4.1.

Table 3.2: Summary of stationary optical and acoustic properties for $\lambda > 0$, $\rho > 0$, and $\Omega > 0$. Positive ellipticity ($\mathcal{E} > 0$) and focusing ($\mathcal{F} > 0$) indicate a focusing, elliptic NLS; in contrast, $\mathcal{E} < 0$ corresponds to a hyperbolic NLS.

Description	**Points**	**C**	$\mathcal{E}$	$\mathcal{F}$
Case 2				
Saddle(acustic)	$\left(0, \frac{\pm\pi}{\sqrt{3}}\right)$	0	< 0	
	$\left(\frac{\pm\pi}{2}, \frac{\pm\pi}{2\sqrt{3}}\right)$	$\pm\sqrt{3}$	< 0	
Case 3				
Global maximum	$\left(0, \frac{\pm\pi}{\sqrt{3}}\right)$	∞	> 0	> 0
	$\left(\frac{\pm\pi}{2}, \frac{\pm\pi}{2\sqrt{3}}\right)$	$\pm\frac{1}{\sqrt{3}}$	> 0	> 0
Case 5				
Saddle(optical)	$\left(\pm\cos^{-1}\left(\frac{-1}{8}\right), 0\right)$	0	> 0	> 0
	$\left(\pm\frac{1}{2}\cos^{-1}\left(\frac{-1}{8}\right), \frac{\pm\sqrt{3}}{2}\cos^{-1}\left(\frac{-1}{8}\right)\right)$	$\pm\sqrt{3}$	> 0	> 0

3.4.1 Cases 1 at global minima, and Case 4 at Dirac points

At order $\mathcal{O}(\varepsilon e^{i\theta})$, we consider Case 1 , which correspond to the global minimum at $(k,l) = (0,0)$, where $\omega = \Omega$. Similarly, the Dirac point $(k,l) = \left(\frac{2\pi}{3}, 0\right)$ yields $\omega = \sqrt{\Omega^2 + 4.5\rho}$. For clarity, we perform calculations explicitly for $(k,l) = (0,0)$, noting that the Dirac point case leads to similar results.

The $\mathcal{O}(\varepsilon^2 e^{i\theta})$ harmonic terms

From the asymptotic expansion, we obtain

$$\mathbf{M}\begin{pmatrix} G_1 \\ Q_1 \end{pmatrix} = \begin{pmatrix} A_1 \\ B_1 \end{pmatrix} \quad \text{leading to} \quad \mathbf{0} = \begin{pmatrix} A_1 \\ B_1 \end{pmatrix}, \tag{3.4.1}$$

where A_1 and B_1 are defined in equations (3.3.20)–(3.3.21). Using the substitution $P = CF$ with, we obtain

$$0 = -2i\omega(F_Z U + F_W V), \tag{3.4.2}$$

$$0 = -2i\omega C(F_Z U + F_W V). \tag{3.4.3}$$

These equations imply $U = V = 0$, while C remains undetermined. Consequently, the solution is $(G_1, Q_1)^T = (0,0)$.

The $\mathcal{O}(\varepsilon^3 e^{i\theta})$ harmonic terms at the global minimum

At third order, and under the simplification $\eta = \zeta = 0$, the asymptotic equations become

$$\mathbf{M}\begin{pmatrix} H_1 \\ R_1 \end{pmatrix} = \begin{pmatrix} A_2 \\ B_2 \end{pmatrix}, \tag{3.4.4}$$

where $\mathbf{M} = \mathbf{0}$ as defined in (3.3.5), and the right-hand side is

$$A_2 = 2i\omega F_T - \lambda\left(3|F|^2F + 2|P|^2F + \bar{F}P^2\right) + \frac{\rho}{2}(9F_{ZZ} + 3F_{WW}) + 3P_{ZW}, \tag{3.4.5}$$

$$B_2 = 2i\omega P_T - \lambda\left(3|P|^2P + 2|F|^2P + \bar{P}F^2\right) + \frac{3\rho}{2}(P_{ZZ} + 3P_{WW}) + 3F_{ZW}. \tag{3.4.6}$$

For this specific case, no choice of C with $P = CF$ allows the system to reduce to a single NLS equation for F.

3.5 Discussion

In this chapter, we applied asymptotic analysis to investigate breather modes in a mechanical triangular lattice shown in Figure 3.1, incorporating a symmetric on-site potential and NNI. We began by deriving the equations of motion for the lattice, and then applied the method of multiple scales to reduce the governing equations to a NLS equation, as shown in equation (3.3.45). We subsequently determined the focusing condition (3.3.47) and the ellipticity condition (3.3.46) that enables discrete breather solutions in the triangular lattice.

The motivation for this work was to extend the asymptotic framework used for square mechanical lattices to a 2D triangular configuration, following the methodology of Wattis *et al.* [26]. The ansatz used in our analysis is structurally similar to that employed by Butt *et al.* [23, 24], who examined square and triangular electrical lattices and derived 2D cubic NLS equations. Comparable results were also obtained by Wattis *et al.* for mechanical square lattices, where an NLS equation similar in form to our equations (3.3.45).

In Section 3.3.1, we examined the linear dispersion relation, which revealed two distinct branches: optical and acoustic. These branches intersect at Dirac points, as detailed in Table 3.1. The relative amplitude between the two com-

ponents F and P was determined via the relation $P = CF$, with C plotted across wavevector space in Figure 3.6. In certain cases, however, C was found to be undefined, indicating singular behaviour.

Section 3.4 focused on simplifying the system by setting $\zeta = 0$ and $\eta = 0$. This allowed us to explore the behaviour of the system at specific special points, again as listed in Table 3.1, and to summarise stationary breather cases in Table 3.2.

We identified stationary breather solutions in mechanical triangular lattices under these simplified conditions. Our approach contrasts with that of Yi *et al.* [71], who also considered a triangular (hexagonal) lattice, but reduced their analysis to three chains only ($n = 0, \pm 1$) using a simplified multiple-scale expansion. While they did not perform asymptotic analysis across the entire lattice as in our study, their numerical simulations confirmed the existence of long-lived moving breathers.

Marin *et al.* [52] were among to point out that hexagonal lattices are capable of supporting breather solutions. Similar conclusions were later drawn by Bajars *et al.* [72], who investigated a symmetric hexagonal lattice with Lennard-Jones and on-site potentials; their numerical results also supported the existence of long-lived breathers.

The findings of this chapter are valid for systems with symmetric interactions and a nonlinear on-site potential (i.e., with $\zeta = 0, \eta = 0$). This analysis may also be extended to the study of mechanical hexagonal lattices often referred to as honeycomb lattices which will be addressed in the following chapters.

Chapter 4

Breather modes in mechanical honeycomb lattice

In this chapter, we present results on a 2D mechanical honeycomb lattice, in which each node is connected to three nearest neighbours. The arrangement is such that each node is linked to either one neighbour on the left and two on the right, or vice versa, forming a honeycomb structure. We assume a quadratic NNI and a quartic and cubic onsite potential energy at each node. For the KG system, we derive four equations of motion for the displacements, based on the Hamiltonian, corresponding to two degrees of freedom at each of the two types of node. The method of multiple scales is used to obtain the governing equations, and we show that the system supports discrete breather solutions. Five distinct types of points in the dispersion relation are identified, at which stationary breather solutions may exist. A single nonlinear NLS equation is derived for the saddle cases, while a more complex coupled NLS system is found for the global maximum and minimum cases. Parts of this chapter are being prepared for publication.

4.1 Introduction

The previous chapter focused on a 2D mechanical triangular lattice, which is one form of a hexagonal lattice. Another form is the honeycomb lattice, in which each node has three connections, in contrast to the six in the triangular lattice considered in Chapter 3.

A honeycomb lattice consists of hexagonally arranged nodes and comprises two types of node: left-facing and right-facing 4.2. This structure is commonly found in systems such as graphene and in certain crystal layers (e.g., mica).

In this chapter, we apply analytical methods to obtain approximate solutions for breather modes in a 2D symmetric mechanical honeycomb lattice. We restrict our attention to small-amplitude breathers with slowly varying envelopes. Our aim is to investigate how the geometry of the honeycomb lattice influences the properties of discrete breathers.

To this end, we follow an analytical procedure similar to that used in Chapter 3. The analysis of the honeycomb lattice is expected to be more complex, potentially resulting in governing equations that are less straightforward than those found in the triangular lattice case.

The outline of the chapter is as follows. In Section 4.2, we derive the equations of motion and present the Hamiltonian of the system. In Section 4.3, we apply an asymptotic expansion to the equations of motion and derive the system's dispersion relation, identifying special wave number cases, including Dirac points. In Sections 4.4 to 4.7, we investigate the system under different cases, some of which yield complex coupled NLS equations. In Section 4.6, we derive a 2D NLS equation. Finally, Section 4.8 concludes the chapter with a summary and discussion of the results.

4.2 Derivation of model equations

In this section, we derive the mechanical model equations of a symmetric honeycomb lattice composed of interconnected particles, as illustrated in Figure 4.1, with the unit cell shown in Figure 4.2. In this system, each particle is connected to three nearest neighbours—either two on the left and one on the right, or vice versa.

The equations of motion for each node in the lattice plane are derived based on this configuration. When the displacements are denoted by $(u_{m,n}(t), v_{m,n}(t))$, the node is connected to one neighbour on the left and two on the right. Conversely, for $(\hat{u}_{m,n}(t), \hat{v}_{m,n}(t))$, the configuration is reversed, with two neighbours on the left and one on the right.

We consider a 2D Hamiltonian $H(u_{m,n}, v_{m,n}, \hat{u}_{m,n}, \hat{v}_{m,n})$, assuming only linear NNIs and neglecting nonlinear contributions in the coupling. To derive the equations of motion for the honeycomb lattice, we follow a similar analytical procedure to that outlined in Chapter 3.

We compute the potential energy associated with particle separations $\phi_{m,n,*}$, where $* = h, d, e$, representing horizontal and two types of diagonal interactions respectively. The subscript h corresponds to the horizontal direction, i.e. in line with m-axis; the subscript d corresponds to the northeast–southwest (upper-right to lower-left) direction, i.e. along the line $n = m$; and the subscript e corresponds to the northwest–southeast (upper-left to lower-right) direction, i.e. along the line $n = -m$. Here, Φ denotes the distance between interacting particles. The corresponding distances for the left-facing and right-facing nodes are denoted by $\phi_{m,n,*}$ and $\hat{\phi}_{m,n,*}$, respectively.

The general form of the potential energy is given by

$$V(\phi) = \frac{1}{2}\rho\phi^2 + \frac{1}{3}a\phi^3 + \frac{1}{4}b\phi^4, \qquad V'(\phi) = \rho\phi + a\phi^2 + b\phi^3. \tag{4.2.1}$$

In the case $(a = b = 0)$, this simplifies to $V'(\phi) = \rho\phi$. The corresponding

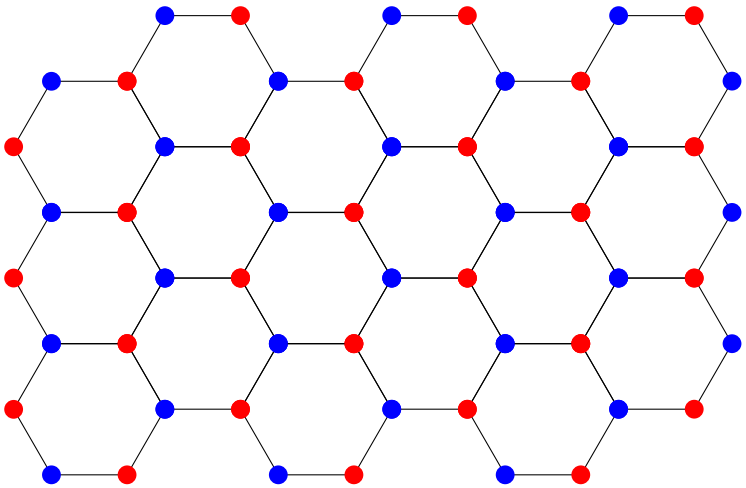

Figure 4.1: Illustration of a mechanical honeycomb lattice in which each particle is connected to three nearest neighbours, arranged either as two on the left and one on the right, or vice versa. These configurations are highlighted in blue and red, respectively.

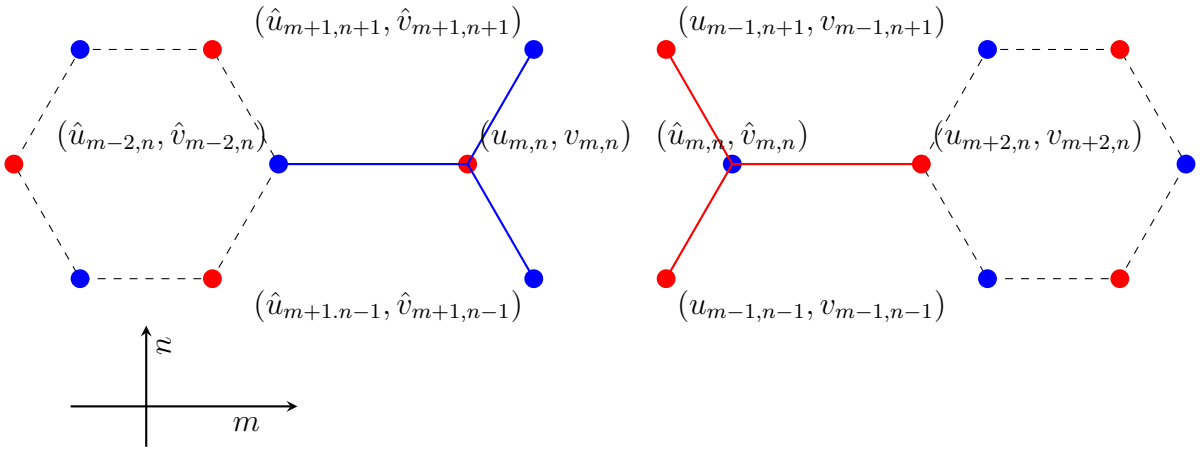

Figure 4.2: A mechanical honeycomb lattice cell illustrates two distinct arrangements of nearest-neighbour connections, highlighted in blue and red.

left-facing node interaction energies in each direction ($* = h, d, e$) are given as

$$V_{\phi_{m,n,h}} = \frac{\rho}{2}(u_{m+2,n} - \hat{u}_{m,n})^2, \qquad V_{\hat{\phi}_{m,n,h}} = \frac{\rho}{2}(\hat{u}_{m-2,n} - u_{m,n})^2, \tag{4.2.2}$$

$$V_{\phi_{m,n,d}} = \frac{\rho}{8}(\hat{u}_{m+1,n+1} - u_{m,n})^2 + \frac{3\rho}{8}(\hat{v}_{m+1,n+1} - v_{m,n})^2 + \frac{\sqrt{3}\rho}{4}(\hat{u}_{m+1,n+1} - \hat{u}_{m+1,n-1})(\hat{v}_{m+1,n+1} - \hat{v}_{m+1,n-1}), \tag{4.2.3}$$

$$V_{\hat{\phi}_{m,n,e}} = \frac{\rho}{8}(u_{m-1,n+1} - \hat{u}_{m,n})^2 + \frac{3\rho}{8}(v_{m-1,n+1} - \hat{v}_{m,n})^2 - \frac{\sqrt{3}\rho}{4}(u_{m-1,n+1} - u_{m-1,n-1})(v_{m-1,n+1} - v_{m-1,n-1}). \tag{4.2.4}$$

The on-site potential energies are defined as

$$V_o(u_{m,n}, v_{m,n}) = \frac{1}{2}\Omega^2(u_{m,n}^2 + v_{m,n}^2) + \frac{1}{4}\lambda(u_{m,n}^2 + v_{m,n}^2)^2 + \frac{1}{3}\eta u_{m,n}(u_{m,n}^2 - 3v_{m,n}^2) + \frac{1}{3}\zeta v_{m,n}(v_{m,n}^2 - 3u_{m,n}^2), \quad (4.2.5)$$

$$\hat{V}_o(\hat{u}_{m,n}, \hat{v}_{m,n}) = \frac{1}{2}\Omega^2(\hat{u}_{m,n}^2 + \hat{v}_{m,n}^2) + \frac{1}{4}\lambda(\hat{u}_{m,n}^2 + \hat{v}_{m,n}^2)^2 - \frac{1}{3}\eta\hat{u}_{m,n}(\hat{u}_{m,n}^2 - 3\hat{v}_{m,n}^2) - \frac{1}{3}\zeta\hat{v}_{m,n}(\hat{v}_{m,n}^2 - 3\hat{u}_{m,n}^2). \quad (4.2.6)$$

The total Hamiltonian of the mechanical honeycomb system is therefore given by

$$H(u, v, \hat{u}, \hat{v}) = \sum_{m,n}\left\{\frac{M}{2}\left(\frac{du_{m,n}}{dt}\right)^2 + \frac{M}{2}\left(\frac{dv_{m,n}}{dt}\right)^2 + \frac{M}{2}\left(\frac{d\hat{u}_{m,n}}{dt}\right)^2 + \frac{M}{2}\left(\frac{d\hat{v}_{m,n}}{dt}\right)^2 + V_o(u_{m,n}, v_{m,n}) + \hat{V}_o(\hat{u}_{m,n}, \hat{v}_{m,n}) + V(\phi_{m,n,h}) + V(\phi_{m,n,d}) + V(\phi_{m,n,e})\right\}. \quad (4.2.7)$$

The corresponding equations of motion are

$$M\frac{d^2u_{m,n}}{dt^2} = -\Omega^2 u_{m,n} - \lambda u_{m,n}(u_{m,n}^2 + v_{m,n}^2) - \eta u_{m,n}^2 + \eta v_{m,n}^2 + 2\zeta u_{m,n}v_{m,n} + \rho(\hat{u}_{m-2,n} - u_{m,n}) + \frac{\rho}{4}(\hat{u}_{m+1,n+1} - 2u_{m,n} + \hat{u}_{m+1,n-1}) + \frac{\sqrt{3}\rho}{4}(\hat{v}_{m+1,n+1} - \hat{v}_{m+1,n-1}), \quad (4.2.8)$$

$$M\frac{d^2v_{m,n}}{dt^2} = -\Omega^2 v_{m,n} - \lambda v_{m,n}(u_{m,n}^2 + v_{m,n}^2) + 2\eta u_{m,n}v_{m,n} - \zeta v_{m,n}^2 + \zeta u_{m,n}^2 + \frac{3\rho}{4}(\hat{v}_{m+1,n+1} - 2v_{m,n} + \hat{v}_{m+1,n-1}) + \frac{\sqrt{3}\rho}{4}(\hat{u}_{m+1,n+1} - \hat{u}_{m+1,n-1}), \quad (4.2.9)$$

$$
\begin{aligned}
M\frac{d^2\hat{u}_{m,n}}{dt^2} = & -\Omega^2\hat{u}_{m,n} - \lambda\hat{u}_{m,n}(\hat{u}_{m,n}^2 + \hat{v}_{m,n}^2) + \eta\hat{u}_{m,n}^2 - \eta\hat{v}_{m,n}^2 \\
& - 2\zeta\hat{u}_{m,n}\hat{v}_{m,n} + \rho(u_{m+2,n} - \hat{u}_{m,n}) \\
& + \frac{\rho}{4}(u_{m-1,n+1} - 2\hat{u}_{m,n} + u_{m-1,n-1}) \\
& - \frac{\sqrt{3}\rho}{4}(v_{m-1,n+1} - v_{m-1,n-1}), \qquad (4.2.10) \\
M\frac{d^2\hat{v}_{m,n}}{dt^2} = & -\Omega^2\hat{v}_{m,n} - \lambda\hat{v}_{m,n}(\hat{u}_{m,n}^2 + \hat{v}_{m,n}^2) - 2\eta\hat{v}_{m,n}\hat{u}_{m,n} \\
& + \zeta\hat{v}_{m,n}^2 - \zeta\hat{u}_{m,n}^2 + \frac{3\rho}{4}(v_{m-1,n+1} - 2\hat{v}_{m,n} + v_{m-1,n-1}) \\
& - \frac{\sqrt{3}\rho}{4}(u_{m-1,n+1} - u_{m-1,n-1}). \qquad (4.2.11)
\end{aligned}
$$

Here, M represents the mass, which may be set to unity ($M = 1$) to simplify further analysis.

4.3 Asymptotic analysis

4.3.1 Preliminaries

To derive an asymptotic solution to the equations of motion, we introduce a small parameter $\varepsilon \ll 1$, where ε is a dimensionless quantity used to systematically expand the solution, capturing the system's slow spatial and temporal variations. We define the scaled spatial and temporal variables as $x = \varepsilon m$, $y = \varepsilon n\sqrt{3}$, $\tau = \varepsilon t$, and $T = \varepsilon^2 t$.

We follow the multiple scales approach described in Chapter 3, using the method outlined by Bender and Orszag [20]. To characterise the phase of linear waves, we define $\theta = km + l\sqrt{3}n + \omega(k,l)t$, and express the leading-order solution (ansatz) in terms of slowly varying amplitude envelopes $F(x,y,\tau,T)$, $P(x,y,\tau,T)$, $\hat{F}(x,y,\tau,T)$, and $\hat{P}(x,y,\tau,T)$ as follows

$$
\begin{aligned}
u_{m,n}(t) &= \varepsilon e^{i\theta} F(x,y,\tau,T) + \varepsilon^2 \left[e^{2i\theta} G_2 + e^{i\theta} G_1 + G_0 \right] \\
&\quad + \varepsilon^3 \left[e^{3i\theta} H_3 + e^{2i\theta} H_2 + e^{i\theta} H_1 + H_0 \right] + \cdots + \text{c.c.}, \qquad (4.3.1) \\
v_{m,n}(t) &= \varepsilon e^{i\theta} P(x,y,\tau,T) + \varepsilon^2 \left[e^{2i\theta} Q_2 + e^{i\theta} Q_1 + Q_0 \right] \\
&\quad + \varepsilon^3 \left[e^{3i\theta} R_3 + e^{2i\theta} R_2 + e^{i\theta} R_1 + R_0 \right] + \cdots + \text{c.c.}, \qquad (4.3.2) \\
\hat{u}_{m,n}(t) &= \varepsilon e^{i\theta} \hat{F}(x,y,\tau,T) + \varepsilon^2 \left[e^{2i\theta} \hat{G}_2 + e^{i\theta} \hat{G}_1 + \hat{G}_0 \right] \\
&\quad + \varepsilon^3 \left[e^{3i\theta} \hat{H}_3 + e^{2i\theta} \hat{H}_2 + e^{i\theta} \hat{H}_1 + \hat{H}_0 \right] + \cdots + \text{c.c.}, \qquad (4.3.3) \\
\hat{v}_{m,n}(t) &= \varepsilon e^{i\theta} \hat{P}(x,y,\tau,T) + \varepsilon^2 \left[e^{2i\theta} \hat{Q}_2 + e^{i\theta} \hat{Q}_1 + \hat{Q}_0 \right] \\
&\quad + \varepsilon^3 \left[e^{3i\theta} \hat{R}_3 + e^{2i\theta} \hat{R}_2 + e^{i\theta} \hat{R}_1 + \hat{R}_0 \right] + \cdots + \text{c.c.}, \qquad (4.3.4)
\end{aligned}
$$

Here, $G_j, Q_j, \hat{G}_j, \hat{Q}_j$ represent second-order corrections in ε, and $H_j, R_j, \hat{H}_j, \hat{R}_j$ denote third-order corrections for $j = 0, 1, 2$. All functions depend on (x, y, τ, T). As in Chapter 3, we adopt the simplifying assumption $\eta = 0, \zeta = 0$ throughout this analysis. To determine the leading-order envelopes $F, P, \hat{F}, \hat{P}$, we begin by considering the linear dispersion relation at order $\mathcal{O}(\varepsilon e^{i\theta})$.

4.3.2 The dispersion relation $\mathcal{O}(\varepsilon e^{i\theta})$ terms

At $\mathcal{O}(\varepsilon e^{i\theta})$, we substitute the asymptotic ansatz expressions (4.3.1)–(4.3.4) into the equations of motion (4.2.8)–(4.2.11). We then collect terms at order $\mathcal{O}(\varepsilon e^{i\theta})$, and the resulting system describes the linear wave propagation in the mechanical honeycomb lattice as

$$
\mathbf{M}_1 \begin{pmatrix} F \\ P \\ \hat{F} \\ \hat{P} \end{pmatrix} = \begin{pmatrix} 0 \\ 0 \\ 0 \\ 0 \end{pmatrix}, \qquad (4.3.5)
$$

where the matrix $\mathbf{M}_1$ is defined as

$$\mathbf{M}_1 = \begin{pmatrix} \Omega^2 - \omega^2 + \frac{3\rho}{2} & 0 & -\rho e^{-2ik} - \frac{\rho}{4}\beta & -\frac{\sqrt{3}\rho}{4}\hat{\beta} \\ 0 & \Omega^2 - \omega^2 + \frac{3\rho}{2} & -\frac{\sqrt{3}\rho}{4}\hat{\beta} & -\frac{3\rho}{4}\beta \\ -\rho e^{2ik} - \frac{\rho}{4}\beta^* & \frac{\sqrt{3}\rho}{4}\hat{\beta}^* & \Omega^2 - \omega^2 + \frac{3\rho}{2} & 0 \\ \frac{\sqrt{3}\rho}{4}\hat{\beta}^* & -\frac{3\rho}{4}\beta^* & 0 & \Omega^2 - \omega^2 + \frac{3\rho}{2} \end{pmatrix}, \quad (4.3.6)$$

with $\beta = 2e^{ik}\cos(l\sqrt{3})$, $\hat{\beta} = 2ie^{ik}\sin(l\sqrt{3})$, and * denoting complex conjugation.

The matrix $\mathbf{M}_1$, introduced in the dispersion relation is *Hermitian*. This means that it is equal to its own Hermitian conjugate, denoted by $\mathbf{M}_1^\dagger = \mathbf{M}_1$. The Hermitian conjugate of a matrix is obtained by taking the complex conjugate of each entry and then transposing the matrix. This structure leads to several important mathematical properties. First, all eigenvalues δ_i of the Hermitian matrix $\mathbf{M}_1$ are real involving wave frequencies, as these must be real-valued. Second, the eigenvectors $\mathbf{v}_i$ associated with distinct eigenvalues are orthogonal, satisfying $\langle \mathbf{v}_i, \mathbf{v}_j \rangle = 0$ for $i \neq j$, where $\langle \cdot, \cdot \rangle$ denotes the standard inner product. Finally, each eigenvector satisfies the eigenvalue relation $\mathbf{M}_1\mathbf{v}_j = \delta_j\mathbf{v}_j$, meaning that the matrix $\mathbf{M}_1$ acts by scaling the eigenvector $\mathbf{v}_j$ by its corresponding eigenvalue δ_j. These properties will be used later to simplify the system and isolate independent wave modes corresponding to each branch of the dispersion relation.

To obtain non-trivial solutions for $F, P, \hat{F}, \hat{P}$, we require the determinant of $\mathbf{M}_1$ to vanish

$$\begin{aligned} \det(\mathbf{M}_1) = -3\left(\frac{\Omega^2}{3} - \frac{\omega^2}{3} + \rho\right)\left(\Omega^2 - \omega^2\right)\Big[\cos^2(l\sqrt{3})\rho^2 + \cos(l\sqrt{3})\cos(3k)\rho^2 \\ - 2\left(\frac{\Omega^2}{2} - \frac{\omega^2}{2} + \rho\right)\left(\Omega^2 - \omega^2 + \rho\right)\Big] = 0. \end{aligned} \quad (4.3.7)$$

Solving this yields four distinct branches of the linear spectrum

$$\omega_1^2 = \Omega^2, \qquad \omega_2^2 = \Omega^2 + 3\rho, \tag{4.3.8}$$

$$\omega_{3ac}^2 = \Omega^2 + \frac{3\rho}{2} - \frac{1}{2}\sqrt{4\cos^2(l\sqrt{3})\rho^2 + 4\cos(l\sqrt{3})\cos(3k)\rho^2 + \rho^2}, \tag{4.3.9}$$

$$\omega_{4op}^2 = \Omega^2 + \frac{3\rho}{2} + \frac{1}{2}\sqrt{4\cos^2(l\sqrt{3})\rho^2 + 4\cos(l\sqrt{3})\cos(3k)\rho^2 + \rho^2}. \tag{4.3.10}$$

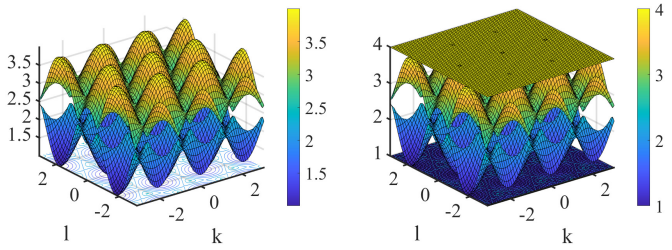

(a) (b)

Figure 4.3: Combined dispersion surfaces of all four branches ω_1, ω_2, ω_3, and ω_4. The left panel shows ω_3 and ω_4, while the right panel displays all four branches. Parameters: $\rho = \Omega = 1$; $-\pi \leq k, l \leq \pi$.

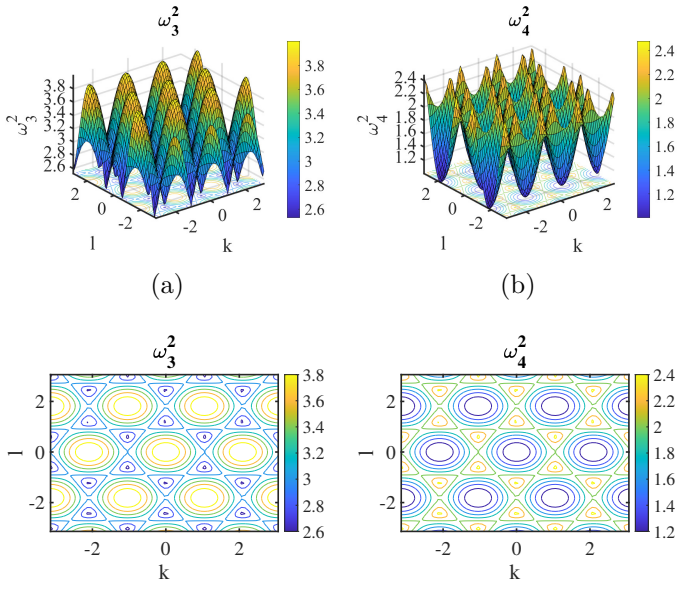

(a) (b)

(c) (d)

Figure 4.4: Dispersion surfaces of ω^2 for the acoustic ω_3^2 and optical ω_4^2 branches. The top panels show surface plots. The bottom panels display the corresponding contour plots. Parameters: $\rho = \Omega = 1$; $-\pi \leq k, l \leq \pi$.

Thus, the linear spectrum consists of four branches: ω_1, ω_2, ω_3, and ω_4. The two flat bands, ω_1 and ω_2, are shown in Figure 4.3(b). The branch ω_3 represents

the acoustic band, while ω_4, corresponding to the optical band, is illustrated in Figure 4.4.

We expect to find DB solutions within both the acoustic and optical branches of the dispersion relation. These DB frequencies may possess higher harmonics that lie beyond the linear spectrum. Since we have four distinct expressions for the dispersion relation $\omega_j(k,l)$, for $j = 1,2,3,4$, we can compute the corresponding horizontal and vertical group velocities as the partial derivatives with respect to the wave numbers $U_j = \frac{\partial \omega_j}{\partial k}, \quad V_j = \frac{\partial \omega_j}{\partial l}$. In particular, the two flat bands ω_1 and ω_2 exhibit zero group velocity in all directions $U_1 = U_2 = 0, \quad V_1 = V_2 = 0$, indicating that waves in these bands do not propagate.

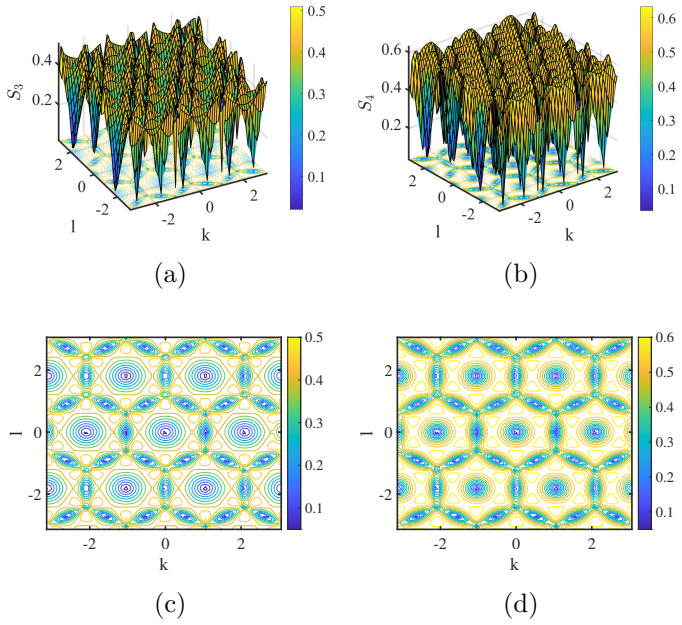

Figure 4.5: Total wave speeds $S_j = \sqrt{U_j^2 + V_j^2}$ for $j = 3,4$, computed over $-\pi \leq k,l \leq \pi$ with $\rho = \Omega = 1$. Panels (a) and (b) show surface plots of S_3 and S_4; panels (c) and (d) display the corresponding contour plots.

The symmetry of the honeycomb lattice is further illustrated in Figure 4.5, where we plot the total speed for the acoustic and optical bands given by

$$S_3 = \sqrt{U_3^2 + V_3^2}, \quad S_4 = \sqrt{U_4^2 + V_4^2}.$$

Later, the quantities U and V are defined at specific points in wavevector space (k, l).

Table 4.1: Summary of special points in wave vector space (k, l) which will be investigated in more detail later; Case 1: global minimum , Case 2: global maximum, Case 3: Dirac points, Case 4: saddle acoustic, and Case 5: saddle optical.

(k,l)	ω	ω
a=$(0,0)$,b=$(2\pi/3,0)$,c=$(-2\pi/3,0)$ d=$\left(\frac{\pi}{3},\frac{\pi}{\sqrt{3}}\right)$ & e=$\left(-\frac{\pi}{3},\frac{\pi}{\sqrt{3}}\right)$ & f=$\left(\frac{\pi}{3},-\frac{\pi}{\sqrt{3}}\right)$ & g=$\left(-\frac{\pi}{3},-\frac{\pi}{\sqrt{3}}\right)$	Case 1: $\omega_1 = \Omega$	Case 2: $\omega_2 = \sqrt{\Omega^2+3\rho}$
a=$\left(\frac{\pi}{3},\frac{\pi}{3\sqrt{3}}\right)$ & b=$\left(-\frac{\pi}{3},\frac{\pi}{3\sqrt{3}}\right)$ & c=$\left(\frac{\pi}{3},-\frac{\pi}{3\sqrt{3}}\right)$ & d=$\left(-\frac{\pi}{3},-\frac{\pi}{3\sqrt{3}}\right)$ e=$\left(0,\frac{2\pi}{3\sqrt{3}}\right)$ & f=$\left(0,\frac{-2\pi}{3\sqrt{3}}\right)$	Case 3: $\omega = \sqrt{\Omega^2+3\rho/2}$	
a=$\left(\frac{\pi}{6},\frac{\pi}{2\sqrt{3}}\right)$ & b=$\left(-\frac{\pi}{6},\frac{\pi}{2\sqrt{3}}\right)$ & c=$\left(\frac{\pi}{6},-\frac{\pi}{6\sqrt{3}}\right)$ & d=$\left(-\frac{\pi}{6},-\frac{\pi}{2\sqrt{3}}\right)$ e=$\left(\frac{\pi}{3},0\right)$ & f=$\left(-\frac{\pi}{3},0\right)$ g=$\left(0,\frac{\pi}{\sqrt{3}}\right)$ & h=$\left(0,\frac{-\pi}{\sqrt{3}}\right)$	Case 4: $\omega_3 = \sqrt{\Omega^2+\rho}$	Case 5: $\omega_4 = \sqrt{\Omega^2+2\rho}$

To guide our subsequent nonlinear analysis, we identify specific wave number pairs (k, l) where stationary breather solutions are expected to arise. These points correspond to special locations in Figure 4.4, such as global extrema, Dirac points, and saddle points of the dispersion surfaces. Each of these configurations is associated with either the acoustic or optical branches of the linear spectrum and represents a significant location where velocity vanishes or the band structure is critical.

Table 4.1 summarises these special points, grouped into five representative cases: Case 1 (global minimum), Case 2 (global maximum), Case 3 (Dirac points), Case 4 (acoustic saddle points), and Case 5 (optical saddle points). In the remainder of this chapter, we first proceed with a general nonlinear asymptotic analysis and then investigate each of these cases in detail. Our

primary interest lies in stationary breather-type solutions, which are often associated with such critical points. These discrete breathers may emerge either above the optical band or below the acoustic band and, in some cases such as the Dirac points, may also be linked to modulational instabilities.

4.3.3 The relative amplitude

At leading order, we have $\mathbf{M}_1\mathbf{v} = 0$, where $\mathbf{v} = (F, P, \hat{F}, \hat{P})^T$ lies in the null space (or kernel) of the singular matrix $\mathbf{M}_1$. The relative amplitudes of the components can therefore be expressed as

$$\begin{pmatrix} F \\ P \\ \hat{F} \\ \hat{P} \end{pmatrix} = F \begin{pmatrix} 1 \\ Ce^{i\gamma} \\ e^{i\psi} \\ \pm Ce^{i(\gamma+\psi)} \end{pmatrix}, \tag{4.3.11}$$

where $e^{i\psi}, e^{i\gamma}, e^{i(\psi+\gamma)}$ are complex phase factors determined from the kernel of $\mathbf{M}_1$.

4.3.4 Zeroth harmonic terms $\mathcal{O}(\varepsilon^2 e^0)$

At order $\mathcal{O}(\varepsilon^2 e^0)$, we collect the coefficients of the zeroth harmonic from the equations of motion (4.2.8)–(4.2.11). This yields the following relations

$$0 = -\Omega^2 \left(G_0 + G_0^*\right) - 2\eta|F|^2 + 2\eta|P|^2 + 2\zeta\left(P\bar{F} + F\bar{P}\right), \tag{4.3.12}$$

$$0 = -\Omega^2 \left(Q_0 + Q_0^*\right) - 2\eta\left(F\bar{P} + \bar{F}P\right) + 2\zeta\left(|F|^2 - |P|^2\right), \tag{4.3.13}$$

$$0 = -\Omega^2 \left(\hat{G}_0 + \hat{G}_0^*\right) + 2\eta|\hat{F}|^2 - 2\eta|\hat{P}|^2 - 2\zeta\left(\hat{P}\bar{\hat{F}} + \hat{F}\bar{\hat{P}}\right), \tag{4.3.14}$$

$$0 = -\Omega^2 \left(\hat{Q}_0 + \hat{Q}_0^*\right) + 2\eta\left(\hat{F}\bar{\hat{P}} - \bar{\hat{F}}\hat{P}\right) - 2\zeta\left(|\hat{F}|^2 - |\hat{P}|^2\right). \tag{4.3.15}$$

In this study, we assume the imaginary parts of G_0, Q_0, $\hat{G}_0$, and $\hat{Q}_0$ vanish, as they do not contribute to the $u_{m,n}$, $v_{m,n}$, $\hat{u}_{m,n}$, and $\hat{v}_{m,n}$.

$$G_0 = \frac{-2}{\Omega^2}\left(\eta|F|^2 - \eta|P|^2 - \zeta\left(P\bar{F} + F\bar{P}\right)\right), \tag{4.3.16}$$

$$Q_0 = \frac{-2}{\Omega^2}\left(\eta\left(F\bar{P} + \bar{F}P\right) - \zeta\left(|F|^2 - |P|^2\right)\right), \tag{4.3.17}$$

$$\hat{G}_0 = \frac{-2}{\Omega^2}\left(-\eta|\hat{F}|^2 + \eta|\hat{P}|^2 + \zeta\left(\hat{P}\bar{\hat{F}} + \hat{F}\bar{\hat{P}}\right)\right), \tag{4.3.18}$$

$$\hat{Q}_0 = \frac{-2}{\Omega^2}\left(-\eta\left(\hat{F}\bar{\hat{P}} - \bar{\hat{F}}\hat{P}\right) + \zeta\left(|\hat{F}|^2 - |\hat{P}|^2\right)\right). \tag{4.3.19}$$

Applying the simplifying assumption $\eta = 0, \zeta = 0$, with $\Omega \neq 0$ the above expressions reduce to

$$G_0 = 0, \qquad Q_0 = 0, \qquad \hat{G}_0 = 0, \qquad \hat{Q}_0 = 0. \tag{4.3.20}$$

These results confirm that, under the assumption $\eta = 0$ and $\zeta = 0$, the zeroth harmonic contributions vanish identically, simplifying the system at this order.

4.3.5 Second harmonic terms $\mathcal{O}(\varepsilon^2 e^{2i\theta})$

At the order $\mathcal{O}(\varepsilon^2 e^{2i\theta})$, we collect all second harmonic terms resulting from the substitution of the asymptotic ansatz (4.3.1)–(4.3.4) into the equations of motion (4.2.8)–(4.2.11). Since we assume $\eta = \zeta = 0$ throughout this chapter, the right-hand side of the system becomes zero, yields

$$\mathbf{M}_2 \begin{pmatrix} G_2 \\ Q_2 \\ \hat{G}_2 \\ \hat{Q}_2 \end{pmatrix} = \begin{pmatrix} 0 \\ 0 \\ 0 \\ 0 \end{pmatrix}, \tag{4.3.21}$$

where $\mathbf{M}_2$ is a Hermitian matrix, given explicitly by

$$\mathbf{M}_2 = \begin{pmatrix} \Omega^2 - 4\omega^2 + \frac{3\rho}{2} & 0 & -\rho e^{-4ik} - \frac{\rho}{4}\beta_1 & -\frac{\sqrt{3}\rho}{4}\hat{\beta}_1 \\ 0 & \Omega^2 - 4\omega^2 + \frac{3\rho}{2} & -\frac{\sqrt{3}\rho}{4}\hat{\beta}_1 & -\frac{3\rho}{4}\beta_1 \\ -\rho e^{4ik} - \frac{\rho}{4}\beta_1^* & \frac{\sqrt{3}\rho}{4}\hat{\beta}_1^* & \Omega^2 - 4\omega^2 + \frac{3\rho}{2} & 0 \\ \frac{\sqrt{3}\rho}{4}\hat{\beta}_1^* & -\frac{3\rho}{4}\beta_1^* & 0 & \Omega^2 - 4\omega^2 + \frac{3\rho}{2} \end{pmatrix}, \tag{4.3.22}$$

where $\beta_1 = 2e^{ik}\cos(2l\sqrt{3})$, $\hat{\beta}_1 = 2ie^{ik}\sin(2l\sqrt{3})$, and * denotes complex conjugation. If $\eta = 0, \zeta = 0$, then, the solution reduces to

$$G_2 = 0, \qquad Q_2 = 0, \qquad \hat{G}_2 = 0, \qquad \hat{Q}_2 = 0. \tag{4.3.23}$$

These results indicate that, all second harmonic contributions vanish, and the solution at this order is zero.

4.3.6 Harmonic terms at $\mathcal{O}(\varepsilon^2 e^{i\theta})$

At the order $\mathcal{O}(\varepsilon^2 e^{i\theta})$, we collect the terms corresponding from the substituted ansatz (4.3.1)–(4.3.4) into the equations of motion (4.2.8)–(4.2.11). This yields the following

$$\mathbf{M}_1 \begin{pmatrix} G_1 \\ Q_1 \\ \hat{G}_1 \\ \hat{Q}_1 \end{pmatrix} = \begin{pmatrix} A_1 \\ A_2 \\ B_1 \\ B_2 \end{pmatrix}, \tag{4.3.24}$$

where $\mathbf{M}_1$ is the same matrix defined in equation (4.3.6), and the terms A_1, A_2, B_1, and B_2 are given by

$$A_1 = -2i\omega F_\tau + \frac{\rho}{2}e^{ik}\left(\cos(lh) - 4e^{-3ik}\right)\hat{F}_x + \frac{\sqrt{3}\rho}{2}ie^{ik}\sin(lh)\hat{F}_y + \frac{\sqrt{3}\rho}{2}\left(ie^{ik}\sin(lh)\hat{P}_x + \sqrt{3}e^{ik}\cos(lh)\hat{P}_y\right), \tag{4.3.25}$$

$$A_2 = -2i\omega P_\tau + \frac{3\rho}{2}e^{ik}\cos(lh)\hat{P}_x + \frac{3\rho}{2}i\sqrt{3}e^{ik}\sin(lh)\hat{P}_y + \frac{\sqrt{3}\rho}{2}\left(ie^{ik}\sin(lh)\hat{F}_x + \sqrt{3}e^{ik}\cos(lh)\hat{F}_y\right), \tag{4.3.26}$$

$$B_1 = -2i\omega\hat{F}_\tau + \frac{\rho}{2}\left(-e^{-ik}(\cos(lh) - 4e^{3ik})F_x + i\sqrt{3}e^{-ik}\sin(lh)F_y\right) + \frac{\sqrt{3}\rho}{2}\left(ie^{-ik}\sin(lh)P_x - \sqrt{3}e^{-ik}\cos(lh)P_y\right), \tag{4.3.27}$$

$$B_2 = -2i\omega\hat{P}_\tau + \frac{3\rho}{2}\left(-e^{-ik}\cos(lh)P_x + i\sqrt{3}e^{-ik}\sin(lh)P_y\right) + \frac{\sqrt{3}\rho}{2}\left(ie^{-ik}\sin(lh)F_x - \sqrt{3}e^{-ik}\cos(lh)F_y\right). \tag{4.3.28}$$

At this stage, we have derived general expressions for the harmonic terms A_1, A_2, B_1, and B_2 at order $\mathcal{O}(\varepsilon^2 e^{i\theta})$, as given in equations (4.3.25)–(4.3.28). These expressions remain valid for arbitrary wavevector values (k, l), and will be used as input in the analysis of specific cases.

Due to the complexity of solving for $G_1, Q_1, \hat{G}_1, \hat{Q}_1$ in the general case, we postpone the full evaluation of these quantities until we consider specific special points in wavevector space in subsections 4.4 to 4.7. In the following subsections, for each special choice of (k, l), we apply the corresponding relative amplitude structure, then introduce travelling wave coordinates $Z = x - U\tau$, $W = y - V\tau$, and determine the appropriate values of U and V. This approach allows us to simplify and solve the governing equations systematically, and derive explicit formulae for the first-order corrections $G_1, Q_1, \hat{G}_1, \hat{Q}_1$ as needed.

We now proceed to compute the harmonic terms at $\mathcal{O}(\varepsilon^3 e^{i\theta})$, which will be used in conjunction with the previous results to derive the corresponding governing equations for the envelope dynamics.

4.3.7 Harmonic terms at $\mathcal{O}(\varepsilon^3 e^{i\theta})$

At this order, we substitute the ansatz (4.3.1)–(4.3.4) into the equations of motion (4.2.8)–(4.2.11) and collect terms at order $\varepsilon^3 e^{i\theta}$. As in previous sections, we continue under the simplifying assumption that $\eta = \zeta = 0$, which eliminates cubic nonlinearities from the system. This yields the following

$$\mathbf{M}_1 \begin{pmatrix} R_1 \\ H_1 \\ \hat{R}_1 \\ \hat{H}_1 \end{pmatrix} = \begin{pmatrix} A_{31} \\ A_{32} \\ A_{33} \\ A_{34} \end{pmatrix}, \tag{4.3.29}$$

where $\mathbf{M}_1$ is defined in equation (4.3.6), and the terms $A_{31}, A_{32}, A_{33}, A_{34}$ are given below

$$\begin{aligned} A_{31} = {} & 2i\omega F_T - \lambda\left(3|F|^2F + 2|P|^2F + \bar{F}P^2\right) \\ & + \frac{\rho}{2}\left[\tfrac{1}{2}e^{ik}\left(\cos(lh) + 8e^{-3ik}\right)\hat{F}_{xx} + \tfrac{3}{2}e^{ik}\cos(lh)\hat{F}_{yy} + \sqrt{3}ie^{ik}\sin(lh)\hat{F}_{xy}\right] \\ & + \frac{\rho}{2}\left[\hat{G}_{1x}e^{ik}\left(\cos(lh) - 4e^{-3ik}\right) + \sqrt{3}ie^{ik}\sin(lh)\hat{G}_{1y}\right] \\ & + \frac{\sqrt{3}\rho}{2}\left[\tfrac{1}{2}ie^{ik}\sin(lh)\hat{P}_{xx} + \tfrac{3}{2}ie^{ik}\sin(lh)\hat{P}_{yy} + \sqrt{3}e^{ik}\cos(lh)\hat{P}_{xy}\right. \\ & \left. + ie^{ik}\sin(lh)\hat{Q}_{1x} + \sqrt{3}e^{ik}\cos(lh)\hat{Q}_{1y}\right], \end{aligned} \tag{4.3.30}$$

$$\begin{aligned} A_{32} = {} & 2i\omega P_T - \lambda\left(3|P|^2P + 2|F|^2P + \bar{P}F^2\right) \\ & + \frac{3\rho}{2}\left[\tfrac{1}{2}e^{ik}\cos(lh)\hat{P}_{xx} + \tfrac{3}{2}e^{ik}\cos(lh)\hat{P}_{yy} + \sqrt{3}ie^{ik}\sin(lh)\hat{P}_{xy}\right. \\ & \left. + \sqrt{3}ie^{ik}\sin(lh)\hat{Q}_{1y} + e^{ik}\cos(lh)\hat{Q}_{1x}\right] \\ & + \frac{\sqrt{3}\rho}{2}\left[\tfrac{1}{2}ie^{ik}\sin(lh)\hat{F}_{xx} + \tfrac{3}{2}ie^{ik}\sin(lh)\hat{F}_{yy} + \sqrt{3}e^{ik}\cos(lh)\hat{F}_{xy}\right. \\ & \left. + ie^{ik}\sin(lh)\hat{G}_{1x} + \sqrt{3}e^{ik}\cos(lh)\hat{G}_{1y}\right], \end{aligned} \tag{4.3.31}$$

$$
\begin{aligned}
A_{33} = {} & 2i\omega\hat{F}_T - \lambda\left(3|\hat{F}|^2\hat{F} + 2|\hat{P}|^2\hat{F} + \bar{\hat{F}}\hat{P}^2\right) \\
& + \frac{\rho}{2}\left[\tfrac{1}{2}e^{-ik}\left(\cos(lh) + 8e^{3ik}\right)F_{xx} + \tfrac{3}{2}e^{-ik}\cos(lh)F_{yy} - \sqrt{3}ie^{-ik}\sin(lh)F_{xy}\right] \\
& - \frac{\rho}{2}\left[e^{ik}\left(\cos(lh) - 4e^{-3ik}\right)G_{1x} - \sqrt{3}ie^{ik}\sin(lh)G_{1y}\right] \\
& - \frac{\sqrt{3}\rho}{2}\left[\tfrac{1}{2}ie^{-ik}\sin(lh)P_{xx} + \tfrac{3}{2}ie^{-ik}\sin(lh)P_{yy} - \sqrt{3}e^{-ik}\cos(lh)P_{xy}\right. \\
& \left. -ie^{-ik}\sin(lh)Q_{1x} + \sqrt{3}e^{-ik}\cos(lh)Q_{1y}\right], \qquad (4.3.32)
\end{aligned}
$$

$$
\begin{aligned}
A_{34} = {} & 2i\omega\hat{P}_T - \lambda\left(3|\hat{P}|^2\hat{P} + 2|\hat{F}|^2\hat{P} + \bar{\hat{P}}\hat{F}^2\right) \\
& + \frac{3\rho}{2}\left[\tfrac{1}{2}e^{-ik}\cos(lh)P_{xx} + \tfrac{3}{2}e^{-ik}\cos(lh)P_{yy} - \sqrt{3}ie^{-ik}\sin(lh)P_{xy}\right. \\
& \left. +\sqrt{3}ie^{-ik}\sin(lh)Q_{1y} - e^{-ik}\cos(lh)Q_{1x}\right] \\
& - \frac{\sqrt{3}\rho}{2}\left[\tfrac{1}{2}ie^{-ik}\sin(lh)F_{xx} + \tfrac{3}{2}ie^{-ik}\sin(lh)F_{yy} - \sqrt{3}e^{-ik}\cos(lh)F_{xy}\right. \\
& \left. -ie^{-ik}\sin(lh)G_{1x} + \sqrt{3}e^{-ik}\cos(lh)G_{1y}\right]. \qquad (4.3.33)
\end{aligned}
$$

Following the general asymptotic analysis in Subsections 4.3.2 to 4.3.7, we now turn our attention to a detailed investigation of the five representative wave number configurations introduced in Table 4.1.

In the following sections, we apply the analytical framework produced above to each case individually. Our aim is to derive the governing nonlinear envelope equations, identify the conditions under which DBs may form, and examine their properties. The analysis proceeds by substituting the corresponding wave numbers (k, l) into the results from the dispersion relation and subsequent asymptotic expansions. It is worth noting that, for this configuration, both the zeroth harmonic terms (Subsection 4.3.4) and second harmonic terms (Subsection 4.3.5) vanish due to symmetry and the chosen simplifying assumptions.

4.4 Case 1: Global minimum

In this case, we examine the behaviour of the system at the global minimum of the dispersion relation, occurring at $(k, l) = (0, 0)$. This point corresponds to a flat band where the group velocity vanishes. We apply the asymptotic framework developed earlier to derive the associated envelope equations governing the breather dynamics if possible.

4.4.1 Harmonic terms $\mathcal{O}(\varepsilon e^{i\theta})$

In the global minimum case, we consider the wave number pair $(k, l) = (0, 0)$, for which the frequency is $\omega_1 = \Omega$.

$$\mathbf{M}_1 \begin{pmatrix} F \\ P \\ \hat{F} \\ \hat{P} \end{pmatrix} = \begin{pmatrix} 0 \\ 0 \\ 0 \\ 0 \end{pmatrix}. \tag{4.4.1}$$

The corresponding matrix $\mathbf{M}_1$ takes the form

$$\mathbf{M}_1 = \frac{3\rho}{2} \begin{pmatrix} 1 & 0 & -1 & 0 \\ 0 & 1 & 0 & -1 \\ -1 & 0 & 1 & 0 \\ 0 & -1 & 0 & 1 \end{pmatrix}, \tag{4.4.2}$$

which is singular, with a 2D kernel. The matrix has a double eigenvalue $\Lambda = 0$, with two linearly independent eigenvectors $\mathbf{n}_1 = (1, 0, 1, 0)^T$, $\mathbf{n}_2 = (0, 1, 0, 1)^T$. Therefore, the solution is spanned by

$$(F, P, \hat{F}, \hat{P})^T = F \begin{pmatrix} 1 \\ 0 \\ 1 \\ 0 \end{pmatrix} + P \begin{pmatrix} 0 \\ 1 \\ 0 \\ 1 \end{pmatrix},$$

implying that $F = \hat{F}$ and $P = \hat{P}$. Thus, F and P represent the two independent degrees of freedom at this order, and $\hat{G}_1 = -G_1, \quad \hat{Q}_1 = -Q_1$.

4.4.2 Harmonic terms $\mathcal{O}(\varepsilon^2 e^{i\theta})$

At $(k, l) = (0, 0)$, we substitute into the expressions (4.3.25) to (4.3.28) to evaluate the right-hand side vector $\mathbf{d}_0$ of the system

$$\mathbf{M}_1 \begin{pmatrix} G_1 \\ Q_1 \\ \hat{G}_1 \\ \hat{Q}_1 \end{pmatrix} = \begin{pmatrix} A_{11} \\ A_{12} \\ B_{21} \\ B_{22} \end{pmatrix} = \mathbf{d}_0, \tag{4.4.3}$$

where the components of $\mathbf{d}_0$ are

$$A_{11} = -\frac{3\rho}{2}F_x + \frac{3\rho}{2}P_y, \qquad A_{12} = \frac{3\rho}{2}P_x + \frac{3\rho}{2}F_y, \tag{4.4.4}$$

$$B_{21} = \frac{3\rho}{2}F_x - \frac{3\rho}{2}P_y, \qquad B_{22} = -\frac{3\rho}{2}P_x - \frac{3\rho}{2}F_y. \tag{4.4.5}$$

Solving the system with the singular matrix $\mathbf{M}_1$, we obtain

$$\begin{aligned} G_1 &= \frac{1}{2}(P_y - F_x), & Q_1 &= \frac{1}{2}(P_x + F_y), \\ \hat{G}_1 &= -G_1, & \hat{Q}_1 &= -Q_1. \end{aligned} \tag{4.4.6}$$

In general, at this order we find the velocities U, V; here we have $U = V = 0$, so the speed zero as well.

4.4.3 Harmonic terms $\mathcal{O}(\varepsilon^3 e^{i\theta})$

To evaluate the nonlinear correction at this order, we use the full expressions for A_{31}–A_{34} from equations (4.3.30)–(4.3.33). At the point $(k, l) = (0, 0)$, we simplify using $\hat{F} = F, \quad \hat{P} = P, \quad \hat{G}_1 = -G_1, \quad \hat{Q}_1 = -Q_1$, and the derivative

expressions from equation (4.4.6)

$$G_{1x} = \frac{1}{2}(P_{yx} - F_{xx}), \qquad G_{1y} = \frac{1}{2}(P_{yy} - F_{xy}),$$
$$Q_{1x} = \frac{1}{2}(P_{xx} + F_{yx}), \qquad Q_{1y} = \frac{1}{2}(P_{xy} + F_{yy}). \tag{4.4.7}$$

Applying the consistency conditions $\mathbf{n}_1 \cdot \mathbf{d}_0 = 0$ and $\mathbf{n}_2 \cdot \mathbf{d}_0 = 0$, where $\mathbf{n}_1 = (1, 0, 1, 0)^T$ and $\mathbf{n}_2 = (0, 1, 0, 1)^T$ are the basis vectors for the kernel of $\mathbf{M}_1$, we obtain

$$A_{31} + A_{33} = 0, \tag{4.4.8}$$

$$A_{32} + A_{34} = 0. \tag{4.4.9}$$

Substituting and simplifying using the assumptions at $(k, l) = (0, 0)$, the resulting coupled envelope equations are

$$-4i\omega F_T - 2\lambda\left(3|F|^2F + 2|P|^2F + \bar{F}P^2\right) + \frac{3\rho}{2}F_{xx} = 0, \tag{4.4.10}$$

$$-4i\omega P_T - 2\lambda\left(3|P|^2P + 2|F|^2P + \bar{P}F^2\right) + \frac{3\rho}{2}P_{yy} = 0. \tag{4.4.11}$$

This coupled system of nonlinear NLS equations governs the evolution of the slowly varying envelope functions $F(x, y, T)$ and $P(x, y, T)$ at the global minimum point. The resulting system cannot be reduced to a single NLS equation, owing to the coupled nature of the envelope functions F and P.

4.5 Case 2: Global maximum

In this section, we analyse the system at the global maximum of the dispersion relation, located at $(k, l) = (0, 0)$ with frequency $\omega_2 = \sqrt{\Omega^2 + 3\rho}$. We follow the same asymptotic procedure outlined earlier to derive the governing equations, starting with the first harmonic terms.

4.5.1 Harmonic terms $\mathcal{O}(\varepsilon e^{i\theta})$

In the global maximum case at $(k,l)=(0,0)$, we have $\omega_2=\sqrt{\Omega^2+3\rho}$.

$$\mathbf{M}_1\begin{pmatrix}F\\P\\\hat{F}\\\hat{P}\end{pmatrix}=\begin{pmatrix}0\\0\\0\\0\end{pmatrix}. \tag{4.5.1}$$

The corresponding matrix $\mathbf{M}_1$ is

$$\mathbf{M}_1=\frac{3\rho}{2}\begin{pmatrix}-1&0&-1&0\\0&-1&0&-1\\-1&0&-1&0\\0&-1&0&-1\end{pmatrix}, \tag{4.5.2}$$

The kernel of $\mathbf{M}_1$ is spanned by the vectors

$$(F,P,\hat{F},\hat{P})^T=F\begin{pmatrix}1\\0\\-1\\0\end{pmatrix}+P\begin{pmatrix}0\\1\\0\\-1\end{pmatrix},$$

implying the relations $F=-\hat{F}$ and $P=-\hat{P}$. Additionally, at this order, we have $\hat{G}_1=G_1$ and $\hat{Q}_1=Q_1$. The vectors normal to the range of $\mathbf{M}_1$ are

$$\mathbf{n}_1=(1,0,-1,0)^T,\quad \mathbf{n}_2=(0,1,0,-1)^T.$$

4.5.2 Harmonic terms $\mathcal{O}(\varepsilon^2 e^{i\theta})$

We now solve the second-order system from Subsection 4.3.6 at the point $(k, l) = (0, 0)$, which yields

$$\mathbf{M}_1 \begin{pmatrix} G_1 \\ Q_1 \\ \hat{G}_1 \\ \hat{Q}_1 \end{pmatrix} = \begin{pmatrix} A_{11} \\ A_{12} \\ B_{21} \\ B_{22} \end{pmatrix}, \tag{4.5.3}$$

with $\mathbf{M}_1$ given in (4.5.2), and

$$A_{11} = \frac{3\rho}{2}F_x - \frac{3\rho}{2}P_y, \qquad A_{12} = -\frac{3\rho}{2}P_x - \frac{3\rho}{2}F_y, \tag{4.5.4}$$

$$B_{21} = \frac{3\rho}{2}F_x - \frac{3\rho}{2}P_y, \qquad B_{22} = -\frac{3\rho}{2}P_x - \frac{3\rho}{2}F_y. \tag{4.5.5}$$

Solving the system, we obtain

$$\begin{aligned} G_1 &= \frac{1}{2}(P_y - F_x), \qquad Q_1 = \frac{1}{2}(P_x + F_y), \\ \hat{G}_1 &= G_1, \qquad \hat{Q}_1 = Q_1. \end{aligned} \tag{4.5.6}$$

At this order, we typically determine the group velocity components U, V; however, in this case we have $U = V = 0$, confirming that the solution is stationary.

4.5.3 Harmonic terms $\mathcal{O}(\varepsilon^3 e^{i\theta})$

At this order, we again apply the system from Subsection 4.3.7 at the point $(k, l) = (0, 0)$, given by

$$\mathbf{M}_1 \begin{pmatrix} H_1 \\ R_1 \\ \hat{H}_1 \\ \hat{R}_1 \end{pmatrix} = \begin{pmatrix} A_{31} \\ A_{32} \\ A_{33} \\ A_{34} \end{pmatrix} = \mathbf{d}_1, \tag{4.5.7}$$

where $\mathbf{M}_1$ is given in (4.5.2), and the right-hand side terms A_{31}–A_{34} are defined in 4.3.30 to 4.3.33, evaluated at $(k, l) = (0, 0)$. We substitute

$$\hat{F} = -F, \quad \hat{P} = -P, \quad \hat{G}_1 = G_1, \quad \hat{Q}_1 = Q_1,$$

along with the derivatives from (4.5.6)

$$\begin{aligned} G_{1x} &= \frac{1}{2}(P_{yx} - F_{xx}), \qquad & G_{1y} &= \frac{1}{2}(P_{yy} - F_{xy}), \\ Q_{1x} &= \frac{1}{2}(P_{xx} + F_{yx}), \qquad & Q_{1y} &= \frac{1}{2}(P_{xy} + F_{yy}). \end{aligned} \tag{4.5.8}$$

We apply the consistency conditions

$$\mathbf{n}_1 \cdot \mathbf{d}_1 = 0, \qquad \mathbf{n}_2 \cdot \mathbf{d}_1 = 0,$$

which yield

$$A_{31} - A_{33} = 0, \tag{4.5.9}$$

$$A_{32} - A_{34} = 0. \tag{4.5.10}$$

Substituting the terms and simplifying, we obtain the coupled nonlinear NLS equations

$$0 = 4i\omega F_T - 2\lambda\left(3|F|^2F + 2|P|^2F + \bar{F}P^2\right) - \frac{3\rho}{2}F_{xx}, \tag{4.5.11}$$

$$0 = 4i\omega P_T - 2\lambda\left(3|P|^2P + 2|F|^2P + \bar{P}F^2\right) - \frac{3\rho}{2}P_{yy}. \tag{4.5.12}$$

These equations are structurally similar to those derived in Case 1 (Sec-

tion 4.4). However, the specific symmetry $F = -\hat{F}, P = -\hat{P}$ changes the interpretation of the coupled modes. The system again remains coupled and cannot be reduced to a single NLS equation due to the independence of the F and P components.

4.6 Case 3: Dirac point

At the Dirac point $(k, l) = \left(0, \dfrac{2\pi}{3\sqrt{3}}\right)$, the dispersion relation yields a frequency of $\omega = \sqrt{\Omega^2 + \dfrac{3\rho}{2}}$. The expansion of the solution takes the form

$$\begin{pmatrix} u \\ v \\ \hat{u} \\ \hat{v} \end{pmatrix} = \varepsilon e^{i\theta} \begin{pmatrix} F \\ P \\ \hat{F} \\ \hat{P} \end{pmatrix} + \varepsilon^2 e^{i\theta} \begin{pmatrix} G_1 \\ Q_1 \\ \hat{G}_1 \\ \hat{Q}_1 \end{pmatrix} + \text{c.c.}, \tag{4.6.1}$$

where $\theta = km + l\sqrt{3}n + \omega t$ defines the phase. As in previous sections, we analyse the system at successive harmonic orders $\mathcal{O}(\varepsilon e^{i\theta})$, $\mathcal{O}(\varepsilon^2 e^{i\theta})$, and $\mathcal{O}(\varepsilon^3 e^{i\theta})$. We begin by determining the leading-order amplitudes $F, P, \hat{F}, \hat{P}$, and the second-order corrections $G_1, Q_1, \hat{G}_1, \hat{Q}_1$.

4.6.1 Harmonic terms $\mathcal{O}(\varepsilon e^{i\theta})$

At this order, we obtain a degenerate system governed by the Hermitian matrix $\mathbf{M}_1$, whose properties were discussed in Subsection 4.3.2. Specifically, Hermitian matrices possess real eigenvalues and orthogonal eigenvectors, and their kernel (null space) can be used to simplify coupled wave systems. Here,

$\mathbf{M}_1$ takes the form

$$\frac{3\rho}{4}\begin{pmatrix} 0 & 0 & -1 & -i \\ 0 & 0 & -i & 1 \\ -1 & i & 0 & 0 \\ i & 1 & 0 & 0 \end{pmatrix}\begin{pmatrix} F \\ P \\ \hat{F} \\ \hat{P} \end{pmatrix} = \begin{pmatrix} 0 \\ 0 \\ 0 \\ 0 \end{pmatrix}. \tag{4.6.2}$$

This matrix has eigenvalues $\pm\frac{3\rho}{2}, 0, 0$, indicating a doubly degenerate kernel. The corresponding null vectors are $\mathbf{r}_1 = (0, 0, -i, 1)^T, \mathbf{r}_2 = (i, 1, 0, 0)^T$. To reduce the system, we apply the framework formulated in Appendix C.1, using the decomposition

$$M_{11} = M_{22} = \mathbf{0}, \qquad M_{12} = \frac{3\rho}{4}\begin{pmatrix} -1 & -i \\ -i & 1 \end{pmatrix}, \qquad M_{21} = M_{12}^{*T}.$$

This leads to the reduced system

$$M_{12}\,\overline{\hat{\mathbf{F}}} = \mathbf{0}, \qquad M_{12}^{*T}\,\overline{\mathbf{F}} = \mathbf{0}, \tag{4.6.3}$$

where $\overline{\mathbf{F}} = (F, P)^T$ and $\overline{\hat{\mathbf{F}}} = (\hat{F}, \hat{P})^T$. Explicitly, this becomes

$$\begin{pmatrix} -1 & -i \\ -i & 1 \end{pmatrix}\begin{pmatrix} \hat{F} \\ \hat{P} \end{pmatrix} = \begin{pmatrix} 0 \\ 0 \end{pmatrix}, \qquad \begin{pmatrix} -1 & i \\ i & 1 \end{pmatrix}\begin{pmatrix} F \\ P \end{pmatrix} = \begin{pmatrix} 0 \\ 0 \end{pmatrix}.$$

It is important to note that both M_{12} and M_{21} are singular, but only singly degenerate. Solving these equations yields the relative amplitudes

$$P = -iF, \qquad \hat{P} = i\hat{F},$$

so the relative amplitude can be expressed as

$$\begin{pmatrix} F \\ P \end{pmatrix} = F \begin{pmatrix} 1 \\ -i \end{pmatrix}, \qquad \begin{pmatrix} \hat{F} \\ \hat{P} \end{pmatrix} = \hat{F} \begin{pmatrix} 1 \\ i \end{pmatrix}. \tag{4.6.4}$$

The corresponding normal vectors to the ranges of M_{12} and M_{21} are their Hermitian adjoints

$$\mathbf{n}_1^* = (1, i)^T, \qquad \mathbf{n}_2^* = (1, -i)^T. \tag{4.6.5}$$

These satisfy

$$\langle \mathbf{n}_1^*, \mathbf{r}_1 \rangle = 0, \qquad \langle \mathbf{n}_2^*, \mathbf{r}_2 \rangle = 0,$$

confirming the orthogonality of left and right nullspaces, as guaranteed by the Hermitian structure of $\mathbf{M}_1$, discussed earlier in Subsection 4.3.2.

4.6.2 Harmonic terms $\mathcal{O}(\varepsilon^2 e^{i\theta})$

We continue our analysis at the Dirac point $(k, l) = \left(0, \dfrac{2\pi}{3\sqrt{3}}\right)$, for which the corresponding frequency is given by $\omega = \sqrt{\Omega + \frac{3\rho}{2}}$. At this point, the governing system at $\mathcal{O}(\varepsilon^2 e^{i\theta})$ takes the form

$$\mathbf{M}_1 \begin{pmatrix} G_1 \\ Q_1 \\ \hat{G}_1 \\ \hat{Q}_1 \end{pmatrix} = \begin{pmatrix} A_1 \\ A_2 \\ B_1 \\ B_2 \end{pmatrix}, \tag{4.6.6}$$

where $\mathbf{M}_1$ is the Hermitian matrix defined in equation (4.6.2). We substitute the leading-order solution

$$\left(F, P, \hat{F}, \hat{P}\right)^T = F \begin{pmatrix} 1 \\ -i \\ 0 \\ 0 \end{pmatrix} + \hat{F} \begin{pmatrix} 0 \\ 0 \\ 1 \\ i \end{pmatrix}.$$

The right-hand side vectors A_1, A_2, B_1, B_2 are derived from equations (4.3.25)–(4.3.28) at the Dirac point. This yields

$$\begin{aligned} A_1 &= -2i\omega F_\tau + \frac{\rho}{4}(3i\hat{F}_y - 9\hat{F}_x) + \frac{3i\rho}{4}(i\hat{F}_x - \hat{F}_y), \\ A_2 &= -2\omega F_\tau + \frac{3i\rho}{4}(3i\hat{F}_y - \hat{F}_x) + \frac{3\rho}{4}(i\hat{F}_x - \hat{F}_y), \\ B_1 &= -2i\omega\hat{F}_\tau + \frac{\rho}{4}(3iF_y + 9F_x) - \frac{3i\rho}{4}(iF_x + F_y), \\ B_2 &= 2\omega\hat{F}_\tau - \frac{3i\rho}{4}(3iF_y + F_x) + \frac{3\rho}{4}(iF_x + F_y). \end{aligned} \tag{4.6.7}$$

To simplify the analysis, we transition to the travelling wave coordinates

$$Z = x - U\tau, \quad W = y - V\tau,$$

so that time derivatives transform as $F_\tau = -UF_Z - VF_W$. Substituting these into equations (4.6.7), we obtain

$$\begin{aligned} A_1 &= 2i\omega(UF_Z + VF_W) - 3\rho\hat{F}_Z, \qquad & A_2 &= 2\omega(UF_Z + VF_W) - 3\rho\hat{F}_W, \\ B_1 &= 2i\omega(U\hat{F}_Z + V\hat{F}_W) + 3\rho F_Z, \qquad & B_2 &= -2\omega(U\hat{F}_Z + V\hat{F}_W) + 3\rho F_W. \end{aligned} \tag{4.6.8}$$

Since M_1 is singular, the consistency conditions require that the right-hand side vectors lie within the range of the respective matrices. Hence, we impose

$$\mathbf{n}_1^* \cdot \mathbf{A} = 0, \qquad \mathbf{n}_2^* \cdot \mathbf{B} = 0,$$

where $\mathbf{n}_1^* = (1, i)$, $\mathbf{n}_2^* = (1, -i)$. These yield

$$\begin{aligned} A_1 + iA_2 &= 0, \\ B_1 - iB_2 &= 0. \end{aligned} \tag{4.6.9}$$

Substituting the expressions for A_1, A_2, B_1, B_2 into (4.6.9) results in

$$\begin{aligned} 4i\omega(UF_Z + VF_W) - 3\rho(\hat{F}_Z + i\hat{F}_W) &= 0, \\ 4i\omega(U\hat{F}_Z + V\hat{F}_W) + 3\rho(F_Z - iF_W) &= 0. \end{aligned} \tag{4.6.10}$$

These relations involve a mix of real and imaginary parts. The asymmetry between them suggests that a fully localised 2D solution not exist. Instead, we could seek a solution in the form of a plane wave extended in one direction. If $U, V \neq 0$, system (4.6.10) can be rewrite as

$$M_{D1} \begin{pmatrix} F_Z \\ F_W \end{pmatrix} = M_{D2} \begin{pmatrix} \hat{F}_Z \\ \hat{F}_W \end{pmatrix}, \tag{4.6.11}$$

where $\gamma = \dfrac{4i\omega}{3\rho}$, and

$$M_{D1} = \begin{pmatrix} U\gamma & V\gamma \\ -\frac{1}{\gamma} & \frac{i}{\gamma} \end{pmatrix}, \qquad M_{D2} = \begin{pmatrix} 1 & i \\ U & V \end{pmatrix}.$$

Assuming both M_{D1} and M_{D2} are invertible, we may write

$$\begin{pmatrix} F_Z \\ F_W \end{pmatrix} = \frac{1}{\gamma(iU + V)} \begin{pmatrix} -\gamma^2 UV + i & -V^2\gamma^2 - 1 \\ U^2\gamma^2 + 1 & \gamma^2 UV + i \end{pmatrix} \begin{pmatrix} \hat{F}_Z \\ \hat{F}_W \end{pmatrix}, \tag{4.6.12}$$

$$\begin{pmatrix} \hat{F}_Z \\ \hat{F}_W \end{pmatrix} = \frac{1}{\gamma(iU - V)} \begin{pmatrix} -\gamma^2 UV - i & -V^2\gamma^2 - 1 \\ U^2\gamma^2 + 1 & \gamma^2 UV - i \end{pmatrix} \begin{pmatrix} F_Z \\ F_W \end{pmatrix}. \tag{4.6.13}$$

To simplify the dimensionality of the system $F(Z, W, T)$, we introduce a re-

duced coordinate

$$\tilde{Z} = Z - \mu W, \qquad \tilde{F}(Z, W, T) = \tilde{F}(\tilde{Z}, T), \tag{4.6.14}$$

where μ is a real parameter chosen to eliminate the mixed derivative. Substituting into the characteristic PDE results in a quadratic equation for μ

$$\tilde{F}_{\tilde{Z}\tilde{Z}} \left[(-V^2\gamma^2 - 1)\mu^2 + 2\gamma^2 UV\mu - (U^2\gamma^2 + 1) \right] = 0.$$

This shows that the solution is not fully localised but rather extends in one direction, exhibiting quasi-one-dimensional behaviour. A non-trivial real solution for μ exists when the discriminant is positive, which is satisfied if

$$U^2 + V^2 > \frac{9\rho^2}{16\omega^2},$$

where $\omega^2 = \Omega^2 + \dfrac{3\rho}{2} \neq 0$. Since the solution has already been assumed in the form $\tilde{F}(\tilde{Z}, T)$, where $\tilde{Z} = Z - \mu W$, it is not necessary to further express $G_1, Q_1, \hat{G}_1, \hat{Q}_1$ in terms of both Z and W. The envelope is treated as quasi-one-dimensional along the direction defined by $\tilde{Z}$, and thus all relevant derivatives and corrections naturally reduce to functions of $\tilde{Z}$ and T. We therefore proceed using the 1D form in the subsequent analysis.

4.6.3 Harmonic terms $\mathcal{O}(\varepsilon^3 e^{i\theta})$

We now proceed to the analysis by substituting the dirac point in subsection 4.3.7. Using the established relations (4.6.4) $(F, P, \hat{F}, \hat{P})^T = F(1, -i, 0, 0)^T + \hat{F}(0, 0, 1, i)^T$, and incorporating the results for $(G, Q)^T$ and $(\hat{G}, \hat{Q})^T$, we obtain the system

$$\mathbf{M}_1 \begin{pmatrix} R_1 \\ H_1 \\ \hat{R}_1 \\ \hat{H}_1 \end{pmatrix} = \begin{pmatrix} A_{31} \\ A_{32} \\ A_{33} \\ A_{34} \end{pmatrix}, \tag{4.6.15}$$

where the matrix $\mathbf{M}_1$ is given in (4.6.2), and the expressions $A_{31}, A_{32}, A_{33}, A_{34}$ are derived from (4.3.30)–(4.3.33), evaluated at the Dirac point. Applying the consistency conditions at $\rho = 1$, as defined by the inner products with the adjoint kernel vectors $\mathbf{n}_1^*, \mathbf{n}_2^*$ in (4.6.5), we obtain

$$A_{31} + iA_{32} = 0, \tag{4.6.16}$$

$$A_{33} - iA_{34} = 0, \tag{4.6.17}$$

Since we assume a reduced solution of the form $\tilde{F}(\tilde{Z}, T)$, where $\tilde{Z} = Z - \mu W$, we define $\hat{F} = e^{iv}\tilde{F}$, with $v \in \mathbb{R}$. Substituting This yields the coupled NLS equations

$$\begin{aligned} 0 &= 4i\omega\tilde{F}_T - 10\lambda|\tilde{F}|^2\tilde{F} + \frac{3}{2}e^{iv}(1 - \mu^2 + 2i\mu)\tilde{F}_{\tilde{Z}\tilde{Z}} \\ &\quad + 2(U^2 + V^2\mu^2 - 2UV\mu)\tilde{F}_{\tilde{Z}\tilde{Z}}, \end{aligned} \tag{4.6.18}$$

$$\begin{aligned} 0 &= 4i\omega e^{iv}\tilde{F}_T - 10\lambda e^{iv}|\tilde{F}|^2\tilde{F} + \frac{3}{2}(1 - \mu^2 - 2i\mu)\tilde{F}_{\tilde{Z}\tilde{Z}} \\ &\quad + 2e^{iv}(U^2 + V^2\mu^2 - 2UV\mu)\tilde{F}_{\tilde{Z}\tilde{Z}}. \end{aligned} \tag{4.6.19}$$

By subtracting (4.6.18) from (4.6.19), we obtain

$$0 = e^{iv}(1 - \mu^2 + 2i\mu) - e^{-iv}(1 - \mu^2 - 2i\mu), \tag{4.6.20}$$

which leads to $\mu = \tan(v/2)$, hence $v = 2\tan^{-1}(\mu)$. Adding (4.6.18) and (4.6.19) results in

$$0 = 4i\omega\tilde{F}_T - 10\lambda|\tilde{F}|^2\tilde{F} + D\,\tilde{F}_{\tilde{Z}\tilde{Z}}, \tag{4.6.21}$$

where the dispersion coefficient D is given by

$$D = 2\left(U^2 + V^2\mu^2 - 2UV\mu + \frac{1}{2}(1+\mu^2)\right).$$

In (4.6.21), the dispersion coefficient D is always positive for real values of μ, indicating a defocusing regime when $\lambda > 0$. Conversely, for $\lambda < 0$, the system enters a focusing regime, which may lead to modulational instability.

4.7 Case 4 and 5: Acoustic and Optical Saddles

4.7.1 Harmonic terms $\mathcal{O}(\varepsilon e^{i\theta})$

In this subsection, we analyse both the acoustic and optical saddle cases. To simplify the calculations, we consider the saddle point located at $(k,l) = \left(\frac{\pi}{3}, 0\right)$, where the corresponding frequencies are $\omega_4 = \sqrt{\Omega^2 + \rho}$ for the acoustic mode, and $\omega_5 = \sqrt{\Omega^2 + 2\rho}$ for the optical mode. At this point, the leading-order system yields the following equation relating $F, \hat{F}, P$, and $\hat{P}$

$$\mathbf{M}_1 \begin{pmatrix} F \\ P \\ \hat{F} \\ \hat{P} \end{pmatrix} = \begin{pmatrix} 0 \\ 0 \\ 0 \\ 0 \end{pmatrix}, \tag{4.7.1}$$

where the matrix $\mathbf{M}_1$ takes the form

$$\begin{pmatrix} \pm\frac{\rho}{2} & 0 & \frac{\rho}{2}e^{i\pi/3} & 0 \\ 0 & \pm\frac{\rho}{2} & 0 & -\frac{3\rho}{2}e^{i\pi/3} \\ \frac{\rho}{2}e^{-i\pi/3} & 0 & \pm\frac{\rho}{2} & 0 \\ 0 & -\frac{3\rho}{2}e^{-i\pi/3} & 0 & \pm\frac{\rho}{2} \end{pmatrix} \begin{pmatrix} F \\ P \\ \hat{F} \\ \hat{P} \end{pmatrix} = \begin{pmatrix} 0 \\ 0 \\ 0 \\ 0 \end{pmatrix}, \tag{4.7.2}$$

with the positive sign (+) corresponding to the acoustic saddle and the negative sign (−) to the optical saddle.

To determine the leading-order components, we reduce the matrix $\mathbf{M}_1$ to echelon form. This reduction allows us to express the solution vector $\mathbf{v} = \left(F, P, \hat{F}, \hat{P}\right)^T$ in a normalised form. In particular, the components are related in magnitude and phase as

$$\left(F, P, \hat{F}, \hat{P}\right)^T = F\left(1, 0, \pm e^{-i\pi/3}, 0\right)^T, \tag{4.7.3}$$

with the (−) and (+) signs representing the acoustic and optical cases, respectively.

4.7.2 Harmonic terms $\mathcal{O}(\varepsilon^2 e^{i\theta})$

In this subsection, we analyse the second-order harmonic terms for both acoustic and optical saddle cases. We focus on the point $(k, l) = (\pi/3, 0)$, where the acoustic and optical frequencies are $\omega_4 = \sqrt{\Omega^2 + \rho}$ and $\omega_5 = \sqrt{\Omega^2 + 2\rho}$, respectively. The governing system is given by

$$\mathbf{M}_1 \begin{pmatrix} G_1 \\ Q_1 \\ \hat{G}_1 \\ \hat{Q}_1 \end{pmatrix} = \begin{pmatrix} A_1 \\ A_2 \\ A_3 \\ A_4 \end{pmatrix} = \mathbf{d}_2, \tag{4.7.4}$$

where $\mathbf{M}_1$ is defined in (4.7.2), and we substitute the leading-order approximation

$$\left(F, P, \hat{F}, \hat{P}\right)^T = F\left(1, 0, \pm e^{-i\pi/3}, 0\right)^T,$$

with $(+)$ for the optical case and $(-)$ for the acoustic case (4.7.3).
We evaluate A_1, A_2, A_3, A_4 at $(k, l) = (\pi/3, 0)$. These are derived from equations (4.3.25) to (4.3.28) in Subsection 4.3.6, we obtain

$$\begin{aligned} A_1 &= 2i\omega F_\tau + \frac{5\rho}{2} e^{i\pi/3}\hat{F}_x, & A_2 &= \frac{3\rho}{2} e^{i\pi/3}\hat{F}_y, \\ A_3 &= 2i\omega \hat{F}_\tau - \frac{5\rho}{2} e^{-i\pi/3} F_x, & A_4 &= -\frac{3\rho}{2} e^{-i\pi/3} F_y. \end{aligned} \tag{4.7.5}$$

Introducing the travelling wave coordinates $Z = x - U\tau$, $W = y - V\tau$, we rewrite these as

$$\begin{aligned} A_1 &= -2i\omega(UF_Z + VF_W) + \frac{5\rho}{2} e^{i\pi/3}\hat{F}_Z, & A_2 &= \frac{3\rho}{2} e^{i\pi/3}\hat{F}_W, \\ A_3 &= -2i\omega(U\hat{F}_Z + V\hat{F}_W) - \frac{5\rho}{2} e^{-i\pi/3} F_Z, & A_4 &= -\frac{3\rho}{2} e^{-i\pi/3} F_W. \end{aligned} \tag{4.7.6}$$

For the acoustic case, using $\left(F, P, \hat{F}, \hat{P}\right)^T = F\left(1, 0, -e^{-i\pi/3}, 0\right)^T$, we get

$$\begin{aligned} A_{1,\mathrm{ac}} &= -2i\omega(UF_Z + VF_W) - \frac{5\rho}{2} F_Z, & A_{2,\mathrm{ac}} &= -\frac{3\rho}{2} e^{i\pi/3} F_W, \\ A_{3,\mathrm{ac}} &= 2i\omega e^{-i\pi/3}(UF_Z + VF_W) - \frac{5\rho}{2} e^{-i\pi/3} F_Z, & A_{4,\mathrm{ac}} &= \frac{3\rho}{2} e^{-i\pi/3} F_W. \end{aligned} \tag{4.7.7}$$

For the optical case, with $\left(F, P, \hat{F}, \hat{P}\right)^T = F\left(1, 0, e^{-i\pi/3}, 0\right)^T$, we find

$$\begin{aligned} A_{1,\mathrm{op}} &= -2i\omega(UF_Z + VF_W) + \frac{5\rho}{2} F_Z, & A_{2,\mathrm{op}} &= \frac{3\rho}{2} F_W, \\ A_{3,\mathrm{op}} &= -2i\omega e^{-i\pi/3}(UF_Z + VF_W) - \frac{5\rho}{2} e^{-i\pi/3} F_Z, & A_{4,\mathrm{op}} &= -\frac{3\rho}{2} e^{-i\pi/3} F_W. \end{aligned} \tag{4.7.8}$$

To determine the velocities U, V and the coefficients $G_1, Q_1, \hat{G}_1, \hat{Q}_1$, we rewrite

system (4.7.4) in reduced 2×2 block matrix C.1 form

$$\begin{pmatrix} M_{11} & M_{12} \\ M_{21} & M_{22} \end{pmatrix} \begin{pmatrix} \overline{\mathbf{G}}_1 \\ \overline{\hat{\mathbf{G}}}_1 \end{pmatrix} = \begin{pmatrix} \mathbf{A} \\ \mathbf{B} \end{pmatrix}, \tag{4.7.9}$$

where $M_{11} = M_{22} = \pm\frac{\rho}{2}I$, with $(+)$ for acoustic and $(-)$ for optical. Also,

$$M_{12} = \frac{\rho}{4}(1 + i\sqrt{3}) \begin{pmatrix} 1 & 0 \\ 0 & -3 \end{pmatrix}, \quad \mathbf{A} = \begin{pmatrix} A_1 \\ A_2 \end{pmatrix}, \quad \mathbf{B} = \begin{pmatrix} A_3 \\ A_4 \end{pmatrix}.$$

Following the reduction in Appendix C.1.9, assuming $\rho = 1$, we find

$$\left(M_{11} - M_{12}M_{22}^{-1}M_{12}^{*}\right)\overline{\mathbf{G}}_1 = \mathbf{A} - M_{12}M_{22}^{-1}\mathbf{B}, \tag{4.7.10}$$

where

$$M_{11} - M_{12}M_{22}^{-1}M_{12}^{*} = \begin{pmatrix} 0 & 0 \\ 0 & \pm 4 \end{pmatrix},$$

where $(-)$ corresponds to the acoustic case, and $(+)$ to the optical case. This leads to the kernel form

$$\begin{pmatrix} G_1 \\ Q_1 \end{pmatrix} = \mu \begin{pmatrix} 1 \\ 0 \end{pmatrix} + \tilde{G} \begin{pmatrix} 0 \\ 1 \end{pmatrix}, \qquad \text{without loss the generate, we take } \mu = 0.$$

Starting with the acoustic case, we apply the consistency condition using the normal vector $\mathbf{n} = (1, 0)^T$, and obtain

$$\begin{pmatrix} 1 \\ 0 \end{pmatrix} \cdot \begin{pmatrix} -4\omega i\left(UF_Z + VF_W\right) \\ 3F_W \end{pmatrix} = \mathbf{0}. \tag{4.7.11}$$

This leads to the condition

$$-4\omega i\left(UF_Z + VF_W\right) = 0. \tag{4.7.12}$$

Since $\omega \neq 0$ and that the derivatives F_Z and F_W are not identically zero, we must conclude

$$U = 0, \qquad V = 0. \tag{4.7.13}$$

Thus, the group velocity vanishes at this saddle point. Then for the acoustic case, we find

$$\tilde{G}_{ac} \begin{pmatrix} 0 \\ -4 \end{pmatrix} = \begin{pmatrix} -4\omega i \left(UF_Z + VF_W\right) \\ 3F_W \end{pmatrix}, \tag{4.7.14}$$

$$-4\tilde{G}_{\text{ac}} = 3F_W \quad \Rightarrow \quad \tilde{G}_{\text{ac}} = -\frac{3}{4}F_W. \tag{4.7.15}$$

Substituting into the reduced system, we find

$$\begin{pmatrix} G_{1,\text{ac}} \\ Q_{1,\text{ac}} \\ \hat{G}_{1,\text{ac}} \\ \hat{Q}_{1,\text{ac}} \end{pmatrix} = \begin{pmatrix} 0 \\ -\frac{3}{4}F_W \\ -5e^{-i\pi/3}F_Z \\ \frac{3}{4}e^{-i\pi/3}F_W \end{pmatrix}. \tag{4.7.16}$$

Returning to equation (4.7.10), we now analyse the optical case, we have

$$\tilde{G}_{\text{op}} \begin{pmatrix} 0 \\ 4 \end{pmatrix} = \begin{pmatrix} -4\omega i(UF_Z + VF_W) \\ 6F_W \end{pmatrix}. \tag{4.7.17}$$

We now apply the consistency condition using the normal vector $\mathbf{n} = (1, 0)^T$, we obtain

$$\begin{pmatrix} 1 \\ 0 \end{pmatrix} \cdot \begin{pmatrix} -4\omega i(UF_Z + VF_W) \\ 6F_W \end{pmatrix} = \mathbf{0}. \tag{4.7.18}$$

For the system to be consistent, this expression must vanish:

$$-4\omega i(UF_Z + VF_W) = 0. \tag{4.7.19}$$

Since $\omega \neq 0$ and $F_Z, F_W \neq 0$, this implies

$$U = 0, \quad V = 0. \tag{4.7.20}$$

Hence, for both acoustic and optical saddle points, the group velocity vanishes. For the optical case in (4.7.17), where $\tilde{G}_{\text{op}} = \frac{3}{2}F_W$, we obtain

$$\begin{pmatrix} G_{1,\text{op}} \\ Q_{1,\text{op}} \\ \hat{G}_{1,\text{op}} \\ \hat{Q}_{1,\text{op}} \end{pmatrix} = \begin{pmatrix} 0 \\ \frac{3}{2}F_W \\ 5e^{-i\pi/3}F_Z \\ -\frac{3}{2}e^{-i\pi/3}F_W \end{pmatrix}. \tag{4.7.21}$$

4.7.3 The acoustic saddle harmonic $\mathcal{O}(\varepsilon^3 e^{i\theta})$ terms

From Subsection 4.3.7, evaluated at the point $(k, l) = (\pi/3, 0)$, and using the results from Subsection 4.7.2, we obtain

$$\mathbf{M}_1 \begin{pmatrix} H_1 \\ R_1 \\ \hat{H}_1 \\ \hat{R}_1 \end{pmatrix} = \begin{pmatrix} A_{31} \\ A_{32} \\ A_{33} \\ A_{34} \end{pmatrix} = \mathbf{d}_3. \tag{4.7.22}$$

Here, $A_{31}, A_{32}, A_{33}, A_{34}$ are obtained after transforming to the travelling wave coordinates, we have

$$\begin{aligned}
A_{31} &= 2i\omega F_T - \lambda\left(3|F|^2F\right) - \frac{\rho}{4}\left(9F_{ZZ} + 3F_{WW}\right) + \frac{5\rho}{2}e^{i\pi/3}\hat{G}_{1Z} + \frac{3\rho}{2}e^{i\pi/3}\hat{Q}_{1W}, \\
A_{32} &= \frac{3\rho}{2}e^{i\pi/3}\hat{Q}_{1Z} + \frac{3\rho}{2}\left(e^{i\pi/3}\hat{G}_{1W} - F_{ZW}\right), \\
A_{33} &= -2i\omega e^{-i\pi/3}F_T + \lambda e^{-i\pi/3}\left(3|F|^2F\right) + \frac{\rho}{4}e^{-i\pi/3}\left(9F_{ZZ} + 3F_{WW}\right) \\
&\quad - \frac{5\rho}{2}e^{-i\pi/3}G_{1Z} - \frac{3\rho}{2}e^{-i\pi/3}Q_{1W}, \\
A_{34} &= \frac{3\rho}{2}e^{-i\pi/3}Q_{1Z} + \frac{3\rho}{2}e^{-i\pi/3}\left(F_{ZW} - G_{1W}\right).
\end{aligned} \tag{4.7.23}$$

As in previous sections, we reduce the matrix $\mathbf{M}_1$ in (4.7.2) into block form appendix C.1. The system can then be written as

$$\begin{pmatrix} M_{11} & M_{12} \\ M_{21} & M_{22} \end{pmatrix} \begin{pmatrix} \overline{\mathbf{H}}_1 \\ \overline{\mathbf{R}}_1 \end{pmatrix} = \begin{pmatrix} \mathbf{A} \\ \mathbf{B} \end{pmatrix}, \tag{4.7.24}$$

where $M_{11} = M_{22} = \frac{\rho}{2} I$, $M_{21} = M_{12}^{*T}$, and $\mathbf{A} = (A_{31}, A_{32})^T$, $\mathbf{B} = (A_{33}, A_{34})^T$. Also, $\overline{\mathbf{H}}_1 = (H_1, R_1)^T$, $\overline{\mathbf{R}}_1 = (\hat{H}_1, \hat{R}_1)^T$.

Thus, the system becomes

$$M_{11}\,\overline{\mathbf{H}}_1 + M_{12}\,\overline{\mathbf{R}}_1 = \mathbf{A}, \tag{4.7.25}$$

$$M_{12}^{*T}\,\overline{\mathbf{H}}_1 + M_{22}\,\overline{\mathbf{R}}_1 = \mathbf{B}. \tag{4.7.26}$$

By eliminating $\overline{\mathbf{R}}_1$, we obtain

$$\left(M_{11} - M_{12}M_{22}^{-1}M_{12}^{*T}\right)\overline{\mathbf{H}}_1 = \mathbf{A} - M_{12}M_{22}^{-1}\mathbf{B}. \tag{4.7.27}$$

Let $\mathbf{n} = (1, 0)^T$ be the vector normal to the range of the $\mathbf{M}_1$ in (4.7.2) . The consistency condition is then

$$\mathbf{n} \cdot \left(\mathbf{A} - M_{12}M_{22}^{-1}\mathbf{B}\right) = \mathbf{0},$$

which leads to the NLS equation

$$\theta i F_T + D_N |F|^2 F + D_Z F_{ZZ} + D_W F_{WW} + D_M F_{ZW} = 0. \tag{4.7.28}$$

Here, the coefficients are defined as

$$\theta = 4\sqrt{\Omega^2 + \rho}, \quad D_Z = -17\rho, \quad D_W = -\frac{3}{2}\rho, \quad D_M = 0, \quad D_N = -6\lambda. \tag{4.7.29}$$

Furthermore, the ellipticity condition [8, 15] is given by

$$\mathcal{E} = 4D_Z D_W - D_M^2 > 0, \tag{4.7.30}$$

which evaluates to

$$\mathcal{E} = 4(-17\rho)\left(-\frac{3}{2}\rho\right) = 102\rho^2 > 0. \tag{4.7.31}$$

Hence, the system is elliptic. The focusing condition [8, 9, 19] is

$$D_Z D_N = 90\lambda\rho > 0 \quad \text{if} \quad \lambda > 0, \tag{4.7.32}$$

so a bright breather exists when $\lambda > 0$.

4.7.4 The optical saddle harmonic $\mathcal{O}(\varepsilon^3 e^{i\theta})$ terms

Using the optical results from Subsection 4.7.2, and following a procedure similar to the acoustic case at order $\mathcal{O}(\varepsilon^3 e^{i\theta})$, we obtain

$$\mathbf{M}_1 \begin{pmatrix} H_1 \\ R_1 \\ \hat{H}_1 \\ \hat{R}_1 \end{pmatrix} = \begin{pmatrix} A_{31} \\ A_{32} \\ A_{33} \\ A_{34} \end{pmatrix} = \mathbf{d}_{22}. \tag{4.7.33}$$

Here, $\mathbf{M}_1$ is given in equation (4.7.2), and the components $A_{31}, A_{32}, A_{33}, A_{34}$

are expressed as

$$
\begin{aligned}
A_{31} &= 2i\omega F_T - \lambda\left(3|F|^2F\right) + \frac{\rho}{4}\left(9F_{ZZ} + 3F_{WW}\right) + \frac{5\rho}{2}e^{i\pi/3}\hat{G}_{1Z} + \frac{3\rho}{2}e^{i\pi/3}\hat{Q}_{1W},\\
A_{32} &= \frac{3\rho}{2}e^{i\pi/3}\hat{Q}_{1Z} + \frac{3\rho}{4}\left(F_{ZW} + e^{i\pi/3}\hat{G}_{1W}\right),\\
A_{33} &= 2i\omega e^{-i\pi/3}F_T - \lambda e^{-i\pi/3}\left(3|F|^2F\right) + \frac{\rho}{4}e^{-i\pi/3}\left(9F_{ZZ} + 3F_{WW}\right)\\
&\quad - \frac{5\rho}{2}e^{-i\pi/3}G_{1Z} - \frac{3\rho}{2}e^{-i\pi/3}Q_{1W},\\
A_{34} &= \frac{3\rho}{2}e^{-i\pi/3}Q_{1Z} + \frac{3\rho}{4}e^{-i\pi/3}\left(F_{ZW} - G_{1W}\right).
\end{aligned}
\tag{4.7.34}
$$

Using the relation in equation (4.7.25), the solvability (consistency) condition becomes

$$
\mathbf{n}\cdot\left(\mathbf{A} - M_{12}M_{22}^{-1}\mathbf{B}\right) = \begin{pmatrix}1\\0\end{pmatrix}\cdot\left(\mathbf{A} - M_{12}M_{22}^{-1}\mathbf{B}\right) = 0. \tag{4.7.35}
$$

Thus, the resulting NLS equation takes the form

$$
4i\sqrt{\Omega^2 + 2\rho}\,F_T - 6\lambda|F|^2F + 17\rho F_{ZZ} - 3\rho F_{WW} = 0. \tag{4.7.36}
$$

In contrast to the acoustic saddle case, the ellipticity condition for the optical saddle is not satisfied

$$
\mathcal{E} = 4D_ZD_W - D_M^2 = -204\rho^2 < 0, \tag{4.7.37}
$$

which indicates that the governing system is hyperbolic, The breather can be localised in only one direction, not both.

4.8 Discussion

In this chapter, we have investigated a mechanical symmetric honeycomb lattice interacting via linear NNIs and a nonlinear onsite potential. First, it was shown that the derived model of the equations of motion preserves symme-

try. This was demonstrated by applying asymptotic methods using a solution ansatz similar to those employed in [24], [23], and [26]. The dispersion relation was derived, which exhibits the expected symmetric behaviour and features both lower and upper flat bands, as well as acoustic and optical branches yielding a total of four dispersion surfaces (see Figures 4.4, 4.3, and 4.5).

Although the resulting system could not be solved in full generality for arbitrary wave numbers (k, l), we reduced it by considering special cases of specific wave numbers. This enabled a more tractable analysis of breather dynamics. A similar strategy was used by Wattis *et al.* [55], who reduced scalar honeycomb lattice under conditions when the symmetric potential terms were either zero or non-zero, leading to insights into breather behaviour in electrical lattices.

Next, we analysed the minimum and maximum of $\omega(k, l)$, deriving a coupled NLS equation in F and P, at $k = 0, l = 0$ as shown in Sections 4.4–4.5. A coupled NLS system was obtained which, due to the complexity of the coupling, could not be reduced to a single NLS equation similar to the cases treated in Section 3.4.1 of Chapter 3. In the Dirac case (Section 4.6), two elements in the kernel were considered, and the relative amplitudes were identified. By applying the coordinate transformation $\tilde{Z} = Z - \mu W$, we reduce the problem to a single spatial dimension. This enables the analysis of modulational instability: for $\lambda < 0$, the 1D NLS equation becomes focusing and supports ID breather solutions.

Finally, we demonstrated that the lattice equations can be reduced to a single cubic NLS equation in two saddle point cases (Section 4.7). An ellipticity condition on the wavevector was examined, allowing us to identify stationary breather solutions in the case of the acoustic saddle.

Conversely, for the optical saddle, a hyperbolic NLS equation was found. Although the theoretical framework for the mechanical triangular lattice (Chapter 3) and the mechanical honeycomb lattice (Chapter 4) is similar, key differences arise during analysis. For instance, stationary breather solutions were identified in the honeycomb lattice at the acoustic saddle, and modulational

instability emerged in the Dirac case when $\lambda < 0$. In contrast, the global maximum and minimum cases for the honeycomb lattice reduce to coupled NLS systems similar to the global minimum case in the mechanical triangular lattice.

It is important to note that the results presented in this chapter are entirely analytical, based on asymptotic analysis of breather solutions in the mechanical honeycomb lattice. From a practical perspective, it would be valuable to extend this work to include numerical simulations of honeycomb networks with both linear and nonlinear NNIs. Previous numerical studies have shown that hexagonal lattices can support breather solutions, as noted by [52], [53], and [73].

Chapter 5

Conclusion

In this thesis, we have explored discrete breathers, spatially localised, time-periodic, and long-lived solutions, which are found in many nonlinear lattice structures, including MiM chains and mechanical triangular and honeycomb lattices in 2D. In Chapter 1, we illustrated how the interplay between nonlinearity and discreteness enables DBs to form and maintain their envelope over long durations, even in the presence of phonon resonances that might otherwise induce decay. DBs occur in various lattice models, including electrical and mechanical systems, within both square and hexagonal geometries. We reviewed several foundational works, including those demonstrating the existence of DBs in diatomic, MiM, and 2D hexagonal lattices, and outlined current research directions focused on DBs in both electrical and mechanical settings. In Section 1.3, we discussed common analytical techniques for deriving approximate small-amplitude solutions. Section 1.3.2 summarised the multiple scales approximation, as presented in [19, 20], and applied it within this thesis. This method has been widely employed in nonlinear systems, as illustrated by works such as [1, 21, 23, 26, 55, 74]. In Section 1.4.5, we focused on key results concerning hexagonal lattices, with selected applications presented in Section 1.4.7.

In Chapter 2, we conducted a numerical investigation of the fully nonlinear MiM system introduced in [1]. We assessed the robustness of the MiM model

by using initial conditions derived from asymptotic reductions to the NLS equation. Our findings revealed that localised structures such as breathers and breather-kinks emerge under certain conditions involving wavenumber k, quadratic nonlinearities α, a, and interaction strength ρ. Numerical simulations confirmed the presence of stationary breathers at $k = 0, \pi$, and moving breathers at other wavenumbers for both optical and acoustic branches. The stability of these modes is primarily governed by ρ, and to a lesser extent by the mass ratio μ. In symmetric cases (Case I), stationary DB solutions are more stable in the optical branch at $k = 0$ and $k = \pi$, with long-lived acoustic modes occurring for large ρ. In Case III, breather-kink solutions were observed in both stationary and moving forms, with stability varying based on ρ and μ. Moreover, we observed that in moving modes for Case I ($k = 0.1, 3.1$), both optical and acoustic waves displayed long-lived behaviour for large ρ, whereas weak instabilities were noted at lower ρ. Similar trends were found in Cases II and IV. In some configurations within Case IV, the governing equation reduces to a CGL equation. Generally, moving modes tend to be more stable at higher values of ρ across all μ. Appendix A presents detailed visualisations illustrating how μ and ρ affect breather stability and dynamics, including breather-kinks or wobbling kinks.

In Chapter 3, we developed a model for a mechanical triangular lattice, allowing in-plane motion with two degrees of freedom per node, and applied asymptotic analysis incorporating symmetric onsite potentials and NNIs. The dispersion relation in Section 4.3.2 produced two branches acoustic and optical enabling the study of stationary breathers, including Dirac points (see Table 3.1). Using multiple scales analysis, we derived the NLS equation (3.3.45) and identified the focusing condition and the ellipticity condition (3.3.47) and (3.3.46), respectively for DB solutions. In Section 3.4, we simplified the system by neglecting quadratic nonlinearities, summarising the stationary results in Table 3.2 (see Appendix B for details). We established stationary breather solutions for symmetric triangular lattices in Case 3 (global maximum) and Case

5 (optical saddle). This work extends prior results on square lattices to 2D triangular configurations, confirming that triangular lattices support breather solutions.

In Chapter 4, we studied a symmetric mechanical honeycomb lattice with linear NNIs and onsite potential energy. Using asymptotic techniques, we derived and validated the symmetry of the governing equations. The dispersion relation exhibited the expected symmetry with lower and upper flat bands, and both optical and acoustic branches. By selecting special wavenumbers, we simplified the analysis, following the approach of Wattis *et al.* [55]. We derived coupled NLS equations for specific wavenumber points, as presented in Sections 4.4, 4.5, and 4.6. In contrast, for the saddle point cases optical and acoustic considered in Section 4.7, the system reduces to single NLS equations. Stationary breather solutions were identified at acoustic saddle points, while optical saddle points exhibited more defocusing propagation dynamics. Whereas the triangular lattice supports breather solutions in case 3 (Global maximum) and case 5 (saddle point), this is notably not the case for the honeycomb lattice. The results are fully analytical and offer insights into the nature of DBs in honeycomb structures.

Future investigations could focus on extending MiM systems into two dimensions, considering triangular and hexagonal configurations with both scalar and vector displacements. Further research could also explore breather-kink interactions, examining their mechanisms, stability, and possible applications in nonlinear wave systems.

It would also be worthwhile to generalise the asymptotic approximation to mechanical triangular and honeycomb lattices with cubic onsite nonlinearities, supported by numerical simulations. Additional directions include examining alternative 2D lattice geometries such as square, 2D diatomic, kagome, and diamond lattices, as discussed by Vainchtein [75].

Given the complexity of discrete breather dynamics, particularly in triangular and honeycomb geometries, numerical simulations are essential for validating

analytical results and exploring regimes beyond the reach of asymptotic methods.

Bibliography

[1] J A D Wattis. Breather modes of fully nonlinear mass-in-mass chains. *Phys. Rev. E*, 105(5):054212, 2022.

[2] K khusnutdinova and V Silberschmidt. Lattice modelling of nonlinear waves in a bi-layer with delamination. *Proc. Estonian Acad. Sci. Phys. Math*, 52(1):63–75, 2003.

[3] S J Flach and C R Willis. Discrete breathers. *Phys. Rep.*, 295(5):181–264, 1998.

[4] J F R Archilla, Noé Jiménez, VJ Sánchez-Morcillo, and LM García-Raffi. *Quodons in Mica: Nonlinear Localized Travelling Excitations in Crystals*, volume 221. Springer, 2015.

[5] I V Barashenkov and O F Oxtoby. Wobbling kinks in ϕ^4 theory. *Phys. Rev. E.*, 80(2):026608, 2009.

[6] T Morikazu. Vibration of a chain with nonlinear interaction. *J. Phys. Soc. Jpn*, 22(2):431–436, 1967.

[7] P M Morse. Diatomic molecules according to the wave mechanics. ii. vibrational levels. *Phys. Rev.*, 34(1):57, 1929.

[8] P L Sulem, C Sulem. *The Nonlinear Schrödinger Equation: Self-Focusing and Wave Collapse* . Applied mathematical sciences (Springer-Verlag New York Inc.) ; 139. Springer, New York, 1999.

[9] M J Ablowitz and T P Horikis. Interacting nonlinear wave envelopes and rogue wave formation in deep water. *Phys. Fluids*, 27(1), 2015.

[10] J J Rasmussen and K Rypdal. Blow-up in nonlinear Schrödinger equations-I a general review. *Phys. Scr.*, 33(6):481–497, 1986.

[11] P G Kevrekidis, K O Rasmussen, and A R Bishop. The discrete nonlinear Schrödinger equation: a survey of recent results. *Int. J. Mod. Phys. B*, 15(21):2833–2900, 2001.

[12] A Vainchtein. Solitary wave propagation in a two-dimensional lattice. *Wave Motion*, 83:12–24, 2018.

[13] P G Kevrekidis and D J Frantzeskakis. Solitons in coupled nonlinear Schrödinger models: a survey of recent developments. *Rev. Phys.*, 1:140–153, 2016.

[14] Y Chen and X Xiao. Vector soliton pairs for a coupled nonautonomous nls model with partially nonlocal coupled nonlinearities under the external potentials. *Nonlinear Dyn*, 109(3):2003–2012, 2022.

[15] R Y Chiao, E Garmire, and C Townes. Self-trapping of optical beams. *Phys. Rev. Lett.*, 13(15):479, 1964.

[16] D Del Vescovo and I Giorgio. Dynamic problems for metamaterials: review of existing models and ideas for further research. *Int. J. Eng. Sci.*, 80:153–172, 2014.

[17] H Ding, Z Zhen, H Imtiaz, W Guo, H Zhu, and B Liu. Why are most 2d lattices hexagonal? the stability of 2d lattices predicted by a simple mechanics model. *Extreme Mechanics Letters*, 32:100507, 2019.

[18] L Zhang and X Wang. Analysis of exact solutions and stability analysis of a (2+1)-dimensional nonlinear schrödinger equation. *Optik (Stuttg.)*, 269:169905, 2022.

[19] M Remoissenet. *Waves Called Solitons: Concepts and Experiments*. Springer Science and Business Media, New York, 1999.

[20] C.M. Bender and S.A. Orszag. *Advanced Mathematical Methods for Scientists and Engineers I: Asymptotic Methods and Perturbation Theory*. Springer New York, New York, NY, 1999.

[21] I A Butt and J A D Wattis. Asymptotic analysis of combined breather–kink modes in a Fermi-Pasta-Ulam chain. *Physica D.*, 231(2):165–179, 2007.

[22] J A D Wattis, A Pickering, and P R Gordoa. Combined breathing–kink modes in the FPU lattice. *Physica D*, 240(7):547–553, 2011.

[23] I A Butt and J A D Wattis. Discrete breathers in a two-dimensional hexagonal Fermi-Pasta-Ulam lattice. *J. Phys. A Math*, 40(6):1239, 2007.

[24] I A Butt and J A D Wattis. Discrete breathers in a two-dimensional Fermi-Pasta-Ulam lattice. *J. Phys. Math. Gen.*, 39(18):4955, 2006.

[25] J A D Wattis and L M James. Discrete breathers in honeycomb Fermi–Pasta–Ulam lattices. *Journal of Physics A: Mathematical and Theoretical*, 47(34):345101, 2014.

[26] J A D Wattis and A S Alzaidi. Asymptotic analysis of breather modes in a two-dimensional mechanical lattice. *Physics. D*, 401:132207, 2020.

[27] E Fermi, P Pasta, S Ulam, and M Tsingou. Studies of the nonlinear problems. *Collect. Work. E. Fermi*, 2(5):978–988, 1955.

[28] N J Zabusky and M D Kruskal. Interaction of solitons in a collisionless plasma and the recurrence of initial states. *Phys.Rev.Lett*, 15(6):240, 1965.

[29] R S MacKay and S Aubry. Proof of existence of breathers for time-reversible or Hamiltonian networks of weakly coupled oscillators. *Nonlinearity*, 7(6):1623–1643, 1994.

[30] G James. Existence of breathers on FPU lattices. *C. R. Acad. Sci. Ser.*, 332(6):581–586, 2001.

[31] R Livi, M Spicci, and R S MacKay. Breathers on a diatomic FPU chain. *Nonlinearity*, 10(6):1421–1434, 1997.

[32] A Vainchtein, and Wright J D Starosvetsky, Y, and R Perline. Solitary waves in diatomic chains. *Phys. Rev. E*, 93(4):042210–042210, 2016.

[33] K R Jayaprakash, Y Starosvetsky, and A F Vakakis. New family of solitary waves in granular dimer chains with no precompression. *Phys.Rev. E*, 83(3):036606, 2011.

[34] S Sen, J Hong, J Bang, E Avalos, and R Doney. Solitary waves in the granular chain. *Phys. Rep*, 462(2):21–66, 2008.

[35] D Pelinovsky and G Schneider. The monoatomic FPU system as a limit of a diatomic FPU system. *Appl. Math. Lett.*, 107:106387, 2020.

[36] S Cadet. Transverse envelope solutions in an atomic chain. *Physics Letters A*, 121(2):77–82, 1987.

[37] S Cadet. Coupled transverse-longitudinal envelope modes in an atomic chain. *J. Phys., C.*, 20(30):L803, 1987.

[38] S Cadet. Propagation and interactions of nonlinear shear waves in a discrete lattice. *Wave ,Motion*, 11(1):77–97, 1989.

[39] P L Christiansen, A V Savin, and A V Zolotaryuk. Zig-zag version of the frenkel-kontorova model. *Phys. Rev. B.*, 54(18):12892–12902, 1996.

[40] K Khusnutdinova. Coupled Klein–Gordon equations and energy exchange in two-component systems. *EP J ST*, 147(1):45–72, 2007.

[41] K Khusnutdinova, A Samsonov, and A Zakharov. Nonlinear layered lattice model and generalized solitary waves in imperfectly bonded structures. *Phys. Rev. E Stat. Nonlin. Soft Matter Phys*, 79(5):056606, 2009.

[42] L Truskinovsky and A Vainchtein. Strictly supersonic solitary waves in lattices with second-neighbor interactions. *Physica D.*, 389:24–50, 2019.

[43] H Duran, H Xu, P G Kevrekidis, and A. Vainchtein. Unstable dynamics of solitary traveling waves in a lattice with long-range interactions. *Wave Motion*, 108:102836, 2022.

[44] P G Kevrekidis, A Vainchtein, M S Garcia, and C Daraio. Interaction of traveling waves with mass-with-mass defects within a Hertzian chain. *Phys.l Rev. E.*, 87(4):042911, 2013.

[45] P G Kevrekidis, A G Stefanov, and H Xu. Traveling waves for the mass in mass model of granular chains. *Lett. Math. Phys.*, 106(8):1067–1088, 2016.

[46] L Liu, G James, P G Kevrekidis, and A Vainchtein. Breathers in a locally resonant granular chain with precompression. *Physica D*, 331(C):27–47, 2016.

[47] T E Faver, R H Goodman, and J D Wright. Solitary waves in mass-in-mass lattices. *Z. Angew. Math. Phys.*, 71(6):1–20, 2020.

[48] S P Wallen, J Lee, D Mei, C Chong, P G. Kevrekidis, and N. Boechler. Discrete breathers in a mass-in-mass chain with Hertzian local resonators. *Phys. Rev. E*, 95(2), 2017.

[49] L Bonanomi, G Theocharis, and C Daraio. Wave propagation in granular chains with local resonances. *Phys. Rev. E*, 91(3):033208, 2015.

[50] M Porter, C Daraio, EB Herbold, I Szelengowicz, and P G Kevrekidis. Highly nonlinear solitary waves in periodic dimer granular chains. *Phys. Rev. E*, 77(1):015601, 2008.

[51] G Theocharis, N Boechler, P G Kevrekidis, S Job, M A Porter, and C Daraio. Intrinsic energy localization through discrete gap breathers in one-dimensional diatomic granular crystals. *Phys. Rev. E*, 82(5):056604, 2010.

[52] J L Marin, J C Eilbeck, and F M Russell. Localized moving breathers in a 2D hexagonal lattice. *Phys. Lett. A*, 248(2):225–229, 1998.

[53] J Bajars, J C Eilbeck, and B Leimkuhler. Nonlinear propagating localized modes in a 2D hexagonal crystal lattice. *Physica D*, 301-302:8–20, 2015.

[54] P G Kevrekidis, J Cuevas-Maraver, and D E Pelinovsky. Energy Criterion for the Spectral Stability of Discrete Breathers. *Phys. Rev. Lett.*, 117(9):1–5, 2016.

[55] J A D Wattis and L M James. Discrete breathers in honeycomb Fermi-Pasta-Ulam lattices. *J. Phys. A Math*, 47(34):345101, 2014.

[56] K J H Law, A Saxena, P G Kevrekidis, and A R Bishop. Localized structures in kagome lattices. *Phys. Rev. A*, 79(5):053818, 2009.

[57] R A Vicencio and M Johansson. Discrete flat-band solitons in the kagome lattice. *Phys. Rev. A.*, 87(6):061803, 2013.

[58] M A J Herrera, S N Kempkes, M B De Paz, A García-Etxarri, I Swart, C M Smith, and D Bercioux. Corner modes of the breathing kagome lattice: Origin and robustness. *Phys. Rev. B*, 105(8):085411, 2022.

[59] Y H Jung, J Kim. Hidden breathing kagome topology in hexagonal transition metal dichalcogenides. *Phys. Rev. B*, 105(8):085138, 2022.

[60] K Prabith, G Theocharis, and R Chaunsali. Nonlinear corner states in a topologically nontrivial kagome lattice. *Phys. Rev. B*, 110(10):104307, 2024.

[61] A Hofstrand. Families of discrete breathers on a nonlinear kagome lattice. *arXiv preprint arXiv:2412.06932*, 2024.

[62] V Koukouloyannis, P G Kevrekidis, G P Veldes, D J Frantzeskakis, D DiMarzio, X Lan, and V Radisic. Bright breathers in nonlinear left-handed metamaterial lattices. *Phys. Scr.*, 93(2):025202, 2018.

[63] H Duran, J Cuevas-Maraver, P G Kevrekidis, and A Vainchtein. Discrete breathers in a mechanical metamaterial. *Phys. Rev. E*, 107(1):014220, 2023.

[64] B Deng, J R Raney, K Bertoldi, and V Tournat. Nonlinear waves in flexible mechanical metamaterials. *J Appl Phys*, 130(4), 2021.

[65] C Chong, M Porter, P G Kevrekidis, and C Daraio. Nonlinear coherent structures in granular crystals. *J. Condens. Matter Phys.*, 29(41):413003, 2017.

[66] I Barashenkov. The continuing story of the wobbling kink. In *A Dynamical Perspective on the ϕ^4 Model: Past, Present and Future*, pages 187–212. Springer, 2019.

[67] Amir A, H Susanto, and J A D Wattis. Rapidly oscillating ac-driven long josephson junctions with phase shifts. *Phys.D*, 246(1):15–22, 2013.

[68] S J Flach and A V Gorbach. Discrete breathers—advances in theory and applications. *Phys. Rep.*, 467(1-3):1–116, 2008.

[69] R S MacKay and S Aubry. Proof of existence of breathers for time-reversible or hamiltonian networks of weakly coupled oscillators. *Nonlinearity*, 7(6):1623, 1994.

[70] A Alonso-Izquierdo, D Miguelez-Caballero, and L M Nieto. Scattering between orthogonally wobbling kinks. *Physica D*, page 134438, 2024.

[71] X Yi and S Liu. Stationary breather model in a two-dimensional hexagonal spring-mass lattice. *Nucl. Phys. B*, 951:114884, 2020.

[72] J Bajārs and J F R Archilla. Frequency–momentum representation of moving breathers in a two dimensional hexagonal lattice. *Physica D: Nonlinear Phenomena*, 441:133497, 2022.

[73] J Bajārs, J C Eilbeck, and B Leimkuhler. Two-dimensional mobile breather scattering in a hexagonal crystal lattice. *Phys. Rev. E*, 103(2):022212, 2021.

[74] I A Butt and J A D Wattis. Discrete breathers in a two-dimensional Fermi-Pasta-Ulam lattice. *J. Phys. Math. Gen.*, 39(18):4955, 2006.

[75] A Vainchtein. Solitary waves in FPU-type lattices. *Physica D*, 434:133252, 2022.

Appendix A

Supplementary material: Chapter 2

Appendix A: Introduction

This appendix presents supplementary figures corresponding to the numerical simulations discussed in Chapter 2. We provide a set of visual results illustrating the spatial profiles and temporal evolution of optical and acoustic discrete breather solutions in the fully nonlinear MiM FPUT chain. The figures cover various parameter regimes, including both zero and non-zero internal coupling (α) and outer mass nonlinearities (a), across different values of wave number k. These cases demonstrate the qualitative behaviour of the system under weak and strong nonlinearity (ρ), and the persistence or decay of localised modes over time.

The inclusion of these results serves two key purposes. First, it validates the numerical analyses carried out in Chapter 2, showing how breather and breather -kink solutions evolve under fully nonlinear dynamics. Second, it offers detailed insight into the localisation properties of both optical and acoustic branches, thereby supporting the broader discussion on the stability and robustness of breather and breather-kink modes. These visualisations enhance the connection between the theoretical predictions and the observed long-lived behaviours identified in the simulations. To avoid excessive length and visual density in Chapter 2, all corresponding figures have been compiled here in Appendix A. Variations in breather amplitude arise from the plotting of solutions at different time points.

Table A.1 displays optical breather profiles at wave number $k = 0$, evaluated at $t = 2000$ (with $N = 400$ or 1000 as appropriate), across four model cases defined by nonlinear parameter combinations:

- **Case I** ($a = 0$, $\alpha = 0$). Subfigures: (a) $\rho = 3, \mu = 3, \beta = -0.3, b = 1, W_b = 22.086$; (b) $\rho = 3, \mu = \frac{1}{3}, \beta = -0.01, b = 1, W_b = 13.441$; (c) $\rho = \frac{1}{3}, \mu = 3, \beta = -0.35, b = 1, W_b = 20.448$; (d) $\rho = \frac{1}{3}, \mu = \frac{1}{3}, \beta = -0.01, b = 1, W_b = 13.441$.

- **Case II** ($a = 0$, $\alpha = 1$). Subfigures: (a) $\beta = 0.18, b = 1, W_b = 27.726$; (b) $\beta = 0.367, b = 1, W_b = 23.153$; (c) $\beta = 2.92, b = 1, W_b = 19.289$; (d) $\beta = 3.33, b = 1, W_b = 23.281$.

Case	(a)$\rho = 3, \mu = 3$	(b)$\rho = 3, \mu = \frac{1}{3}$	(c) $\rho = \frac{1}{3}, \mu = 3$	(d)$\rho = \frac{1}{3}, \mu = \frac{1}{3}$
I	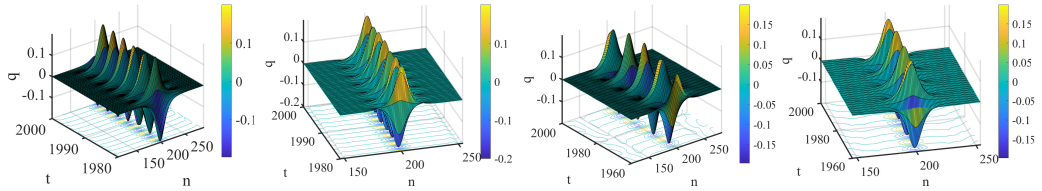			
II	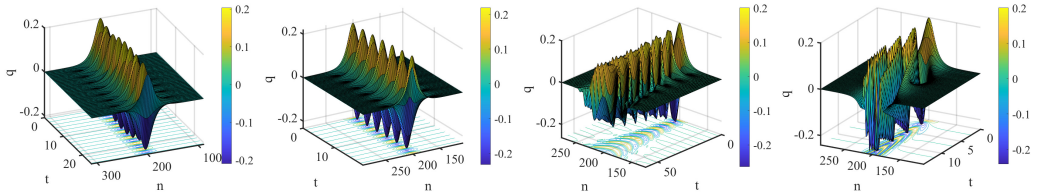			
III	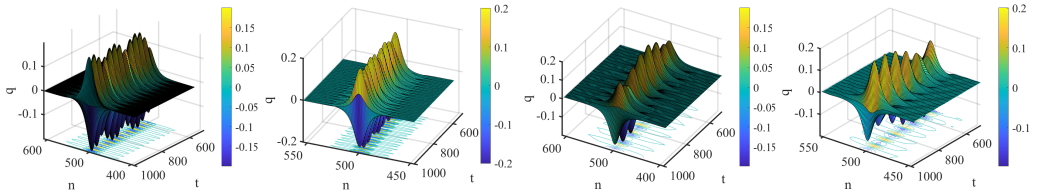			
IV	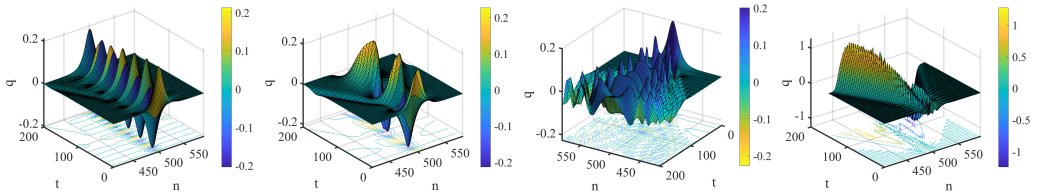			

Table A.1: Optical breather profiles at $k = 0$ for Cases I–IV.

- **Case III** ($a = 1$, $\alpha = 0$). Subfigures: (a) $\beta = -0.20, b = 1, W_b = 27.050$; (b) $\beta = -0.01, b = 1, W_b = 13.441$; (c) $\beta = -0.20, b = 1, W_b = 27.050$; (d) $\beta = -0.10, b = 1, W_b = 13.441$.

- **Case IV** ($a = 1$, $\alpha = 1$). Subfigures: (a) $\beta = 0.08, b = 1, W_b = 22.449$; (b) $\beta = 0.366, b = 1, W_b = 20.332$; (c) $\beta = 2.98, b = 1, W_b = 20.351$; (d) $\beta = 3.33, b = 1, W_b = 23.281$.

Each panel shows the range $400 \leq n \leq 600$, where breather localisation is most evident.
Table A.2 presents optical breather profiles at wave number $k = \pi$, recorded at $t_{\max} = 2000$ (or $t = 1000$) across four different model cases. The simulations use either $N = 400$ or 1000, and only selected spatial ranges are shown to focus on breather localisation.

- **Case I** ($a = 0$, $\alpha = 0$). Subfigures: (a) $\beta = 1, b = 0.001, W_b = 16.057$; (b) $\beta = 0, b = 0.2, W_b = 12.022$; (c) $\beta = 1, b = 0.01, W_b = 19.089$; (d) $\beta = 1, b = 0, W_b = 12.893$; all for $N = 400$, with $100 \leq n \leq 300$ displayed.

- **Case II** ($a = 0$, $\alpha = 1$). Subfigures: (a) $\beta = b = 0.1, W_b = 21.000$; (b) $\beta = b = 0.335, W_b = 19.235$; (c) $\beta = b = 0.33, W_b = 19.104$, $N = 500$; (d) $\beta = b = 0.67, W_b = 15.569$; all with $100 \leq n \leq 300$ displayed.

- **Case III** ($a = 1$, $\alpha = 0$). Subfigures: (a) $\beta = b = 1.28, W_b = 18.033$; (b) $\beta = b = 0.21, W_b = 18.511$; (c) $\beta = b = 1.31, W_b = 20.696$; (d)

Case	(a)$\rho = 3, \mu = 3$	(b)$\rho = 3, \mu = \frac{1}{3}$	(c)$\rho = \frac{1}{3}, \mu = 3$	(d)$\rho = \frac{1}{3}, \mu = \frac{1}{3}$
I	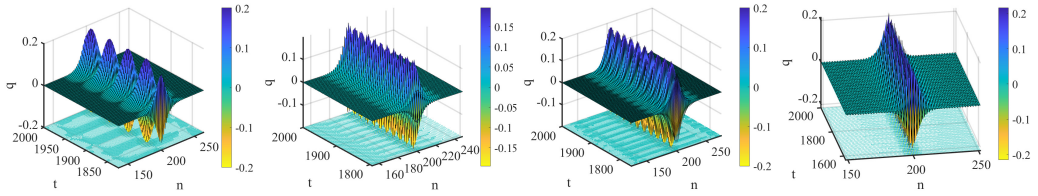			
II	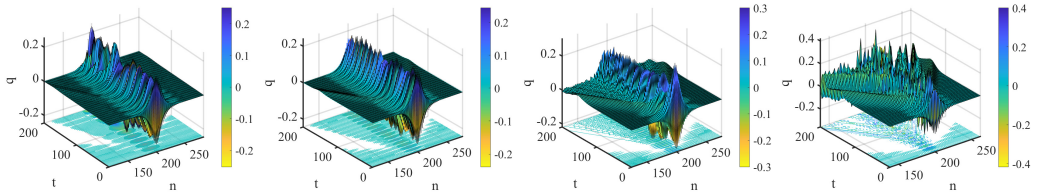			
III	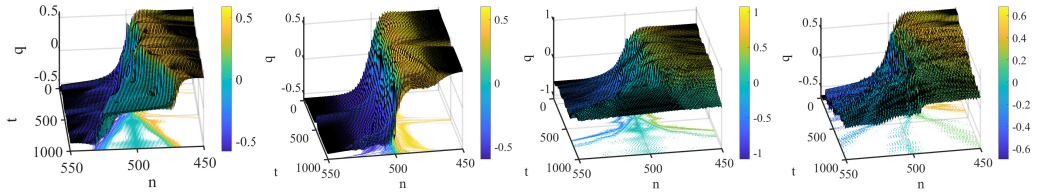			
IV	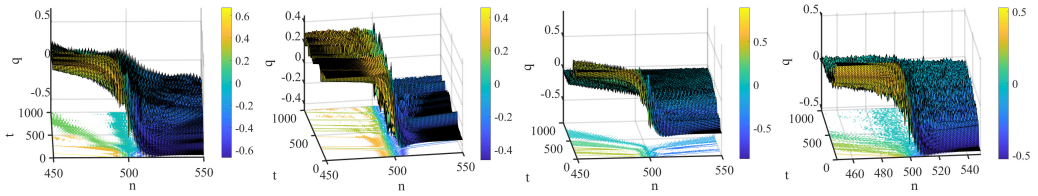			

Table A.2: Optical breather profiles at $k = \pi$ for Cases I–IV.

$\beta = b = 1.19, W_b = 21.321$; all for $N = 1000$, displaying $400 \leq n \leq 600$ at early simulation times.

- **Case IV** ($a = 1$, $\alpha = 1$). Subfigures: (a) $\beta = b = 1.3, W_b = 21.000$; (b) $\beta = 0.6, b = 0.3, W_b = 11.119$; (c) $\beta = b = 1.6, W_b = 16.678$; (d) $\beta = b = 1.8, W_b = 16.036$; with $400 \leq n \leq 600$ shown in each case.

Case	(a)$\rho = 3, \mu = 3$	(b)$\rho = 3, \mu = \frac{1}{3}$	(c)$\rho = \frac{1}{3}, \mu = 3$	(d) $\rho = \frac{1}{3}, \mu = \frac{1}{3}$
I	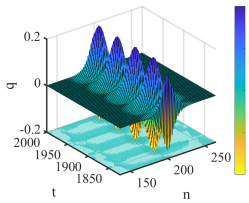	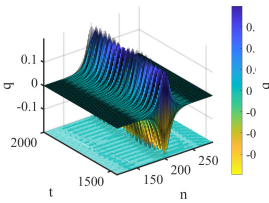	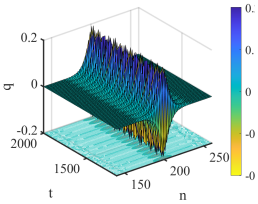	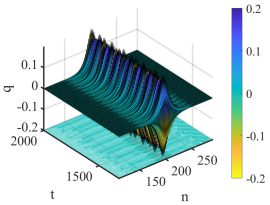
II	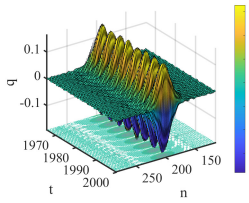	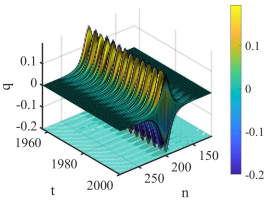	defocusing	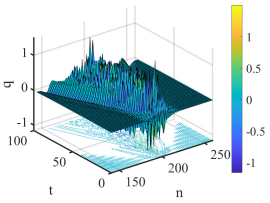
III	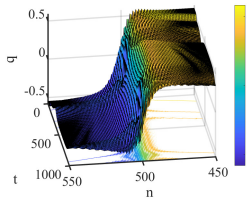	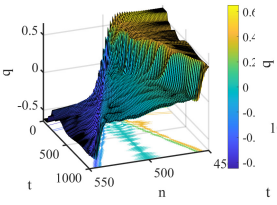	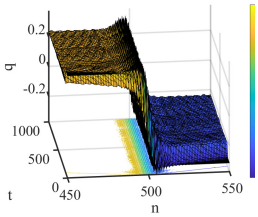	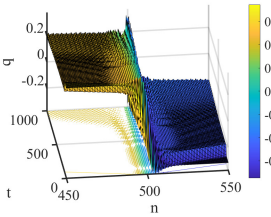
IV	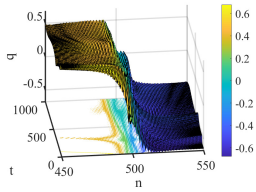	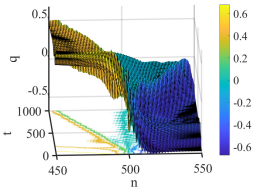	defocusing	defocusing

Table A.3: Acoustic breather profiles at $k = \pi$ for Cases I–IV.

Table A.3 presents acoustic breather profiles at wave number $k = \pi$, evaluated at either $t = 2000$ or $t = 1000$, depending on the case. The simulations use $N = 400$ or 1000, and the displayed spatial range is restricted (e.g., $150 \leq n \leq 300$ or $400 \leq n \leq 600$) to emphasise localisation. Each case explores a distinct nonlinear configuration:

- **Case I** ($a = 0$, $\alpha = 0$). Subfigures: (a) $\beta = 1, b = 0.001, W_b = 16.057$; (b) $\beta = 1, b = 0.06, W_b = 21.567$; (c) $\beta = 0.0001, b = 0.01, W_b = 15.097$; (d) $\beta = 0.0001, b = 0.01, W_b = 22.602$; all for $N = 400$, with $150 \leq n \leq 300$ displayed.

- **Case II** ($a = 0$, $\alpha = 1$). Subfigures: (a) $\beta = b = 0.15, W_b = 21.239$; (b) $\beta = b = 0.07, W_b = 21.205$; (d) $\beta = 2.82, b = 4.5, W_b = 14.899$; all for $N = 400$, displaying $150 \leq n \leq 300$. For $\rho = \frac{1}{3}$, $\mu = 3$, the system is defocusing for all $-10 \leq \beta, b \leq 10$.

- **Case III** ($a = 1$, $\alpha = 0$). Subfigures: (a) $\beta = b = 1.28, W_b = 18.033$; (b) $\beta = b = 1.4, W_b = 20.369$; (c) $\beta = 0, b = 1.6, W_b = 10.412$; (d) $\beta = 0.01, b = 0.02, W_b = 2.940$; all for $N = 1000$, with $400 \leq n \leq 600$ displayed.

- **Case IV** ($a = 1$, $\alpha = 1$). Subfigures: (a) $\beta = b = 1.35, W_b = 21.239$; (b) $\beta = b = 1.4, W_b = 21.285$; all for $N = 1000$, with $400 \leq n \leq 600$ displayed. When $\rho = \frac{1}{3}$, the system remains defocusing.

Table A.4 presents optical breather profiles at wave number $k = 3.1$, with simulations at $t = 1000$ and $N = 1000$. The spatial range is restricted to $200 \leq n \leq 350$ to highlight localisation effects. Each case investigates different combinations:

- **Case I** ($a = 0$, $\alpha = 0$). Subfigures: (a) $\beta = 1, b = 0, W_b = 16.123$; (b) $\beta = 0.019, b = 0.01, W_b = 15.556$; (c) $\beta = 1, b = 0.018, W_b = 18.191$; (d) $\beta = 1, b = 0, W_b = 12.887$; all for $t = 1000$, $N = 1000$, displaying $200 \leq n \leq 350$ at the end time.
- **Case II** ($a = 0$, $\alpha = 1$). Subfigures: (a) $\beta = b = 0.1, W_b = 21.007$; (b) $\beta = b = 0.33, W_b = 25.615$; (c) $\beta = b = 0.32, W_b = 20.579$; (d) $\beta = b = 0.67, W_b = 15.618$; all for $t = 1000$, $N = 1000$, with $200 \leq n \leq 350$ displayed at early time.
- **Case III** ($a = 1$, $\alpha = 0$). Subfigures: (a) $\beta = b = 1.27, W_b = 19.392$; (b) $\beta = 0.01, b = 1.31, W_b = 29.058$; (c) $\beta = 0.01, b = 1.41, W_b = 19.596$; (d) $\beta = 0.1, b = 1.4, W_b = 18.612$; all for $t = 1000$, $N = 1000$, displaying $200 \leq n \leq 350$.

Case	(a) $\rho = 3, \mu = 3$	(b) $\rho = 3, \mu = \frac{1}{3}$	(c) $\rho = \frac{1}{3}, \mu = 3$	(d) $\rho = \frac{1}{3}, \mu = \frac{1}{3}$
I	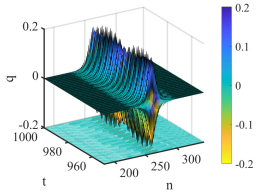	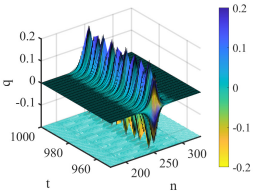	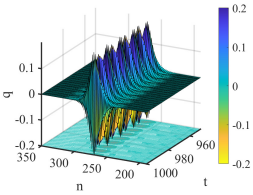	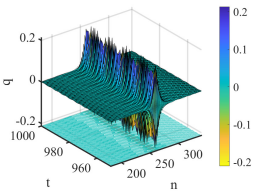
II	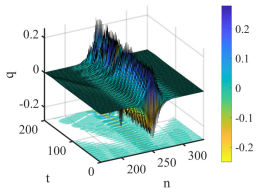	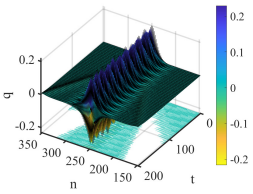	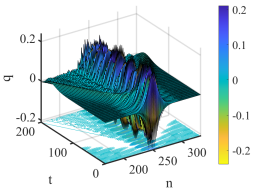	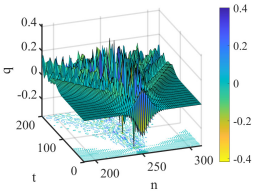
III	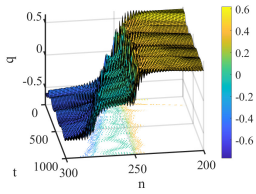	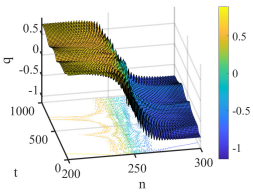	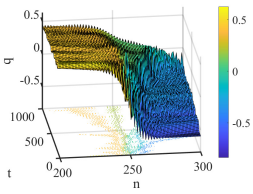	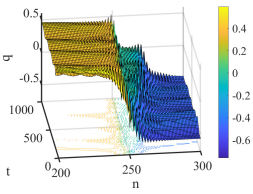

Table A.4: Optical breather profiles at $k = 3.1$ for Cases I–III.

Case	(a)$\rho = 3, \mu = 3$	(b) $\rho = 3, \mu = \frac{1}{3}$	(c)$\rho = \frac{1}{3}, \mu = 3$	(d)$\rho = \frac{1}{3}, \mu = \frac{1}{3}$
I	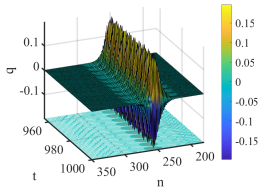	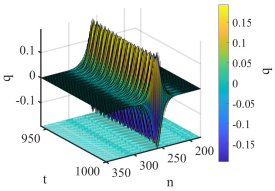	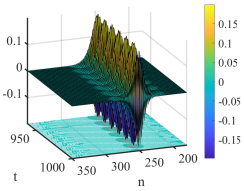	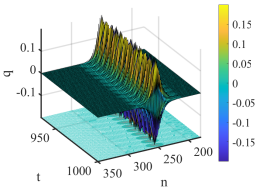
II	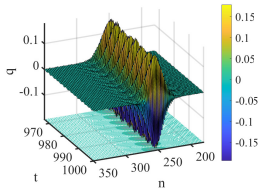	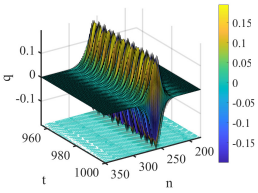	defocusing	defocusing
III	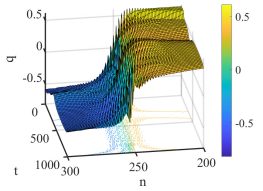	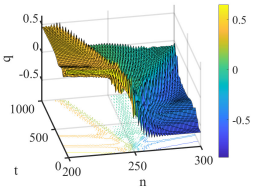	defocusing	defocusing

Table A.5: Acoustic breather profiles at $k = 3.1$ for Cases I–III.

Table A.5 presents acoustic breather profiles at wave number $k = 3.1$, with simulations carried out at $t = 1000$ and $N = 1000$. The spatial domain is limited to $200 \leq n \leq 350$ to emphasise localisation. Each case explores distinct nonlinear parameter regimes, with detailed values for β, b, and breather width W_b summarised below.

- **Case I** ($a = 0$, $\alpha = 0$). Subfigures: (a) $\beta = 1, b = 0, W_b = 16.147$; (b) $\beta = 1, b = 0.07, W_b = 20.023$; (c) $\beta = 0, b = 0.1, W_b = 17.016$; (d) $\beta = 0, b = 0.1, W_b = 17.019$; all displayed at the end time over $200 \leq n \leq 350$.

- **Case II** ($a = 0$, $\alpha = 1$). Subfigures: (a) $\beta = b = 0.15, W_b = 21.210$; (b) $\beta = b = 0.07, W_b = 21.207$; displayed at early simulation time over $200 \leq n \leq 350$.

- **Case III** ($a = 1$, $\alpha = 0$). Subfigures: (a) $\beta = 0.01, b = 1.41, W_b = 19.233$; (b) $\beta = 0.1, b = 1.4, W_b = 20.509$; simulated over $0 \leq t \leq 850$, with $200 \leq n \leq 350$ displayed throughout.

Table A.6 shows optical breather profiles at wave number $k = 0.1$, simulated over $t = 1000$ with $N = 1000$. The range $200 \leq n \leq 350$ is used for visualisation. Each case explores a distinct nonlinear configuration listed below.

Case	(a)$\rho = 3, \mu = 3$	(b)$\rho = 3, \mu = \frac{1}{3}$	(c)$\rho = \frac{1}{3}, \mu = 3$	(d) $\rho = \frac{1}{3}, \mu = \frac{1}{3}$
I	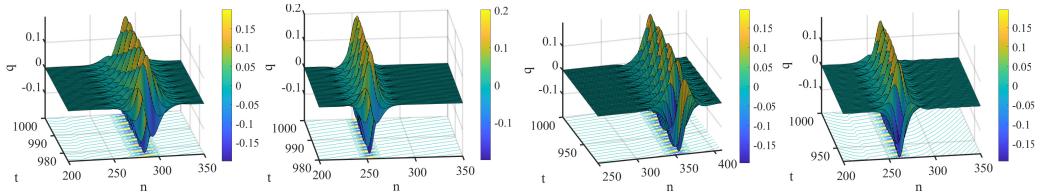			
II	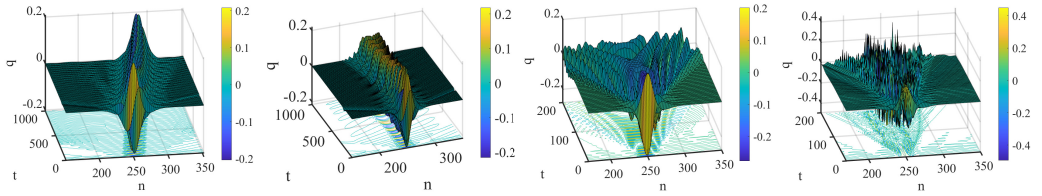			
III	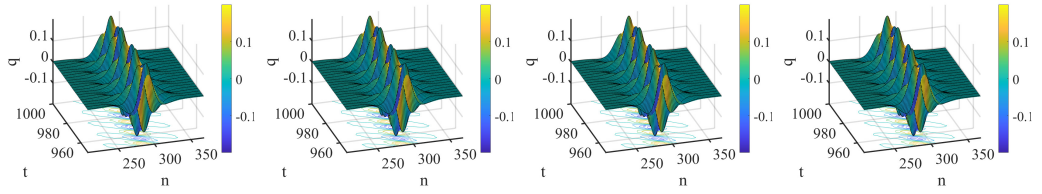			

Table A.6: Optical breather profiles at $k = 0.1$ for Cases I–III.

- **Case I** ($a = 0$, $\alpha = 0$). Subfigures: (a) $b = 1, \beta = -0.3, W_b = 22.066$; (b) $b = 1, \beta = -0.009, W_b = 14.167$; (c) $b = 1, \beta = -0.3, W_b = 22.330$; (d) $b = 1, \beta = -0.009, W_b = 14.440$; all with $200 \leq n \leq 350$ displayed.
- **Case II** ($a = 0$, $\alpha = 1$). Subfigures: (a) $b = \beta = 0.09, W_b = 22.825$; (b) $b = \beta = 0.366, W_b = 20.330$; (c) $b = \beta = 3, W_b = 21.185$; (d) $b = \beta = 3.33, W_b = 23.716$; all with $200 \leq n \leq 350$ displayed, taken at early time $0 \leq n \leq 250$.
- **Case III** ($a = 1$, $\alpha = 0$). Subfigures: (a) $b = 10, \beta = -0.20, W_b = 27.043$; (b) $b = \beta = -0.003, W_b = 24.535$; (c) $b = 10, \beta = -0.20, W_b = 27.366$; (d) $b = \beta = -0.003, W_b = 25.008$; all with $200 \leq n \leq 350$ displayed.

Case	(a) $\rho = 3, \mu = 3$	(b)$\rho = 3, \mu = \frac{1}{3}$	(c)$\rho = \frac{1}{3}, \mu = 3$	(d)$\rho = \frac{1}{3}, \mu = \frac{1}{3}$
I	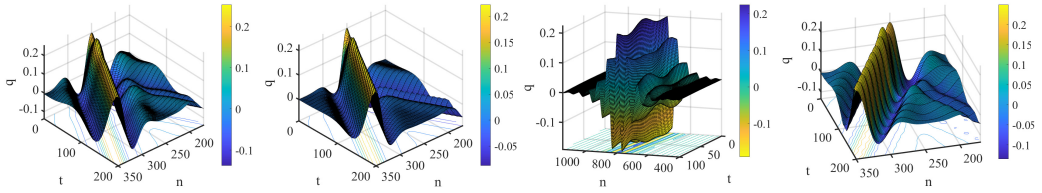			

Table A.7: Acoustic breather profiles at $k = 0.1$ for Cases I–II.

Table A.7 presents acoustic breather profiles at wave number $k = 0.1$, simulated with $t = 1000$ and $N = 1000$. The spatial region $500 \leq n \leq 1000$ is used to highlight the localisation range, and the parameter values are summarised below.

- **Case I** ($a = 0$, $\alpha = 0$). Subfigures: (a) $b = \beta = 10, W_b = 61.278$; (b) $b = \beta = 10, W_b = 38.031$; (c) $b = \beta = 10, W_b = 156.601$; (d) $b = \beta = 10, W_b = 61.631$; with $500 \leq n \leq 1000$ displayed for subfigures (a), (b), and (c).

- **Case II**. The breather dynamics and parameter regimes are the same as in Case I.

Appendix B

Supplementary material: Chapter 3

This section addresses Cases 2, 3, and 5 from Table 3.2, extending the analysis of stationary optical and acoustic properties previously discussed for Cases 1 and 4 in Section 3.4. We begin with Case 2 (a saddle point) and Case 3 (a global maximum), focusing on their corresponding stationary optical and acoustic characteristics. Subsequently, we examine Case 5 (the saddle point) to explore its distinct behaviour.

B.1 Cases 2: Saddle Point and 3: Global Maximum

In Cases 2 and 3 (optical and acoustic), we focus on special wave numbers: $(\pm\pi/2, \pm\pi/(2\sqrt{3}))$ and $(0, \pm\pi/\sqrt{3})$. These are labelled as follows b $= (k, l) = (\pi/2, \pi/(2\sqrt{3}))$, f $= (-\pi/2, \pi/(2\sqrt{3}))$, c $= (\pi/2, -\pi/(2\sqrt{3}))$, e $= (-\pi/2, -\pi/(2\sqrt{3}))$.
The quantities C_{ac} and C_{op} are defined in equations (3.3.8) and (3.3.9), respectively. Due to the system's symmetry, the results for points b and e are identical, as are those for f and c. To avoid redundancy, we report only the results for wave vectors b and f. For Cases 2b and 3b, from Table 3.1, the coefficients are given by

$$\omega^2(k,l) \approx \frac{1}{2}\left(\mathrm{tr} \pm \sqrt{\mathrm{tr}^2 - 4\det}\right), \qquad \omega_{ac}^2 \approx \Omega^2 + 2\rho, \qquad \omega_{op}^2 \approx \Omega^2 + 6\rho. \tag{B.1.1}$$

using (3.3.8) and (3.3.9), we have

$$\begin{aligned} C_{op} &= \frac{-\sqrt{3}\rho \sin(k)\sin(l\sqrt{3})}{\Omega^2 - \omega_{op}^2 + 3\rho\left(1 - \cos(k)\cos(l\sqrt{3})\right)} = \frac{1}{\sqrt{3}}, \\ C_{ac} &= \frac{-\sqrt{3}\rho(1)(1)}{\Omega^2 - \omega_{ac}^2 + 3\rho(1-0)} = -\sqrt{3}. \end{aligned} \tag{B.1.2}$$

Evaluating U, V, $\tilde{U}$, and $\tilde{V}$ using equations (3.3.27)–(3.3.28) and (3.3.33)–

(3.3.34) at point b and with the values from (B.1.1) and (B.1.2), we find

$$U = V = 0, \quad \tilde{U} = \tilde{V} = 0,$$

in both optical and acoustic cases. The NLS coefficients for the acoustic case are

$$\Theta_{ac} = 8\sqrt{\Omega^2 + 2\rho}, \qquad D_{Zac} = -\rho, \qquad D_{Wac} = 9\rho, \tag{B.1.3}$$

$$D_{Mac} = -10\sqrt{3}\rho, \qquad D_{Nac} = -12\lambda, \tag{B.1.4}$$

$$\mathcal{E}_{ac} = 4(-\rho)(9\rho) - \left(-10\sqrt{3}\rho\right)^2 = -36\rho^2 - 300\rho^2 < 0. \tag{B.1.5}$$

Hence, the system is not elliptic at Case 2 b and e, which agrees with the numerical results in Figure 3.11. For the optical case, we find

$$\Theta_{op} = \frac{8}{3}\sqrt{\Omega^2 + 6\rho}, \qquad D_{Zop} = -5\rho, \qquad D_{Wop} = -3\rho, \tag{B.1.6}$$

$$D_{Mop} = -2\sqrt{3}\rho, \qquad D_{Nop} = -3\lambda(1.3), \tag{B.1.7}$$

$$\mathcal{E}_{op} = 4(-5\rho)(-3\rho) - \left(-2\sqrt{3}\rho\right)^2 = 48\rho^2 > 0, \tag{B.1.8}$$

$$\mathcal{F}_{op} = (-3\lambda)(1.3)(-5\rho) = 20\lambda\rho > 0, \quad \lambda > 0. \tag{B.1.9}$$

This confirms that Case 3 b and e satisfy both the focusing and elliptic conditions, as supported by the simulation results in Figure 3.11.

B.2 At Saddle Case 5

To begin the analysis, we consider the case $(k, l) = (\cos^{-1}(-1/8), 0)$, as the case with negative k is analogous due to symmetry. Using the value of ω from Table 3.1, we have $\omega_{op} = \sqrt{\Omega^2 + 5\rho}$. For this case, the calculations proceed via direct substitution

$$C_{op} = \frac{-\sqrt{3}\rho \sin(k)\sin(l\sqrt{3})}{\Omega^2 - \omega_{op}^2 + 3\rho(1 - \cos(k)\cos(l\sqrt{3}))} = 0. \tag{B.2.1}$$

Evaluating the quantities U, V, $\tilde{U}$, and $\tilde{V}$ using equations (3.3.27)–(3.3.28) and (3.3.33)–(3.3.34), we find

$$U = V = 0, \quad \tilde{U} = \tilde{V} = 0.$$

The corresponding NLS coefficients are

$$\Theta_{op} = \sqrt{\Omega^2 + 5\rho}, \qquad D_{Zop} = -3.9, \qquad D_{Wop} = -0.18, \tag{B.2.2}$$

$$D_{ZWop} = 0, \qquad D_{Nop} = -3\lambda, \qquad \mathcal{E}_{op} = 4(-3.9)(-0.18) = 2.8 > 0, \tag{B.2.3}$$

$$\mathcal{F}_{op} = (-3.9)(-3\lambda) = 11.7\rho\lambda > 0. \tag{B.2.4}$$

Therefore, the system is elliptic and focusing provided that $\lambda > 0$.

B.2.1 Cases 5 (b) and (e)

We now consider point b, defined as $b = \left(\frac{1}{2}\cos^{-1}(-1/8), \frac{\sqrt{3}}{2}\cos^{-1}(-1/8)\right)$. The case $e = \left(-\frac{1}{2}\cos^{-1}(-1/8), -\frac{\sqrt{3}}{2}\cos^{-1}(-1/8)\right)$ is symmetric and hence yields identical results. In both cases, we have $\omega_{op} = \sqrt{\Omega^2 + 5\rho}$, and

$$C_{op} = \frac{-\sqrt{3}\rho\sin(k)\sin(l\sqrt{3})}{\Omega^2 - \omega_{op}^2 + 3\rho(1 - \cos(k)\cos(l\sqrt{3}))} = \sqrt{3}. \tag{B.2.5}$$

From equations (3.3.27)–(3.3.28) and (3.3.33)–(3.3.34), we obtain

$$U = V = 0, \quad \tilde{U} = \tilde{V} = 0.$$

The resulting NLS coefficients are

$$\Theta_{op} = \sqrt{\Omega^2 + 5\rho}, \qquad D_{Zop} = -4.5\rho, \qquad D_{Wop} = -12\rho, \tag{B.2.6}$$

$$D_{ZWop} = -12\rho, \qquad D_{Nop} = -48\lambda, \tag{B.2.7}$$

$$\mathcal{E}_{op} = 4(-4.5)(-12) - (-12\rho)^2 = 72\rho^2 > 0, \tag{B.2.8}$$

$$\mathcal{F}_{op} = (-4.5)(-48\lambda) = 216\rho\lambda > 0. \tag{B.2.9}$$

Thus, the system remains elliptic and focusing for $\lambda > 0$.

B.2.2 Cases 5 (c) and (f)

Finally, we consider case $c = \left(-\frac{1}{2}\cos^{-1}(-1/8), \frac{\sqrt{3}}{2}\cos^{-1}(-1/8)\right)$. The corresponding value of ω is

$$\omega^2(k, l) = \Omega^2 + 5\rho, \tag{B.2.10}$$

and the coupling coefficient becomes

$$C_{op} = \frac{-\sqrt{3}\rho\sin(k)\sin(l\sqrt{3})}{\Omega^2 - \omega_{op}^2 + 3\rho(1 - \cos(k)\cos(l\sqrt{3}))} = -\sqrt{3}. \tag{B.2.11}$$

Again, from equations (3.3.27)–(3.3.28) and (3.3.33)–(3.3.34), we have

$$U = V = 0, \quad \tilde{U} = \tilde{V} = 0.$$

The associated NLS coefficients are

$$\Theta_{op} = \sqrt{\Omega^2 + 5\rho}, \qquad D_{Zop} = -4.5\rho, \qquad D_{Wop} = -12\rho, \tag{B.2.12}$$

$$D_{ZWop} = 12\rho, \qquad D_{Nop} = -48\lambda, \tag{B.2.13}$$

$$\mathcal{E}_{op} = 4(-4.5)(-12) - (12\rho)^2 = 72\rho^2 > 0, \tag{B.2.14}$$

$$\mathcal{F}_{op} = (-4.5)(-48\lambda) = 216\rho\lambda > 0. \tag{B.2.15}$$

Therefore, the system is again elliptic and focusing for $\lambda > 0$.

Appendix C

Supplementary material: Chapter 4

C.1 Reduction of the system

In this section, we reduce the 4×4 system in 4 to a pair of 2×2 matrix equations in order to simplify the analysis of the special points identified in Table 4.1, specifically Cases 3, 4, and 5.
The system introduced in Section 4.3.6 can be rewritten in block matrix form as

$$m_1 \begin{pmatrix} \overline{\mathbf{F}} \\ \overline{\hat{\mathbf{F}}} \end{pmatrix} = \begin{pmatrix} \mathbf{A} \\ \mathbf{B} \end{pmatrix}, \tag{C.1.1}$$

or equivalently

$$\begin{pmatrix} M_{11} & M_{12} \\ M_{21} & M_{22} \end{pmatrix} \begin{pmatrix} \overline{\mathbf{F}} \\ \overline{\hat{\mathbf{F}}} \end{pmatrix} = \begin{pmatrix} \mathbf{A} \\ \mathbf{B} \end{pmatrix}, \tag{C.1.2}$$

where $\overline{\mathbf{F}} = (F, P)^T$, $\overline{\hat{\mathbf{F}}} = (\hat{F}, \hat{P})^T$, and $\mathbf{A} = (A_1, A_2)^T$, $\mathbf{B} = (B_1, B_2)^T$ are the right-hand side vectors defined in equations (4.3.25)–(4.3.28).
The diagonal blocks M_{11} and M_{22} are equal and take the form

$$M_{11} = M_{22} = \begin{pmatrix} \Omega^2 - \omega^2 + \dfrac{3\rho}{2} & 0 \\ 0 & \Omega^2 - \omega^2 + \dfrac{3\rho}{2} \end{pmatrix}, \tag{C.1.3}$$

where $\omega^2 \neq \Omega^2 + \dfrac{3\rho}{2}$. The off-diagonal block M_{12} is given by

$$M_{12} = \begin{pmatrix} -e^{ik}\left(2\rho e^{-3ik} + \rho\cos(l\sqrt{3})\right) & -\dfrac{i}{2}\sqrt{3}\rho e^{ik}\sin(l\sqrt{3}) \\ -\dfrac{i}{2}\sqrt{3}\rho e^{ik}\sin(l\sqrt{3}) & -\dfrac{3\rho}{2}e^{ik}\cos(l\sqrt{3}) \end{pmatrix}, \tag{C.1.4}$$

and the lower-left block M_{21} is simply the Hermitian transpose of M_{12}, i.e.,

$$M_{21} = M_{12}^{*T},$$

where * denotes complex conjugation and ^{T} the transpose.
Thus, the reduced system may be expressed as

$$M_{11}\,\overline{\mathbf{F}} + M_{12}\,\overline{\hat{\mathbf{F}}} = \mathbf{A}, \tag{C.1.5}$$

$$M_{12}^{*T}\,\overline{\mathbf{F}} + M_{11}\,\overline{\hat{\mathbf{F}}} = \mathbf{B}. \tag{C.1.6}$$

Solving equation (C.1.6) for $\overline{\hat{\mathbf{F}}}$ gives

$$\overline{\hat{\mathbf{F}}} = M_{11}^{-1}\left(-M_{12}^{*T}\overline{\mathbf{F}} + \mathbf{B}\right). \tag{C.1.7}$$

Since $M_{11} = M_{22}$, both can be expressed in terms of the identity matrix as

$$M_{11} = M_{22} = \left(\Omega^2 - \omega^2 + \frac{3\rho}{2}\right)\cdot \mathbf{I}, \tag{C.1.8}$$

where $\mathbf{I}$ is the 2×2 identity matrix. Substituting the expression for $\overline{\hat{\mathbf{F}}}$ from equation (C.1.7) into equation (C.1.5), we obtain

$$\begin{aligned} M_{11}\,\overline{\mathbf{F}} + M_{12}M_{22}^{-1}\left(-M_{12}^{*T}\overline{\mathbf{F}} + \mathbf{B}\right) = \mathbf{A}, \qquad &\text{which leads to} \\ \left(M_{11} - M_{12}M_{22}^{-1}M_{12}^{*T}\right)\overline{\mathbf{F}} = \mathbf{A} - M_{12}M_{22}^{-1}\mathbf{B}. \qquad &\text{(C.1.9)} \end{aligned}$$

This reduced form will be used in Sections 4.6 and 4.7 to simplify the analysis of the Dirac point and saddle point cases, respectively.
To solve the coupled block matrix system in equations (C.1.5) and (C.1.6), we proceed as follows

1. **To compute** M_{11}^{-1} From equation (C.1.8), we know that both M_{11} and M_{22} are scalar multiples of the identity matrix. Since the inverse of a scalar multiple of the identity is just the reciprocal of the scalar times the identity, we have $M_{11}^{-1} = \dfrac{1}{\Omega^2 - \omega^2 + \dfrac{3\rho}{2}} \cdot \mathbf{I}$.

2. **Solve the reduced linear system**
   Equation (C.1.9) is a 2×2 linear system in the unknown vector $\overline{\mathbf{F}} = (F, P)^T$. Compute

   $$\overline{\mathbf{F}} = \left(M_{11} - M_{12}M_{11}^{-1}M_{12}^{*T}\right)^{-1}\left(\mathbf{A} - M_{12}M_{11}^{-1}\mathbf{B}\right).$$

   This inversion is non-singular. The right-hand side is known, and the matrices involved are computable from the system parameters. Back-substitute into equation (C.1.7). Once $\overline{\mathbf{F}}$ is found, substitute it into

   $$\overline{\hat{\mathbf{F}}} = M_{11}^{-1}\left(-M_{12}^{*T}\overline{\mathbf{F}} + \mathbf{B}\right),$$

   to find the corresponding components $\overline{\hat{\mathbf{F}}} = (\hat{F}, \hat{P})^T$.